

WATER-MEDIATED INTERACTIONS THROUGH THE LENS OF RAMAN MULTIVARIATE CURVE RESOLUTION

by

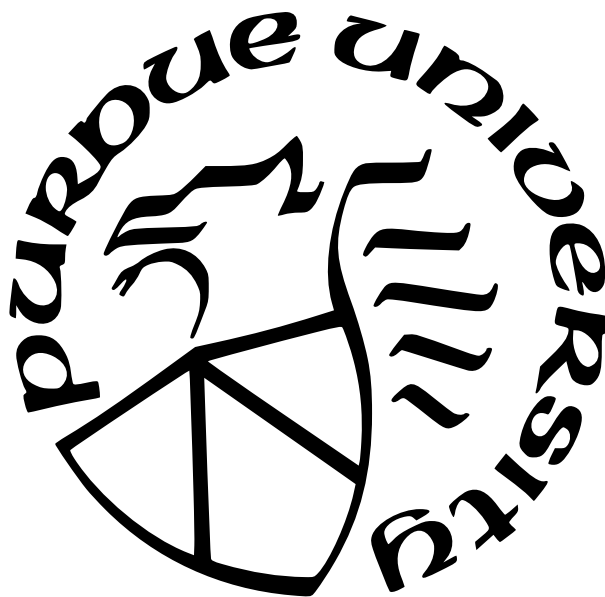
Denilson Mendes de Oliveira

A Dissertation

Submitted to the Faculty of Purdue University

In Partial Fulfillment of the Requirements for the Degree of

Doctor of Philosophy



Department of Chemistry

West Lafayette, Indiana

May 2021

**THE PURDUE UNIVERSITY GRADUATE SCHOOL
STATEMENT OF COMMITTEE APPROVAL**

Dr. Dor Ben-Amotz, Chair

Department of Chemistry

Dr. Mary Wirth

Department of Chemistry

Dr. Julia Laskin

Department of Chemistry

Dr. Adam Wasserman

Department of Chemistry

Approved by:

Dr. Christine A. Hrycyna

ACKNOWLEDGMENTS

I am especially grateful to Prof. Dor Ben-Amotz for his support and always being enthusiastic in the course of this work. Dor goes beyond his role as an advisor by also being a fantastic example of a great researcher, writer, and teacher. I also thank Prof. Julia Laskin, Prof. Mary Wirth, and Prof. Adam Wasserman for their time and helpful comments on this thesis.

Thanks also to Prof. Ana Vila Verde and Dr. João Robalo (Max Planck Institute for Colloids and Interfaces) for a very fruitful collaboration. I am very much indebted to them for getting us started with hydration-shell studies of fluorinated molecules and providing insightful simulation results that enhanced the interpretation of our experimental results. I also acknowledge Dr. Elise Duboué-Dijon (CNRS, Université de Paris), Prof. Pavel Jungwirth (Academy of Sciences of the Czech Republic) and their research groups for performing simulations of ion pairing in aqueous solutions of metal(II) acetate salts. In addition, I thank Prof. Steven Corcelli and Tierney Miller (University of Notre Dame) for their contributions to our paper on ion pairing in aqueous hydroxide solutions.

A special thanks to all the friends I have made at Purdue. You have helped me achieve more in research and have provided good advice when I needed it. I will not forget our fun times together.

Finally, I want to express my gratitude to my fiancée and family in Brazil. You have helped me grow into a better person and go after my dreams even when I stumbled and thought it would not be possible.

TABLE OF CONTENTS

LIST OF TABLES	7
LIST OF FIGURES	8
ABSTRACT	14
1 RAMAN SPECTROSCOPY AND MULTIVARIATE DATA ANALYSIS	15
1.1 Instrumentation	17
1.2 Self-Modeling Curve Resolution	18
1.3 Organization of the Thesis	23
2 CAVITY HYDRATION AND COMPETITIVE BINDING IN METHYLATED β -CYCLODEXTRIN	25
2.1 Introduction	25
2.2 Experimental Details	27
2.3 Results and Discussion	28
2.4 Conclusions	32
3 EFFECTS OF FLUORINATION ON HYDRATION-SHELL THERMODYNAMICS AND SOLUTE-WATER INTERACTIONS	34
3.1 Introduction	34
3.2 Experimental Methods	36
3.3 Computational Methods	38
3.4 Results and Discussion	39
3.5 Conclusions	47
4 SPECIFIC ION EFFECTS ON NONIONIC MICELLE FORMATION	49
4.1 Introduction	49
4.2 Experimental Methods	52
4.3 Results and Discussion	53
4.4 Conclusions	58

5	DIRECT-CONTACT ION PAIRING IN AQUEOUS ACETATE SOLUTIONS . .	59
5.1	Introduction	59
5.2	Experimental Details	61
5.3	Computational Details	64
5.4	Results	64
5.5	Discussion	67
5.6	Conclusions	69
6	WATER-SHARED ION PAIRING IN AQUEOUS HYDROXIDE SOLUTIONS . .	71
6.1	Introduction	71
6.2	Methods	72
6.3	Results	76
6.4	Summary and Discussion	83
	REFERENCES	86
A	SUPPLEMENTARY METHODS AND EXPERIMENTAL RESULTS FOR HOST-GUEST BINDING STUDIES	103
A.1	Total least squares regression	103
A.2	Determination of the host–guest binding constant and Raman cross section change	104
A.3	Determination of the number of water molecules in the Me- β -CD cavity . . .	106
B	SUPPORTING INFORMATION FOR DANGLING HYDROXY FORMATION IN AQUEOUS SOLUTIONS OF FLUORINATED ETHANOL	107
B.1	Solute-correlated hydration-shell spectrum of ethanol	107
B.2	Assignment of the high frequency OH peak	107
B.3	Dangling OH bands after subtracting a Gaussian background	109
B.4	Hydration thermodynamics	110
C	ADDITIONAL METHODS AND EXPERIMENTAL RESULTS FOR RAMAN-MCR OF MICELLE FORMATION	111

C.1	Additional experimental results	111
C.2	Derivation of micellization and Wyman-Tanford expressions	115
C.3	Wyman-Tanford partition coefficient bounds	118
D	SUPPLEMENTARY INFORMATION FOR ION PAIRING IN ACETATE SOLUTIONS	121
D.1	Raman spectra of bound acetate	121
D.2	Binding constant determination using TLS regression	122
D.3	Influence of ion pairing on acetate hydration shell spectra	125
D.4	Simulated Raman spectra	126
D.5	Binding patterns from DFT-based <i>ab initio</i> molecular dynamics simulations	128
E	ADDITIONAL RESULTS FOR WATER-SHARED ION PAIRING IN HYDROXIDE SOLUTIONS	130
E.1	Temperature-dependent thermodynamic analysis	130
E.2	Additional Raman-MCR results	131
E.3	Supporting AIMD results	132
	LIST OF PUBLICATIONS	136

LIST OF TABLES

5.1	Comparison of the standard binding constant K° (extrapolated to zero ionic strength as described in Ref. [149]) for the formation of the 1:1 cation:acetate complex for different divalent cations, as obtained from Raman-MCR and previous studies.	69
B.1	Henry’s law coefficients of EtOH, MFE, DFE, and TFE.	110
B.2	Experimental hydration free energy of EtOH, MFE, DFE, and TFE.	110
D.1	Ion-pairing binding constants obtained from TLS fits to different vibrational bands. Errors correspond to the standard deviation of the values of K obtained in the 0.2 to 1 M total acetate concentration range.	124
E.1	K_0 and b values obtained from the dissociation fraction x_F points in Fig. E.1. .	131

LIST OF FIGURES

1.1	Energy level diagram illustrating the origin of Raman spectra. The horizontal dashed lines represent a <i>virtual</i> state, and $v = 0, 1$ are vibrational quantum levels separated by an energy gap $h\nu$, where h is Planck's constant and ν is the vibrational frequency.	16
1.2	Typical neon emission spectrum (A) highlighting the emission lines used for wavelength calibration and Raman spectrum of water (B) obtained at 20 °C using the home-built Raman system.	19
1.3	Example of a Ramam-MCR decomposition for <i>tert</i> -butyl alcohol (TBA) at 20 °C. (A) Measured Raman spectrum for pure water and 1 mol L ⁻¹ TBA. (B) Raman-MCR SC component spectra obtained by decomposing the spectra shown in panel A. (C) Expanded view showing the TBA hydration-shell OH stretch and highlighting a small dangling band.	21
2.1	(A) Raman spectra of pure water, 0.1 M Me- β -CD, and 0.1 M Me- β -CD + benzene-d ₆ . (B) Hydration-shell spectra of Me- β -CD at different concentrations. (C) Hydration-shell spectra of Me- β -CD with and without benzene-d ₆ (with inset panels showing expanded views of the O-H stretch region). (D) Comparison of the O-H stretch bands of cavity-bound (solid blue) and pure liquid (dashed blue) water molecules. The cavity-bound O-H band is obtained from the difference between the purple and orange O-H bands in (C).	29
2.2	Spectroscopic determination of the host-guest binding equilibrium constant and Raman cross section ratio of bound and unbound benzene-d ₆ (guest), all of which have a total benzene-d ₆ concentration of 10 mM. (A) The C-D stretch bands of the free (dashed blue) and bound (dashed orange) benzene-d ₆ are compared with those obtained from mixtures containing total Me- β -CD (host) concentrations of 10 mM, 15 mM and 20 mM. (B) The fraction of bound benzene-d ₆ (points) are plotted as a function of total Me- β -CD concentration and compared with binding curves pertaining to $K = 92$ and 110. The inset panel in (B) shows the TLS reconstruction (dashed curves) of the measured (solid green curve) guest C-D stretch band pertaining to the middle point.	31
3.1	A schematic representation of the hydration shell of TFE. A hydroxy group forming a hydrogen bond-like structure is highlighted in green, a free hydroxy group is highlighted in purple; we refer to both structures jointly as non-water-bonded hydroxy groups. Carbon atoms are shown in gray, fluorine in green, oxygen in red and hydrogen in white. The solute and the first hydration shell waters are encircled in blue.	39

3.2	(A) Unprocessed Raman spectra obtained at 20 °C for 1 mol dm ⁻³ solutions of MFE, DFE, and TFE and pure water. (B) Solute-correlated component spectra of MFE, DFE, and TFE. The dashed curves are the corresponding pure water Raman spectra, arbitrarily scaled to highlight the difference in shape between the pure water and SC OH stretch bands.	40
3.3	Hydration-shell spectra of MFE, DFE, and TFE normalized to the CH band area. The solid lines represent the solute-correlated (SC) spectra and the dashed lines represent the (arbitrarily scaled) spectra of pure water.	41
3.4	Temperature dependence of the dangling OH peaks in the hydration shell of (A) MFE, (B) DFE and (C) TFE. These peaks were obtained from the respective minimum area non-negative SC spectra (transparent solid lines), after subtracting the background (dashed lines) using a cubic polynomial function.	42
3.5	Average number, $\langle k \rangle$, of dangling OH structures per hydration shell determined experimentally using the high-frequency OH peak areas.	43
3.6	Enthalpy and entropy changes associated with the formation of dangling OH structures with increasing fluorination of the methyl group of ethanol using the experimental average $\langle k \rangle$ values.	44
3.7	Average number $\langle k \rangle$ of non-water-bonded (panel A) and hydrogen bond-like (panel B) hydroxy structures <i>per</i> hydration shell, quantified with MD simulations in the $278 \leq T/K \leq 358$ range, for solutions of MFE, DFE and TFE.	45
3.8	Free energy of formation of a non-water-bonded hydroxy structures (MFE as red circles, DFE as blue squares, TFE as green triangles) in the $278 \leq T/K \leq 358$ range, calculated from MD simulations. Dashed lines are linear fits to the data points from where the enthalpy (panel A), the entropy (panel B) and their respective errors are calculated.	45
3.9	A) Total interaction energy <i>vs.</i> distance for water-solute dimers forming a hydrogen bond-like structure (water-MFE as red circles, water-DFE as blue squares, water-TFE as green triangles), calculated at the DF-SAPT2+(CCD) δ MP2/aug-cc-pVTZ level of theory. The distance corresponds to the closest water oxygen-fluorine pair. Configurations are extracted from MD simulations at 298 K. The inset molecules represent a conformation of a water-TFE dimer corresponding to one of the plotted data points. B) Average energy components $\langle E \rangle$, calculated for distances above which the total energy becomes attractive (2.5, 2.6 and 2.8 Å for MFE, DFE and TFE, respectively). The number of points in each data set is MFE: 2890; DFE: 1537; TFE: 1314.	46

4.1	Experimental Raman spectra and Raman-MCR results pertaining to 12HD dissolved in pure water. (A) Measured Raman spectra of aqueous 12HD at 20 °C at various concentrations. (B) SC spectra of 12HD in the CH and OH stretch band region, after subtraction of a cubic polynomial background. The inset figure in (B) shows an expanded view of the SC hydration shell OH stretch band region, including the OH bands of pure water (dashed blue curve) and the micelle hydration shell (dotted-black curve). (C) The mean CH frequency of 12HD is plotted a function of $[12HD]_T$. (D) The concentrations of free and aggregated 12HD plotted as a function of $[12HD]_T$, obtained from a TLS fit of the SC spectra in (A) to a linear combination of the free (solid red curve) and aggregated (dotted-black curve) spectra.	55
4.2	Raman-MCR results pertaining to 12HD dissolved in aqueous salt solutions containing either 2 M NaSCN or 0.25 M Na ₂ SO ₄ . (A) Free and aggregated 12HD concentrations in 2 M NaSCN. (B) Free and aggregated 12HD concentrations in 0.25 M Na ₂ SO ₄	57
5.1	Sketch of the different cation-acetate ion pairing modes with the surrounding layer of water molecules, with typical associated C-cation distances (for a Ca ²⁺ cation). Snapshots were prepared using the VMD software. ¹⁴⁶	62
5.2	(A) Raman spectra of acetic acid and sodium acetate at approximately equal concentrations. (B) Raman-MCR SC spectra of sodium acetate solutions as a function of concentration. The water spectrum (dashed black) is for reference.	65
5.3	Concentration-dependent SC spectra of zinc(II) acetate (top), magnesium acetate (middle), and calcium acetate (bottom). The larger concentration dependent changes in the CC and COO ⁻ stretching band intensity for ZnAc ₂ clearly indicate that Zn ²⁺ interacts more strongly with Ac ⁻ than either Ca ²⁺ or Mg ²⁺ . The dashed black spectrum corresponds to aqueous sodium acetate and is included as reference for the unbound acetate spectrum. The spectra are vertically offset for clarity.	66
5.4	Free and bound component spectra (left-hand panels A–C) and binding curves (right-hand panels D–F) for magnesium (A and D), calcium (B and E) and zinc (C and F). The inset spectra in panels D–F compare the TLS reconstruction (dotted black curves) with the experimental SC spectrum (solid green curves) obtained for a 0.5 M solution of MAc ₂ . The dot-dashed curves represent a 99% confidence interval for the binding constants.	68
6.1	Experimental (upper panels) and simulation (lower panels) results for aqueous NaOH and LiOH. Experimental Raman spectra of aqueous NaOH (A) and Raman-MCR of aqueous NaOH and LiOH (B) at 20 °C and both 0.5 M and 2 M. AIMD predictions of the distributions of Na ⁺ (C) and Li ⁺ (D) around OH ⁻ at 1 M and 25 °C . See the experimental and simulation methods for further details.	77

6.2	Comparison of the concentration (A and C) and temperature (B and D) dependent Raman-MCR hydration shell spectra of aqueous NaOH (A and B) and LiOH (C and D). The dashed curves are pure water spectra at the specified temperatures (scaled to approximately the same peak intensity).	79
6.3	Ion pair dissociation fractions x_F (A and B) and thermodynamics (C and D) obtained from concentration dependent changes in the Raman-MCR SC spectra intensity near 3500 cm^{-1} in NaOH (A and C) and LiOH (B and D) solutions at $5\text{ }^\circ\text{C}$. The experimental square points in (A) and (B) are compared with theoretical predictions obtained assuming a concentration independent ion pairing constant K_0 (match to the experimental results at infinite dilution), as well as a best fit of the experimental results to Eq. 6.3, which assumes that the ion pairing free energy decreases linearly with increasing concentration. The ion-pairing free energy ΔG , enthalpy ΔH and entropy ΔS (expressed in kJ mol^{-1}) at $20\text{ }^\circ\text{C}$ are obtained using Eqs. 6.4–6.6. The thermodynamic functions with a 0 subscript pertain to the dilute limit, and the non-subscripted functions pertain to a 1 M solution. . .	82
B.1	Measured Raman spectra (A) and Raman-MCR SC spectra (B) obtained from water and 1 mol dm^{-3} aqueous solutions of ethanol (EtOH) and 2,2,2-trifluoroethanol (TFE). The Raman spectra in (A) are unprocessed. The solid curves spectra in (B) are solute-correlated (SC) spectra of EtOH and TFE (with their experimental intensities, pertaining to the same 1 mol dm^{-3} concentration), and the inset panel shows an expanded view of the OH stretch region, compared to that of pure water (arbitrarily scaled to the same peak intensity as the EtOH SC OH band).	107
B.2	(A) Raman spectra of TFE and EtOH. (B) Raman-MCR SC spectra of TFE in EtOH, obtained from solutions with TFE concentrations of 1 mol dm^{-3} and 2 mol dm^{-3} . The inset panels show expanded views of the corresponding OH bands. The SC spectra in (B) are normalized to the same CH band intensity.	108
B.3	Temperature dependence of the dangling OH peaks in the hydration shell of MFE, DFE and TFE. These peaks were obtained from the respective minimum area non-negative SC spectra (transparent solid lines), after subtracting the background (dashed lines) using a Gaussian fit. Analogous to Figure 3.4 in Chapter 3.	109
C.1	Raman-MCR SC spectra of free (solid curves) and aggregated (dotted curves) 12HD in pure water (blue), aqueous $0.25\text{ M Na}_2\text{SO}_4$ (green), and aqueous 2 M NaSCN (red).	112
C.2	The SC $\text{C}\equiv\text{N}$ stretch band of aqueous 2 M NaSCN (dashed black curve) is compared with the $\text{C}\equiv\text{N}$ bands appearing in the concentration dependent SC spectra of 12HD.	113
C.3	The $\text{C}\equiv\text{N}$ band in aqueous NaSCN (dashed-black band) is compared with that in the SC spectrum of 12HD dissolved in 0.5 M NaSCN . Note that interaction of SCN^- with 12HD monomers at low concentration shifts the $\text{C}\equiv\text{N}$ band to higher frequency, while the interaction of SCN^- with 12HD micelles at high concentration shifts the $\text{C}\equiv\text{N}$ band to lower frequency.	113

C.4	The S=O band in aqueous Na ₂ SO ₄ (dashed-black band) is compared with that in the SC spectrum of 12HD dissolved in 0.25 M Na ₂ SO ₄ . Note that the solid curves reveal bands due to 12HD (normalized to the same CH band area), and show no evidence of a perturbed S=O band, thus confirming that there is no indication of any interaction between SO ₄ ²⁻ and either the free monomers or micelles of 12HD.	114
D.1	Family of possible bound spectra (blue shade) in the CC region obtained for MAc ₂ . All spectra shown are normalized to unit area over the CC stretch band.	123
D.2	Relative error with respect to the mean value of the binding constants estimated using the range of bound spectrum candidates shown in Figure D.1	124
D.3	Hydration-shell spectra for magnesium acetate (top), calcium acetate (middle) and zinc(II) acetate (bottom).	125
D.4	Simulated Raman spectra for acetate in pure water (black) or involved in a contact monodentate (red), contact bidentate (green) or solvent-shared (blue) ion pair with a calcium, magnesium and zinc cation.	127
D.5	Free energy profiles along the carboxylate carbon-cation distance for calcium (orange), magnesium (purple) and zinc (blue) as obtained from DFT-based ab initio MD simulations. The location of the bidentate and monodentate ion pairs is indicated with red and dashed green arrows, respectively.	129
E.1	Dissociated ion pair fractions, $x_F = I/I_0$, were fit to obtain K_0 and b , as described above. The 5 °C points are the same as those in Fig. 6.3(A and B) of Chapter 6, and the points at other temperatures were obtained from the SC spectra shown in Fig. E.2. The dotted curves are obtained using Eq. 6.2 and 6.3 with the K_0 and b values in Table E.1.	131
E.2	Concentration-dependent Raman-MCR hydration-shell spectra of aqueous NaOH (A: 10 °C and B: 40 °C) and LiOH (C: 10 °C and D: 20 °C). The dashed curves are pure water spectra at the specified temperatures (scaled to approximately the same peak intensity).	132
E.3	Raman-MCR SC spectra of aqueous (0.5 M and 2 M) NaOH and LiOH at 5 °C prior to background subtraction. The dashed curves represent the fourth-order polynomial function fit to the background points marked with black squares on the x -axis.	133
E.4	AIMD predictions of the populations of cations (A and B) or water molecules (C and D) surrounding the hydroxide ion in 1 M LiOH (red) and 1 M NaOH (green) at 25 °C. The radial distribution functions $g(r)$ (A and C) and integrated number of cations or water molecules $N(r)$ (B and D) are plotted as a function of the distance between the OH ⁻ oxygen atom and either the cation, M ⁺ , or the oxygen atom of H ₂ O	134

E.5	AIMD predictions of the distributions of H_2O around OH^- in 1 M solutions of NaOH (right panel) and LiOH (left panel) at 25 °C. The r and z axes are distances relative to the hydroxide oxygen atom located at $(r, z) = (0, 0)$	135
-----	---	-----

ABSTRACT

Raman multivariate curve resolution (Raman-MCR) spectroscopy is used to study water-mediated interactions by decomposing Raman spectra of aqueous solutions into bulk water and solute-correlated (SC) spectral components. The SC spectra are minimum-area difference spectra that reveal solute-induced perturbations of water structure, including changes in water hydrogen-bonding strength, tetrahedral structure, and formation of dangling (non-hydrogen-bonded) OH defects in a solute’s hydration shell. Additionally, Raman-active intramolecular vibrational modes of the solute may be used to uncover complementary information regarding solute–solute interactions. Herein, Raman-MCR is applied to address fundamental questions related to: (1) confined cavity water and its connection to host–guest binding, (2) hydrophobic hydration of fluorinated solutes, (3) specific ion effects on nonionic micelle formation, and (4) ion pairing in aqueous solutions.

1. RAMAN SPECTROSCOPY AND MULTIVARIATE DATA ANALYSIS

Raman spectroscopy is a scattering technique that allows access to the vibrational modes of molecules, although other frequency modes (e.g., rotational) may also be measured in a similar fashion. Generally, a monochromatic and high-intensity source of radiation, typically from a laser, is used to vibrationally excite molecules via the inelastic scattering of photons. While most of the impinging radiation on a sample is scattered without a change in photon energy, a small fraction of the incident photons is shifted up or down in frequency. These energy-shifted photons, corresponding at most to $\sim 0.001\%$ of the incident intensity,¹ produce a signature spectrum carrying both qualitative and quantitative information about the sample. For spontaneous Raman spectroscopy (as opposed to resonance Raman), the excitation wavelength should preferably not coincide with absorption bands of the sample to reduce potential fluorescence interference in the Raman spectrum.

Figure 1.1 shows in more detail the underlying principle of Raman spectroscopy. In this diagram, the sample is irradiated with a laser beam of energy $h\nu_{\text{ex}}$ (per photon). Because this laser wavelength ($\lambda_{\text{ex}} = c/\nu_{\text{ex}}$, where c is the speed of light) is usually not in resonance with an absorption band, the excited state corresponds to a *virtual* energy state (depicted by horizontal dashed lines). When a molecule scatters light elastically, the energy of the incident photon is equal to that of the emitted photon and gives rise to *Rayleigh* scattering. On the other hand, when a molecule scatters inelastically, there are two possible outcomes. One possibility is that a molecule in the vibrational ground state $v = 0$ is excited to a virtual state by an $h\nu_{\text{ex}}$ photon but emits back a photon of lower energy $h(\nu_{\text{ex}} - \nu)$. This process is called *Stokes* scattering and is followed by the vibrational transition $v = 0 \rightarrow 1$, with $h\nu$ corresponding to the energy gap between these two vibrational states. The second possible outcome occurs when a molecule initially in a vibrational excited state ($v = 1$) interacts with an $h\nu_{\text{ex}}$ photon and emits a higher energy $h(\nu_{\text{ex}} + \nu)$ photon. This last process involves the vibrational transition $v = 1 \rightarrow 0$ and corresponds to *anti-Stokes* scattering.

In this thesis, all reported Raman spectra are due to Stokes Raman scattering. This is usually the case in most Raman spectroscopic studies because Stokes lines are more intense

than the corresponding anti-Stokes ones, although specific experimental constraints may require measuring the anti-Stokes spectrum. Raman spectra are conventionally plotted as a function of wavenumber shift ($\tilde{\nu}$, cm^{-1}), corresponding to the allowed vibrational transitions of the sample, and computed using Equation 1.1:

$$\tilde{\nu} = \frac{10^7 \text{ nm}}{1 \text{ cm}} \left(\frac{1}{\lambda_{\text{ex}}} - \frac{1}{\lambda} \right) \quad (1.1)$$

where λ_{ex} and λ are the wavelength of the excitation laser and the wavelength of the Raman-scattered photons expressed in nm, respectively. Note that Stokes and anti-Stokes lines involving the same vibrational levels have wavenumber shifts of identical magnitude but opposite signs.

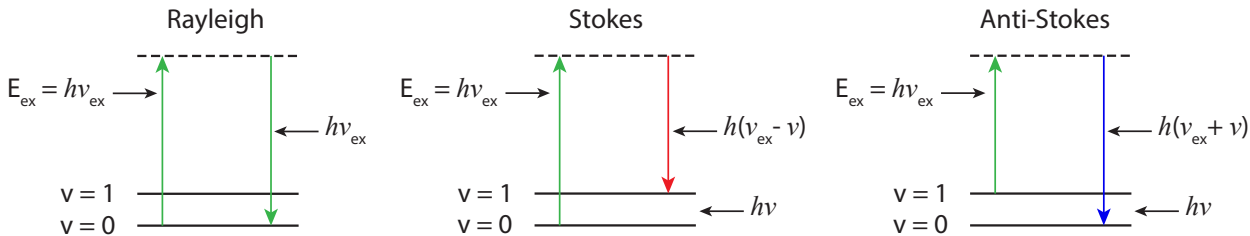


Figure 1.1. Energy level diagram illustrating the origin of Raman spectra. The horizontal dashed lines represent a *virtual* state, and $v = 0, 1$ are vibrational quantum levels separated by an energy gap $h\nu$, where h is Planck’s constant and ν is the vibrational frequency.

In chemistry, Raman spectroscopy can provide detailed information about chemical structure and molecular interactions. The study of intermolecular interactions is particularly important as these interactions directly affect chemical equilibria, structure, and dynamics. This thesis will focus on approaches that can be used to extract information about such interactions for various processes taking place in aqueous solution. We are interested in solute-induced perturbations of water structure and uncovering their relationship to processes such as host–guest binding, micelle formation, specific ion effects, and ion pairing.

Although (unprocessed) Raman spectra can *per se* provide useful information, they are often dominated by the signal of the major component in a mixture sample. Oftentimes, we are interested in extracting information about how a minor component, for example, a solute in aqueous solution, affects (or interacts with) its surroundings. In other words, we want to find out how much a solute’s hydration shell differs from bulk water and/or how much interaction there is between solute molecules. To do so, we use multivariate data analysis to separate out the two main components of the measured Raman spectra and obtain *bulk water* and *solute-correlated* spectral components. Successfully carrying out this task requires measuring spectra of exceptionally high signal-to-noise ($>1000:1$) that are amenable to such spectral decompositions. Our approach consists in a combination of Raman spectroscopy and multivariate curve resolution, constituting an experimental technique referred to as *Raman Multivariate Curve Resolution Spectroscopy*, or *Raman-MCR* for short. The following sections expand on the instrumentation and methods required for a successful implementation of Raman-MCR.

1.1 Instrumentation

All Raman measurements reported here were performed using a home-built Raman system described in detail elsewhere.^{2,3} This system includes an Ar-ion laser source (514.5 nm, ~ 20 mW of power at the sample) and a thermoelectrically cooled CCD detector (Pixis 400, 1340×400 pixels, Princeton Instruments Inc.) mounted to a 300 mm focal length imaging spectrograph (SpectraPro300i, Acton Research Inc.) with a 300 grooves/mm grating producing a dispersion of $\sim 6 \text{ cm}^{-1}$ per CCD pixel. The excitation laser light is focused in the center of a 1 cm sample cell (glass cuvette or round vial) using a $20\times$ microscope objective (Mitutoyo Inc.). The back-scattered Raman light is collected along the same optical path and delivered to the spectrograph using a fiber bundle consisting of seven $100 \mu\text{m}$ (core diameter) fibers arranged in a circular array (six around one) at the collection end and in a linear stack at the detection end. All samples are placed in a temperature-controlled cell holder and maintained at a constant temperature to within $\pm 0.01 \text{ }^\circ\text{C}$.

Wavelength calibration is performed by collecting the emission spectrum of a neon lamp before the Raman measurements. This procedure consists in correlating a set of six known Ne emission lines (shown in Figure 1.2A) with their CCD pixel of maximum intensity using a cubic polynomial. Note that the precise pixel position of each of these six Ne lines is obtained by fitting it to a Gaussian peak shape. Using the cubic calibration equation, the wavelength for each CCD pixel is calculated, and then converted into a Raman shift using Equation 1.1.

Figure 1.2B shows a typical Raman spectrum of pure water obtained with the Raman system described above. This spectrum was obtained with 5 min of integration time, which is usually a requirement to obtain high-quality spectra amenable to multivariate curve resolution. Another very important requirement of Raman-MCR is the inclusion of a reference emission line from a neon (or any other compatible) lamp in all measured spectra using appropriate band-pass filters (see high-frequency side of Figure 1.2B). This line allows for spectral alignment by shifting all measured spectra so that the Ne peaks precisely overlap with each other. Such corrections not only permit better comparisons between data obtained on different days but also provide a way to compensate for small sub-pixel wavelength shifts due to barometric pressure changes that could lead to spurious features upon spectral decomposition, especially when dealing with dilute solutions (at millimolar range or lower).

1.2 Self-Modeling Curve Resolution

Raman-MCR is a type of difference spectroscopy implemented by decomposing measured Raman spectra using multivariate curve resolution (MCR). This spectral decomposition procedure relies on the principle that any set of mixture spectra $\mathbf{D}_{m \times n}$, containing m spectra of p components measured at n wavelength channels, may be represented (in matrix notation) as a linear combination of the underlying spectral components $\mathbf{S}_{p \times n}$ as

$$\mathbf{D}_{m \times n} = \mathbf{C}_{m \times p} \mathbf{S}_{p \times n} + \mathbf{E}_{m \times n} \quad (1.2)$$

In Equation 1.2, $\mathbf{C}_{m \times p}$ is a matrix of component concentrations (or weights) and $\mathbf{E}_{m \times n}$ is a residual matrix containing (random) variance not explained by the spectral decomposition.

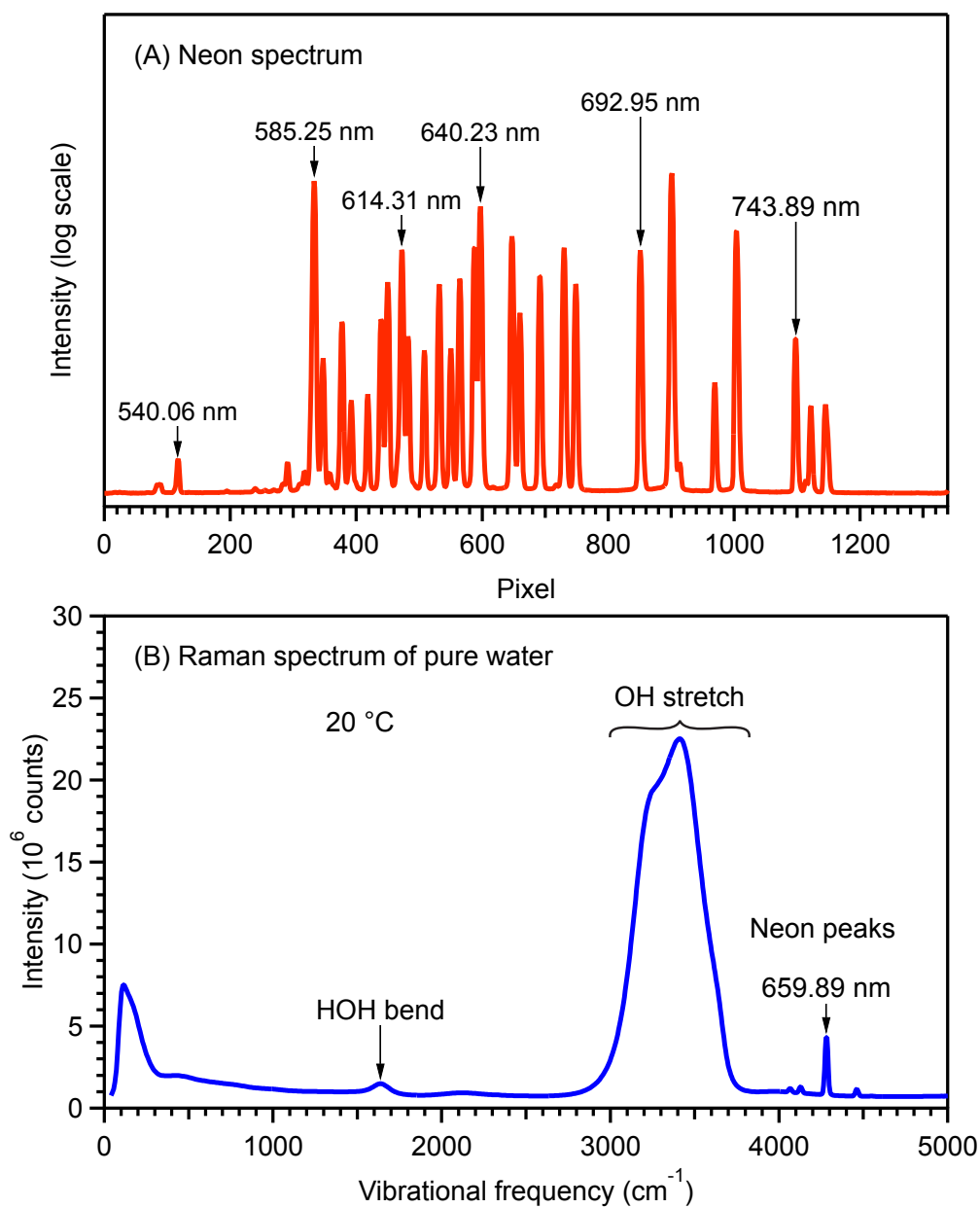


Figure 1.2. Typical neon emission spectrum (A) highlighting the emission lines used for wavelength calibration and Raman spectrum of water (B) obtained at 20 °C using the home-built Raman system.

There are multiple algorithms available for performing MCR⁴ (i.e., solving Equation 1.2 for $\mathbf{S}_{p \times n}$), but *self-modeling curve resolution* (SMCR) seems to be the most convenient for decomposing Raman spectra of two-component aqueous mixtures. SMCR is a non-iterative algorithm that starts with the well-known *singular value decomposition* (SVD) matrix factorization, which imposes no constraints other than an ordering of increasing variance for the extracted factors of a data matrix $\mathbf{D}_{m \times n}$. Although the singular values and singular vectors from SVD constitute only an abstract (purely mathematical) description of $\mathbf{D}_{m \times n}$, they can be manipulated to obtain a set of component spectra $\mathbf{S}_{p \times n}$ that contain exclusively nonnegative values, i.e., more physically meaningful spectral components. This is possible because any nonnegative spectral component should be representable as a linear combination of the underlying orthogonal eigenvectors (of the second moment matrix) spanning this vector space. This procedure was described in detail by Lawton and Sylvestre⁵ and will not be repeated here.

Raman-MCR, as implemented in this work, is performed mainly as a type of hydration-shell vibrational spectroscopy.⁶ The two spectral components that are extracted are a *bulk water* component and a *solute-correlated* (SC) component. The bulk water component is constrained to the measured spectrum of pure water, and the SC spectrum is basically equivalent to a minimum-area nonnegative difference between the measured solution and water spectra. Usually, no preprocessing is applied to the raw Raman data, although Savitzky-Golay smoothing⁷ may be performed to reduce noise when analyzing spectra of dilute solutions (especially in the millimolar range or lower).

The Raman-MCR SC spectra contain, in addition to intramolecular (Raman-active) vibrational modes of the solute, vibrational features arising from solute-perturbed water molecules (if any). Although these perturbations of water affect both the HOH bend and OH stretch, they are more evident in the OH stretch region due to higher signal-to-noise. Thus, most experimental conclusions are drawn from analyzing perturbations of the OH stretch band. These include changes in water hydrogen-bonding strength, tetrahedral structure, and formation of dangling (non-hydrogen-bonded) OH defects in a solute’s hydration shell.

Figure 1.3 illustrates the application of Raman-MCR using Raman spectra of 1 mol L⁻¹ *tert*-butyl alcohol (TBA) and water as model systems. Some significant differences may be

observed by comparing the TBA solution and pure water unprocessed Raman spectra: the solution spectrum, as expected, displays some intramolecular vibrational features of TBA superimposed to the water spectrum, such as a CH stretch band between 2850 and 3000 cm^{-1} and other smaller fingerprint bands. However, it is not obvious from these raw spectra how TBA perturbs the structure of water since only some minor changes in intensity are observed in the OH stretch region (and even smaller ones in the HOH bend region). The Raman-MCR spectra in Figure 1.3B, on the other hand, represent the two underlying components of the solution spectrum: (i) a bulk water component, corresponding to a maximum contribution of bulk water (blue curve) to the solution spectrum; and (ii) a TBA SC spectrum (red curve), containing a minimum-area nonnegative difference between the OH stretch bands of the solution and pure water spectra. Figure 1.3C shows an expanded view of the TBA

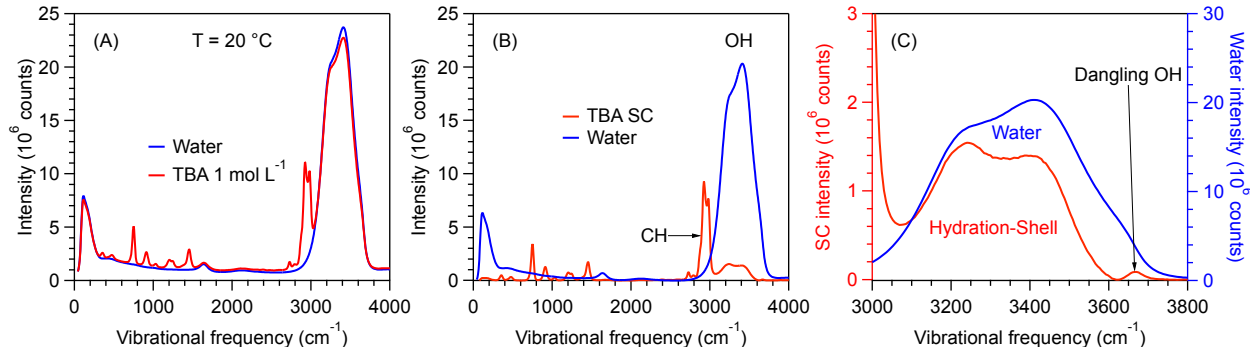


Figure 1.3. Example of a Ramam-MCR decomposition for *tert*-butyl alcohol (TBA) at 20 °C. (A) Measured Raman spectrum for pure water and 1 mol L⁻¹ TBA. (B) Raman-MCR SC component spectra obtained by decomposing the spectra shown in panel A. (C) Expanded view showing the TBA hydration-shell OH stretch and highlighting a small dangling band.

SC hydration-shell spectrum (red curve) as well as the pure water spectrum (blue curve) arbitrarily scaled for comparison. As can be seen, the hydration-shell spectrum of TBA differs significantly from the pure water spectrum. One significant difference appears as a flip of the relative intensity of the two most prominent peaks at $\sim 3200 \text{ cm}^{-1}$ and $\sim 3400 \text{ cm}^{-1}$ compared to pure water. The TBA hydration-shell spectrum shows an increase in intensity at 3200 cm^{-1} ,

implying an enhancement in tetrahedrality of the hydration shell relative to bulk water, as an increase in the tetrahedral order of water is associated with a lowering of the average OH stretch frequency.^{8,9} Another important feature of the TBA hydration-shell spectrum is the presence of a small high-frequency band at $\sim 3670\text{ cm}^{-1}$, corresponding to dangling (non-hydrogen-bonded) OH groups, which are well-known features of macroscopic air–water and oil–water interfaces but only more recently characterized in hydrophobic hydration shells using Raman-MCR.^{10–12}

The power of SMCR relies on its ability to resolve spectral components without any assumptions concerning the shapes of the underlying SC bands. However, SMCR has an inherent limitation associated with a *rotational ambiguity* that leads to multiple $\mathbf{S}_{p \times n}$ spectral profile solutions. Mathematically, this may be understood by rewriting Equation 1.2 as follows

$$\mathbf{D} = \mathbf{C}_{\text{old}} \mathbf{S}_{\text{old}} = (\mathbf{C}_{\text{old}} \mathbf{M}) (\mathbf{M}^{-1} \mathbf{S}_{\text{old}}) = \mathbf{C}_{\text{new}} \mathbf{S}_{\text{new}} \quad (1.3)$$

where \mathbf{M} is any nonsingular matrix. Therefore, any set of solutions (\mathbf{C}_{old} and \mathbf{S}_{old}) may be transformed into new solutions (\mathbf{C}_{new} and \mathbf{S}_{new}) that equally well represent the original data matrix \mathbf{D} .

In the context of hydration-shell spectroscopy, rotational ambiguity may be traced to an ambiguity in establishing a solvation-shell boundary. In other words, the minimum-area SC spectrum does not necessarily include all water molecules in the first hydration shell of the solute, and may be interpreted as arising only from water molecules that are most perturbed by the solute. To account for the full first hydration shell, a new SC component spectrum may be constructed by extending its boundary farther out from the solute. This can be accomplished by using complementary information either from other experiments or simulations that provide estimates of the number of water molecules comprising the first hydration shell around the solute.

A final note regarding SMCR is that it is formally limited to two-component analyses. For instance, if an SMCR analysis is performed on a multicomponent aqueous system, the SC spectra will be dominated by hydration-shell features of the component that most strongly perturbs the structure of water. To bypass this limitation, such multicomponent systems

may be effectively reduced to a two-component analysis by varying the concentration of one component at a time.

1.3 Organization of the Thesis

This thesis describes applications of Raman multivariate curve resolution (Raman-MCR) spectroscopy to fundamental questions related to host-guest binding, self-assembly, hydrophobic hydration, and ion-pairing in aqueous solutions. Each one of these topics and corresponding main results appear in separate chapters as briefly described below.

Host-guest binding: In Chapter 2, we designed a method to determine the vibrational spectrum of “high energy” water molecules present inside the cavity of β -cyclodextrin. The displacement of cavity water molecules has been suggested as a driving force for host-guest binding, but no previous work had reported experimental observations of the structure of water in such nonpolar host cavities in aqueous solution. Using Raman-MCR, we found that the cavity water in β -cyclodextrin has slightly greater tetrahedrality and fewer weak hydrogen bonds than bulk water. These findings may constitute an important factor to consider, e.g., in supramolecular chemistry, when modelling and/or designing host molecules for drug delivery.

Hydrophobic hydration: In Chapter 3, we used Raman-MCR combined with molecular dynamics simulations to compare the hydration shell structure of methyl and fluorinated methyl groups. We demonstrated that the hydration shell of a fluorinated methyl group has a significantly higher number of water dangling OH defects than the hydration shell of a $-\text{CH}_3$ group. This was a surprising result, and we demonstrated that it originates from the C–F bond polarity that disrupts the water structure via attractive solute–water interactions. In the case of $-\text{CF}_3$, these results contrast to classical theories of hydrophobicity that predict similar interactions of water with both alkyl and perfluoroalkyl groups after accounting for their volume difference. These results suggest that $-\text{CF}_3$ is not a typical hydrophobe, particularly under low hydration conditions, e.g., under confinement in protein-binding pockets or in crevices on the protein surface.

Self-assembly: In Chapter 4, Raman-MCR was applied to study micelle formation. For this process, Raman-MCR spectra contains a wealth of information that helps clarifying questions

related to the hydration of non-ionic micelles and specific ion effects. We used MCR to obtain an estimate of the critical micelle concentration (cmc) and extract the micelle-correlated spectrum. We quantified how much chaotropic (SCN^-) and kosmotropic (SO_4^{2-}) ions alter the cmc and have obtained a spectroscopic signature for the different behaviors. These micelle studies contribute new knowledge on micelle structure and hydration that may have implications in drug delivery, oil recovery, and environmental remediation applications.

Ion pairing: In Chapter 5, Raman-MCR was applied to study ion pairing in aqueous acetate solutions. In spite of the biological importance of the binding of Zn^{2+} , Ca^{2+} , and Mg^{2+} to carboxylate anions, previous experimental and computational studies have obtained conflicting results regarding the corresponding binding affinities. We demonstrated the first use of Raman-MCR to obtain self-consistent free and bound acetate spectra and one-to-one binding constants, without any *a priori* assumptions regarding the shapes of the corresponding vibrational bands. The experimental results, combined with classical molecular dynamics simulations with a charge-scaled force field and *ab initio* simulations, indicate that the measured binding constants pertain to direct contact (as opposed to water separated) ion pairing. In Chapter 6, Raman-MCR was used to probe the structure of ion pairs in aqueous solutions of NaOH and LiOH. We have found that the initially formed ion pairs are predominantly water-shared with the hydroxide ion retaining its full first hydration shell, while direct contact ion pairing only becomes significant at higher concentrations. Moreover, temperature-dependent measurements imply that the ion pairing free energies have an approximately linear (rather than square-root) concentration dependence and are enthalpically disfavored and entropically favored to a degree that increases with increasing concentration.

2. CAVITY HYDRATION AND COMPETITIVE BINDING IN METHYLATED β -CYCLODEXTRIN

A version of this chapter was published in a peer-reviewed journal as:

Mendes de Oliveira, D.; Ben-Amotz, D. Cavity hydration and competitive binding in methylated β -cyclodextrin. *J. Phys. Chem. Lett.* **2019**, *10*, 2802–2805.

Abstract. Raman multivariate curve resolution (Raman-MCR) spectroscopy is used to measure the vibrational spectrum of water molecules in the cavity of an aqueous methylated β -cyclodextrin (Me- β -CD), as well as to quantify the competitive expulsion of those water molecules by benzene. The Me- β -CD cavity is found to contain 5–6 water molecules whose structure is remarkably similar to bulk water, although slightly more tetrahedral and with fewer weak hydrogen bonds. The binding constant of benzene to Me- β -CD, obtained using Raman-MCR, is found to be similar to that of benzene to β -CD (previously determined by other means). The competitive displacement of water by benzene in Me- β -CD is quantified by explicitly including the release of cavity-bound water molecules in the measured equilibrium constant.

2.1 Introduction

Displacement of “high-energy” water from a nonpolar host cavity has been proposed as a driving force for supramolecular host–guest binding processes.^{13,14} For instance, it has been suggested that liberation of water from cyclodextrin (CD) cavities leads to an enthalpy gain because the expelled water molecules can form better hydrogen bonds in the bulk medium than inside the nonpolar cavity.¹⁵ In addition, calorimetric measurements and molecular dynamics (MD) simulations of binding in cucurbiturils have found a correlation between the number of water molecules in the unbound host cavity and their binding constants.^{16,17} However, no previous studies have reported direct experimental observations of the structure of water in such nonpolar host cavities in aqueous solution. Here, we do so by combining Raman spectroscopy and multivariate curve resolution (Raman-MCR) to measure the hydration-shell

vibrational spectra of water-filled and benzene-filled methylated β -cyclodextrin (Me- β -CD) host molecules. Our results reveal that there are 5–6 water molecules in the unbound Me- β -CD host, in reasonable agreement with values inferred from previously reported MD simulations^{13,18–20} as well as the crystal structure²¹ of nonmethylated β -CD. Moreover, our results show that the cavity-bound water has a structure that is quite similar (but not identical) to bulk water. In addition, we demonstrate that Raman-MCR may be used to determine the binding constant of benzene to Me- β -CD and find that it is comparable to that for benzene binding to nonmethylated β -CD. We also discuss the implications of the results regarding the competitive displacement of cavity-bound water molecules by benzene.

Previous MD simulations of various aqueous cavities predict that stable hydrogen-bonded water clusters can be formed inside cavities of diameters larger than ~ 1 nm, while smaller nonpolar cavities, which could accommodate up to 4 water molecules, may remain dry in an equilibrated aqueous solution.²² These predictions are consistent with MD simulations of a synthetic host whose hydrophobic cavity was found to fluctuate between completely empty and water-filled states with an average of 4.5 bound water molecules.²³ These predictions are also supported by experimental NMR²⁴ and x-ray²⁵ structure measurements of hydrated proteins with dry nonpolar cavities. Another experimental x-ray and neutron diffraction study of a self-assembled framework with very large (~ 27 nm³) nonpolar (aromatic) cavities revealed that the cavities are filled by an ice-like water structure.²⁶ Other studies have suggested that the “high-energy” water molecules inside nonpolar cavities resemble a supercritical fluid^{13,27} or may undergo vapor–liquid (drying) fluctuations.²⁸ Different MD simulation studies of aqueous β -CD have predicted an average of as few as ~ 4 or as many as ~ 7 water molecules inside its cavity, while an experimental neutron diffraction study found ~ 6 cavity-bound water molecules in crystalline β -CD, whose structure is more ordered than that of interstitial water molecules.²¹ Additionally, a simulation study has predicted that alkylation of β -CD does not significantly change its overall cavity size and water occupancy.¹⁹

Here we probe the structure of the cavity-bound water molecules in Me- β -CD by measuring the change in its hydration-shell spectrum upon displacing the cavity-bound water molecules by benzene-d₆. Previous Raman-MCR studies of aqueous benzene solutions have found that its hydration-shell spectrum consists of only a relatively small and narrow high-frequency

peak at $\sim 3610\text{ cm}^{-1}$ assigned to a π -hydrogen bond between water and benzene². Previous UV spectroscopy, vapor pressure, and calorimetric studies found that benzene binds to all cyclodextrins with binding constants ranging from $\log K = 0.96$ in γ -cyclodextrin²⁹ to $\log K = 1.93\text{--}2.23$ in β -cyclodextrin^{29,30} at ambient conditions. Thus, the displacement of cavity-bound water molecules by benzene should make it possible to obtain the Raman spectrum of the displaced water molecules. The following is a more detailed description of how we used this strategy to determine the number and structure of cavity-bound water molecules, and to quantify the competitive displacement of water by benzene in the Me- β -CD cavity.

2.2 Experimental Details

Sample Preparation and Raman Spectra Collection. Aqueous solutions of benzene- d_6 (Sigma Aldrich) and heptakis(2,6-di-O-methyl)- β -cyclodextrin (Sigma-Aldrich) were prepared with ultrapure filtered water (Milli-Q UF Plus, $18.2\text{ M}\Omega\text{ cm}$). Raman spectra were obtained at $20\text{ }^\circ\text{C}$ using an Ar-ion 514.5 nm laser with $\sim 20\text{ mW}$ of power at the sample and 5 min of integration time. Backscattered Raman photons were collected from the sample using a $20\times$ long-working-distance microscope objective ($\text{NA} = 0.42$, Mitutoyo Inc.) and transmitted with an optical fiber bundle to an imaging spectrograph (Acton Research Inc.) equipped with a 300 grooves/mm grating and a CCD camera (Princeton Instruments Inc.).

Raman-MCR Spectra. Self-modeling curve resolution (SMCR)^{3,5,8,31} was used to obtain Raman-MCR solute-correlated (SC) spectra of the free and bound aqueous host and guest molecules. The resulting SC spectra contain spectral features arising from intramolecular vibrational modes of the solute as well as from solvent molecules whose vibrations are perturbed by the solute. The pure water spectral component is constrained to the experimentally measured water spectrum while the SC component is equivalent to the minimum-area (non-negative) difference between the solution and pure water spectra. Note that it is particularly important to assure that the MCR input spectra are obtained under identical experimental conditions. Specifically, the temperatures of the two samples should be the same to within at least $0.1\text{ }^\circ\text{C}$, and wavelength changes resulting from barometric pressure variations need

to be compensated by including a reference spectral line (e.g., a helium lamp line) in each measured Raman spectrum. In practice, obtaining properly converged SC spectra requires accurately establishing the background underlying the SC peaks of interest using either a linear or quadratic fit to the local background in the spectrum.

2.3 Results and Discussion

Figure 2.1A shows the measured Raman spectra of pure water and an aqueous 0.1 M Me- β -CD solution with and without deuterated benzene. Benzene-d₆ was used as the guest in order to distinguish its C–D stretch band from the C–H band of the host. The binding of benzene to the Me- β -CD leads to a change in both the average frequency and intensity of the benzene-d₆ C–D stretch band near 2300 cm⁻¹ and induces shifts in the Me- β -CD C–H stretch band near 2900 cm⁻¹.

Figure 2.1B shows Raman-MCR SC spectra obtained from aqueous Me- β -CD with concentrations ranging from 0.025 M to 0.2 M (as well as pure water). All the SC spectra are normalized to the Me- β -CD C–H stretch band area. The fact that the resulting Me- β -CD SC spectra are essentially concentration independent provides strong evidence of the lack of any significant aggregation of Me- β -CD over this concentration range.

Figure 2.1C compares the SC spectra of the free and benzene-complexed Me- β -CD and benzene-d₆, and the inset panels show expanded views of the associated SC O–H stretch bands. The Me- β -CD SC O–H stretch bands arise from perturbation of the vibrational structure of the entire hydration-shell of Me- β -CD (as well as from OH groups of Me- β -CD itself). Free benzene has essentially no hydration-shell (on this scale), as indicated by the red curve in Figure 2.1C (and the expanded view in the lower inset panel). This free benzene contribution has been subtracted from the SC spectrum of the aqueous Me- β -CD+C₆D₆ solution (orange curve). The SC spectrum of the free Me- β -CD host (purple curve) in Figure 2.1C is the same as the 0.1 M SC spectrum in Figure 2.1B. Thus, the difference between the purple and orange curves in Figure 2.1C represents the spectrum of the water molecules that were present in the free Me- β -CD cavity before they were displaced by benzene.

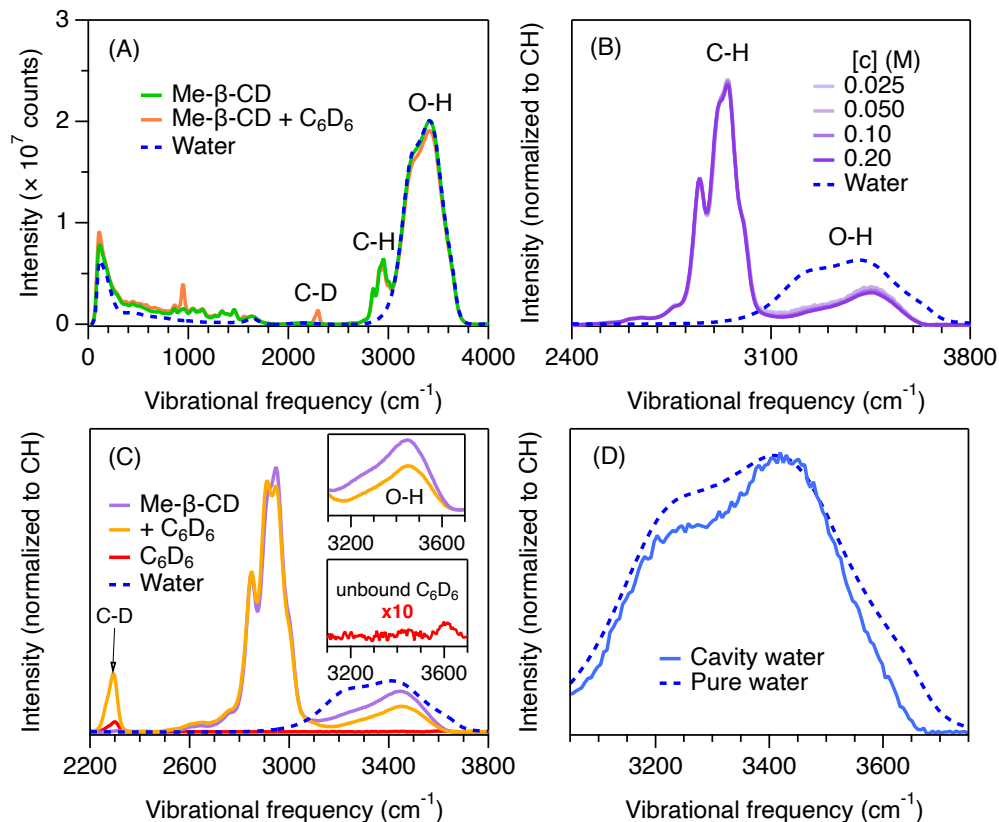


Figure 2.1. (A) Raman spectra of pure water, 0.1 M Me- β -CD, and 0.1 M Me- β -CD + benzene- d_6 . (B) Hydration-shell spectra of Me- β -CD at different concentrations. (C) Hydration-shell spectra of Me- β -CD with and without benzene- d_6 (with inset panels showing expanded views of the O-H stretch region). (D) Comparison of the O-H stretch bands of cavity-bound (solid blue) and pure liquid (dashed blue) water molecules. The cavity-bound O-H band is obtained from the difference between the purple and orange O-H bands in (C).

Figure 2.1D compares the resulting O-H stretch bands of the cavity-bound water (solid blue curve) and pure water (dashed blue curve). The similarity of the two O-H stretch bands indicates that the structure of the cavity-bound water is similar to liquid water. The slightly lower average O-H band frequency (by $\sim 9 \text{ cm}^{-1}$) of the cavity-bound water suggests that these water molecules are slightly more tetrahedrally ordered than bulk water, as previous studies have demonstrated a strong correlation between average O-H frequency and tetrahedral order.⁸ Moreover, the high frequency edge of the cavity-bound water O-H band begins near

3650 cm^{-1} , while that for pure water begins at a higher frequency of $\sim 3700 \text{ cm}^{-1}$, thus implying that there are fewer weak H-bonds in the cavity-bound water than in bulk water.

In order to quantify the number of water molecules in the Me- β -CD cavity, we need to know the number of host molecules that contain a bound benzene, which requires determining the equilibrium constant for this host/guest binding process. Although the binding constant of benzene to (non-methylated) β -CD has previously been measured, there are no previous reports of the binding constant of benzene to Me- β -CD. However, some β -CD derivatives (e.g., hydroxypropyl- β -CD) have been found to have benzene binding constants that are similar to those for β -CD while others (e.g., β -CD-thioethers) were found to differ significantly.³² Here we quantify the binding constant of benzene to Me- β -CD using Raman-MCR. To the best of our knowledge, this is the first such Raman-based determination of a host-guest binding constant.

Given the low aqueous solubility of benzene, we found it advantageous to perform the binding constant measurement in a way that differs somewhat from previously employed spectrometric titration procedures.³³ Our strategy relied on first obtaining Raman-MCR spectra from solutions that were equilibrated with a liquid benzene phase that remained continuously in contact with either 1 mL of pure water or 1 mL of 0.1 M Me- β -CD. Thus, both equilibrated solutions necessarily have approximately the same saturated concentration ($\sim 23 \text{ mM}$)^{34,35} of free (unbound) benzene. The SC spectrum of unbound benzene in water (red curve in Figure 2.1C) was obtained from an SMCR decomposition of the spectra of a saturated aqueous benzene solution and pure water, as previously reported.² The SC spectrum of the cavity-bound benzene host-guest complex was obtained from an SMCR decomposition of the 100 mM Me- β -CD solution in equilibrium with benzene and a separate saturated aqueous solution of benzene (treated as the solvent). Thus, the benzene- d_6 features in the resulting SC spectrum should pertain only to the host-guest complex (with no contribution from the unbound benzene- d_6). Our results reveal that the benzene- d_6 C–D band frequency decreases by $\sim 7 \text{ cm}^{-1}$ (and increases in intensity by $\sim 40\%$) upon binding to the Me- β -CD cavity (as further described below).

Figure 2.2A shows the C–D stretch band spectra of the free (dashed blue) and bound (dashed orange) benzene- d_6 , along with spectra obtained from solutions consisting of a

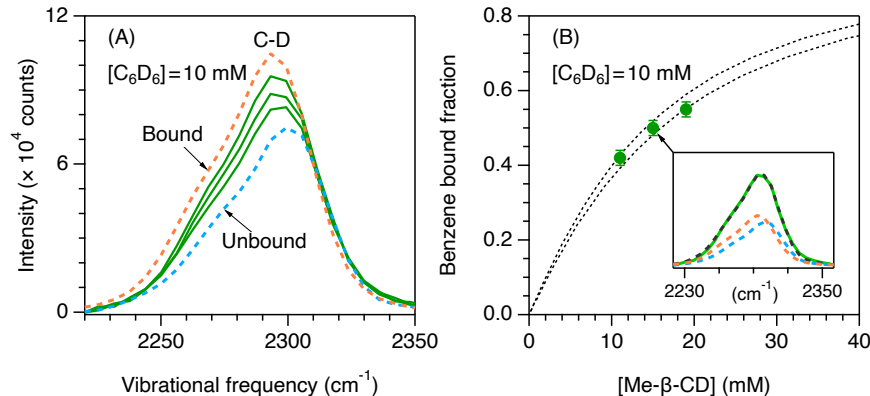


Figure 2.2. Spectroscopic determination of the host-guest binding equilibrium constant and Raman cross section ratio of bound and unbound benzene-d₆ (guest), all of which have a total benzene-d₆ concentration of 10 mM. (A) The C–D stretch bands of the free (dashed blue) and bound (dashed orange) benzene-d₆ are compared with those obtained from mixtures containing total Me-β-CD (host) concentrations of 10 mM, 15 mM and 20 mM. (B) The fraction of bound benzene-d₆ (points) are plotted as a function of total Me-β-CD concentration and compared with binding curves pertaining to $K = 92$ and 110 . The inset panel in (B) shows the TLS reconstruction (dashed curves) of the measured (solid green curve) guest C–D stretch band pertaining to the middle point.

mixture of free and bound benzene-d₆ (solid green) in solutions containing a total Me-β-CD concentration of 10 mM, 15 mM, and 20 mM. All the C–D stretch bands in Figure 2.2A pertain to a total benzene-d₆ concentration of 10 mM. The difference in intensity between the bound and free benzene-d₆ bands indicates that the Raman cross section of benzene-d₆ increases by a factor of 1.4 ± 0.1 upon binding to Me-β-CD, as obtained directly from the measured spectra of the above solution, as well as the solutions saturated with benzene-d₆ (as described in Appendix A.2).

Figure 2.2B shows the fraction of bound benzene-d₆ as a function of total Me-β-CD concentration, obtained by performing a total-least-squares (TLS) fit of each of the solid green bands in Figure 2.2A to a linear combination of the corresponding free and bound component bands (as further described in the Appendix A.1). The inset panel in Figure 2.2B shows the resulting free and bound component intensities obtained from such a TLS fit to the spectrum obtained with a total benzene concentration of 10 mM and a total Me-β-CD

concentration of 15 mM. The good agreement between the reconstructed (dashed black) band and the measured (solid green) band confirms the accuracy of the TLS fit. The two dotted black curves in Figure 2.2B indicate binding curves pertaining to binding constants of $K = 92$ (1/M) and 110 (1/M), respectively, whose average is $K = 101 \pm 10$ (1/M) (or $\log K = 2.00 \pm 0.05$). Note that this binding constant is quite similar to the $1.93 < \log K < 2.23$ binding constants previously obtained (by other means) for benzene binding to non-methylated β -CD.^{29,30}

2.4 Conclusions

In summary, Raman-MCR has been used to obtain the spectrum of cavity-bound water molecules in Me- β -CD, as well as the binding constant associated with the displacement of those water molecules by benzene- d_6 . The results indicate that the cavity-bound water molecules have a structure that is quite similar to liquid water, although with slightly greater tetrahedrality and fewer weak H-bonds. The benzene binding constant of $\log K \approx 2$ implicitly pertains to a process in which benzene displaces cavity-bound water molecules, although those are not included in defining the equilibrium as $H + G \rightleftharpoons HG$, and thus $K = [HG]/[H][G]$. To quantify the relative binding affinities of benzene and water, it is necessary to express the equilibrium constant in a form that explicitly includes the cavity-bound (and displaced) water molecules, $K' = [HG][H_2O]^n/[H(H_2O)_n][G]$, where $5 \leq n \leq 6$ is the number of cavity-bound water molecules, and $K' = K[H_2O]^n$ (obtained as further described in Appendices A.2 and A.3). Note that the number of cavity-bound water molecules is obtained assuming that the water Raman cross section is not changed upon binding (and thus the number of cavity-bound water molecules would decrease if there were a binding-induced increase in the Raman cross section of water, as we have found to be the case for benzene). The K' equilibrium constant implies that, if the unbound water and benzene were (hypothetically) scaled to the same 1 M concentration, then the fraction of benzene-filled to water-filled Me- β -CD cavities would be of the order of $K' \sim 10^{12}$, which corresponds to a partial molar Gibbs energy difference of $\sim RT \ln[10^{12}] \approx 70$ kJ/mol between the water-filled and benzene-filled Me- β -CD cavity.

With regard to the influence of “high energy” water molecules in host–guest binding, it is important to note that the cavity-bound water molecules in an equilibrium aqueous

solution necessarily have the same chemical potential (partial molar Gibbs energy) as the surrounding liquid water. Since the same is true for any aqueous host–guest binding process, the differences between any such competitive water-displacement processes are necessarily dictated by differences between the partial molar free energies of the unbound and bound host and guest molecules rather than by that of the cavity-bound water molecules in the unbound host. More specifically, host–guest binding equilibria can only be influenced by binding-induced changes in host–guest and solute–water interactions, and cannot be affected by binding-induced changes in water–water energy and entropy, which are necessarily precisely compensating.^{14,36}

3. EFFECTS OF FLUORINATION ON HYDRATION-SHELL THERMODYNAMICS AND SOLUTE–WATER INTERACTIONS

Large portions of this chapter are from the following two publications:

Robalo[†], J. R.; Mendes de Oliveira[†], D.; Imhof, P.; Ben-Amotz, D.; Vila Verde, A. Quantifying how step-wise fluorination tunes local solute hydrophobicity hydration shell thermodynamics and the quantum mechanical contributions of solute–water interactions. *Phys. Chem. Chem. Phys.* **2020**, 22, 22997–23008. [†]**These authors contributed equally.**

Robalo, J. R.; Streacker, L. M.; Mendes de Oliveira, D.; Imhof, P.; Ben-Amotz, D.; Verde, A. V. Hydrophobic but water-friendly: Favorable water–perfluoromethyl interactions promote hydration shell defects. *J. Am. Chem. Soc.* **2019**, 141, 15856–15868.

Abstract. Partial or complete fluorination of a molecule is commonly used to tune its hydrophilic/hydrophobic character. However, the influence of fluorination on hydration-shell structure and thermodynamics remains unclear. In fact, the connection between i) the hydrophobicity of a functional group; ii) the local structure and thermodynamics of its hydration shell; and iii) the relative influence of van der Waals (dispersion) and electrostatic interactions on hydration is yet to be established. We investigate this connection using spectroscopic, classical simulation and *ab initio* methods by following the transition from hydrophile to hydrophobe induced by the step-wise fluorination of methyl groups. Along the transition, we find that water–solute hydrogen bonds are progressively transformed into dangling hydroxy groups. Each structure has a distinct thermodynamic, spectroscopic and quantum-mechanical signature connected to the associated local solute hydrophobicity and correlating with the relative contribution of electrostatics and dispersion to the solute–water interactions.

3.1 Introduction

The perfluorination of hydrocarbons or alkyl substituents often increases their hydrophobicity as evidenced, for example, by the decreased solubility of methane (CH_4) upon fluorination (to CF_4)³⁷ and the increased aqueous contact angle of polyethylene (PE) upon fluorination

(to PTFE).³⁸ Interestingly, while mostly absent from biological systems, introduction of fluorine into synthetic biology results in a remarkable ability to manipulate cellular machinery,^{39–42} structural motifs^{43–45} and compartments.^{46,47} In aqueous chemistry, the associated minimal changes to molecular surface area and the retention of molecular topology upon fluorination result in a minimal volume-induced structural perturbation of the hydration water molecules.⁴⁸ Predictively understanding the influence of fluorination on aqueous processes requires quantifying the associated solute–water interactions, as those interactions determine hydration free energies and thus also the influence of water on folding and binding processes.⁴⁹ Although previous infrared spectroscopic studies have provided intriguing hints regarding the influence of fluorination on hydration,^{50,51} they have not quantified the associated changes in hydration-shell structure and thermodynamics. Here we do so by combining Raman multivariate curve resolution (Raman-MCR) spectroscopy with classical molecular dynamics (MD) simulations and *ab initio* interaction energy calculations. Our Raman-MCR spectra reveal striking differences between the hydration-shell structures of ethanol (EtOH), 2-fluoroethanol (MFE), 2,2-difluoroethanol (DFE), and 2,2,2-trifluoroethanol (TFE) dissolved in water. Comparisons of those experimental results with molecular dynamics simulation predictions obtained using classical force fields facilitate the definitive assignment of the observed fluorination-induced hydration-shell structure changes, quantitatively link those changes to hydration thermodynamics, and establish the electrostatic origin of these changes.

We found that the population of non-hydrogen-bonded (“dangling”) water hydroxy (OH) groups at the water–solute interface provides a sensitive means of quantifying and understanding how fluorination alters hydration-shell structure and thermodynamics. Prior studies have reported the presence of such dangling OH structures, detectable as a vibrational peak near 3650 cm^{-1} ,^{10,52–58} both at macroscopic and molecular hydrophobic interfaces. At macroscopic air–water and oil–water interfaces, experiments and simulations suggest that 20–30 % of the interfacial water molecules have one dangling hydroxy.^{10,52,56,57,59–65} In molecular hydrophobic hydration shells, the dangling OH structures have about a 10 times lower probability (per first hydration-shell water molecule)¹² but increase with increasing n-alcohol chain-length⁵⁴ and with increasing solute negative partial charge.^{54,66} In this work, we present both experimental and theoretical results revealing the marked increase in the

hydration-shell dangling OH population upon fluorination of the terminal methyl group of ethanol. We further show that this increased population is due to the negative partial charge of the F atoms, which electrostatically stabilize the hydration-shell dangling OH structures. Along with the fact that the fluoromethyl groups range from hydrophilic ($-\text{CH}_2\text{F}$) to hydrophobic ($-\text{CF}_3$), the thermodynamic signature of these hydrogen bond-like structures leads to a distinction between enthalpically stabilized, *de facto* hydrogen bonds (in MFE), entropically stabilized (for this reason termed “dangling”) hydroxy groups (in TFE), and hybrid structures (in DFE). Likewise, the quantum mechanical nature of the solute–water attractive interactions also varies along the hydrogen bond to dangling hydroxy transition, further supporting a fundamental distinction between structurally similar hydration shell features.

3.2 Experimental Methods

Aqueous solutions of EtOH (200 proof, anhydrous, Decon Laboratories), MFE ($\geq 95\%$, Alfa Aesar), DFE ($> 98\%$, Tokyo Chemical Industry), and TFE (99.8%, Acros Organics) were prepared using ultrapurified water (Milli-Q UF plus, Millipore Inc., resistivity of 18.2 M Ω cm). In view of toxicity, all fluorinated alcohol solutions were prepared in a fume hood and enclosed in sealed glass vials for Raman acquisition. Raman spectral measurements were performed as previously described^{2,3} at temperatures between 20 °C and 80 °C (held constant to within less than ± 0.1 °C) using an Ar-ion 514.5 nm excitation laser with ~ 20 mW of power at the sample and 5 min of integration time.

Self-modeling curve resolution (SMCR)^{3,5,31} was used to obtain minimum-area non-negative solute-correlated (SC) spectra from pairs of pure water and solution spectra collected under identical experimental conditions (as described above). Any residual baseline in the SC spectra was removed using either a linear or quadratic polynomial fit to selected background points adjacent to the Raman bands of interest. The dangling OH peaks, corresponding to water OH groups that do not participate in a normal water–water hydrogen bond, were identified in the SC spectra and quantified as previously described.⁵⁴ Assuming that the Raman scattering cross section of a dangling OH is equal to the average Raman cross section

of an OH group in pure water, we can obtain the average number $\langle k \rangle$ of those species using the following expression:

$$\langle k \rangle = \left(\frac{2[W]}{[S]} \right) \left(\frac{I_{\text{D-OH}}}{I_{\text{W-OH}}} \right) \quad (3.1)$$

where $I_{\text{D-OH}}$ corresponds to the integrated area (measured counts) of a water dangling OH band, $I_{\text{W-OH}}$ is the integrated area of the OH band of pure water, $2[W]$ ($\approx 2 \times 55.5 \text{ mol dm}^{-3} = 111 \text{ mol dm}^{-3}$) is the concentration of OH groups in pure water, and $[S]$ is the solute concentration in mol dm^{-3} units.

A more general procedure for obtaining $\langle k \rangle$ relies on dividing the SC spectrum by the area of a solute intramolecular vibrational band, such as the CH stretch. In such a normalized spectrum, the dangling OH intensity is given by $I_{\text{D-OH}}^{\text{CH-n}} = I_{\text{D-OH}}/I_{\text{CH}}$. This last quantity can be directly translated into $\langle k \rangle$ given the values of the Raman cross sections of a CH group (Ω_{CH}), a water OH group (Ω_{OH}), and the number of CH bonds (n_{CH}) in a solute molecule, as follows:

$$\langle k \rangle = n_{\text{CH}} \left(\frac{\Omega_{\text{CH}}}{\Omega_{\text{OH}}} \right) I_{\text{D-OH}}^{\text{CH-n}} \quad (3.2)$$

The ratio $\Omega_{\text{CH}}/\Omega_{\text{OH}}$ in Equation 3.2 is estimated using the measured area of the OH band in pure water ($I_{\text{W-OH}}$), the measured area of the CH band (I_{CH}) in the solute, and the concentrations of pure water and solute, as shown below:

$$\frac{\Omega_{\text{CH}}}{\Omega_{\text{OH}}} = \left(\frac{I_{\text{CH}}}{I_{\text{W-OH}}} \right) \left(\frac{2[W]}{n_{\text{CH}}[S]} \right) \quad (3.3)$$

Note that Equation 3.2 is preferred over Equation 3.1 because normalization of the SC spectrum to the solute CH band area compensates for any variations in laser intensity (or drifts in optical alignment) that may occur during the Raman spectral acquisition process. Moreover, Equation 3.2 may also be used to correct the value of $\langle k \rangle$ for any difference between the Raman cross section of the dangling OH group and an average OH group in pure water. For example, previously reported calculations have predicted that some dangling OH groups may have a Raman cross section that is approximately half that of an average OH group in pure water.⁵⁴ If that is assumed to also be the case for the dangling OH groups interacting with a solute fluorine atom, then the appropriate value of $\Omega_{\text{CH}}/\Omega_{\text{OH}}$ should be increased by

a factor of two (relative to the value obtained using Equation 3.3) and thus the resulting values of $\langle k \rangle$ (obtained using Equation 3.2) would also increase by about a factor of two.

To obtain the dangling OH formation thermodynamics, we consider the process of forming one such dangling OH defect structure in a hydration shell that initially contained no dangling OH defects. This transformation was previously described using a lattice model,⁵⁴ which predicts that, as long as the dangling OH defect formation has a relatively low probability of occurrence (such that $\langle k \rangle < 1$), the equilibrium constant K for the dangling OH formation process should be well approximated by $\langle k \rangle$. Thus, the following expressions may be used to obtain the Gibbs energy, enthalpy, and entropy changes associated with the formation of dangling OH defects in the hydration shell of the solute (where R is the gas constant and T is the absolute temperature):

$$\Delta G = -RT \ln \langle k \rangle \quad (3.4)$$

$$\Delta H = \left[\frac{\partial(\Delta G/T)}{\partial(1/T)} \right]_P \quad (3.5)$$

$$\Delta S = - \left(\frac{\partial \Delta G}{\partial T} \right)_P \quad (3.6)$$

3.3 Computational Methods

All computational results presented in this chapter were obtained by our collaborators (Dr. Ana Vila Verde and Dr. João Robalo) at the Max Planck Institute. The description of the computational methods can be found in our published work.^{67,68} The computational work included classical molecular dynamics (MD) simulations that quantified two types of non-water-bonded hydroxy structures in the hydration shell of ethanol and fluorinated ethanol, as schematically shown in Figure 3.1. The sum of the populations of these two structures were found to represent the dangling OH population quantified experimentally. After determining the average number of dangling OH groups, $\langle k \rangle$, from the simulations, Equations 3.4, 3.5 and 3.6 were used to obtain the Gibbs energy ΔG , enthalpy ΔH , and entropy ΔS of dangling OH formation. Additionally, symmetry-adapted perturbation theory (SAPT) was used to quantify and decompose the interaction energy between one alcohol

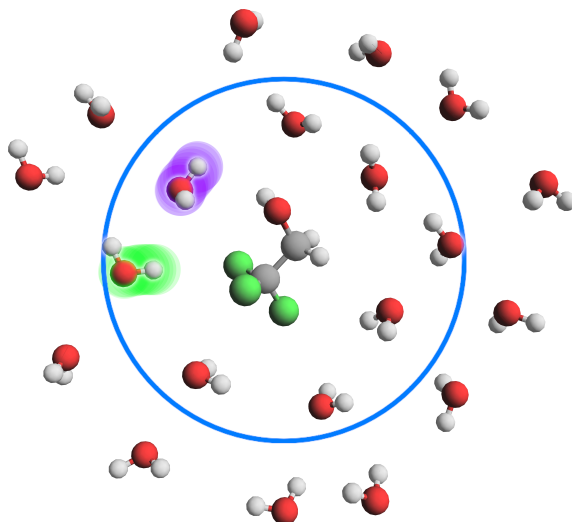


Figure 3.1. A schematic representation of the hydration shell of TFE. A hydroxy group forming a hydrogen bond-like structure is highlighted in green, a free hydroxy group is highlighted in purple; we refer to both structures jointly as non-water-bonded hydroxy groups. Carbon atoms are shown in gray, fluorine in green, oxygen in red and hydrogen in white. The solute and the first hydration shell waters are encircled in blue.

molecule and one water molecule, in configurations selected from MD simulations of a single solute in a water box at 298 K. The intermolecular interactions were evaluated in two types of configurations: those in which the water molecule forms a hydrogen bond-like structure with the solute, and, for comparison, those in which this structure does not exist.

3.4 Results and Discussion

Experimental results. Figure 3.2A shows unprocessed Raman spectra obtained at 20 °C for 1 mol dm⁻³ solutions of MFE, DFE, and TFE, and pure water. A slightly higher background is present in the spectrum of MFE due to fluorescence as this sample is less pure than the other two fluorinated alcohol samples. This level of interfering fluorescence is not detrimental to our analysis given that it can be effectively removed using a linear (or quadratic) background subtraction to produce the SC spectra shown in Figure 3.2B. These (unnormalized) SC component spectra clearly indicate a difference in the CH stretch band intensity reflecting the different number of CH groups in each one of the fluorinated alcohols ($n_{\text{CH}} = 4$ in MFE,

$n_{\text{CH}} = 3$ in DFE, and $n_{\text{CH}} = 2$ in TFE). Additionally, as highlighted in the inset panel in Figure 3.2B, these SC spectra also display vibrational features arising from water molecules whose OH band is perturbed by the solute and thus differ from the OH band of pure water. All three fluorinated alcohols exhibit a prominent and relatively narrow OH feature with a frequency near 3660 cm^{-1} , which has previously been assigned to water dangling OH defects in the hydrogen-bonded hydration-shell structure. For all fluorinated solutes, the dangling OH feature is significantly more intense than the previously measured dangling OH in the hydration shell of EtOH (see Figure B.1). More interestingly, the intensities of the dangling OH peaks do not increase in proportion to the number of fluorine atom substitutions, suggesting that the dangling OH probability around the single fluorine atom in MFE is larger than that for each of the three fluorine atoms in TFE (as further discussed and quantified below). Moreover, the vibrational frequencies of the dangling OH peaks are significantly redshifted for MFE (3626 cm^{-1}) and DFE (3656 cm^{-1}) relative to TFE and EtOH that have dangling OH frequencies near 3670 cm^{-1} .

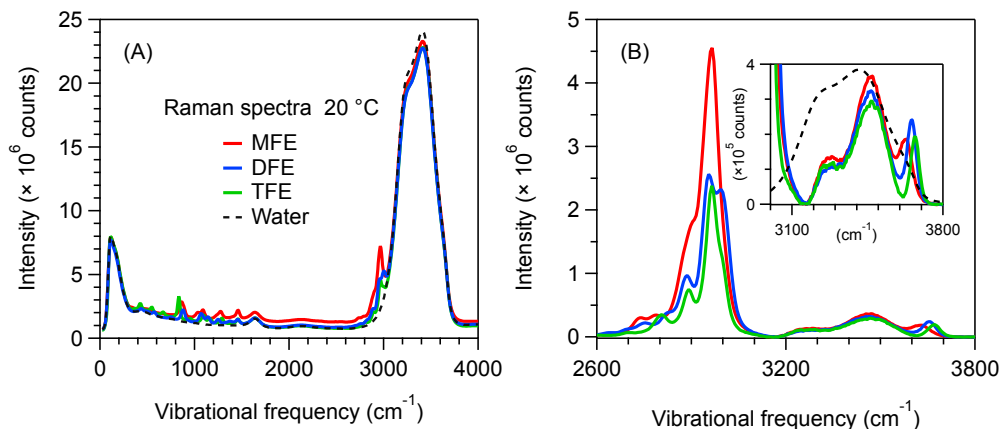


Figure 3.2. (A) Unprocessed Raman spectra obtained at $20\text{ }^{\circ}\text{C}$ for 1 mol dm^{-3} solutions of MFE, DFE, and TFE and pure water. (B) Solute-correlated component spectra of MFE, DFE, and TFE. The dashed curves are the corresponding pure water Raman spectra, arbitrarily scaled to highlight the difference in shape between the pure water and SC OH stretch bands.

Figure 3.3 shows the temperature-dependent Raman-MCR SC CH and hydration-shell OH spectra of the three fluorinated ethanol solutes along with the spectra of pure water. These results clearly reveal that the hydration shells of MFE have a significantly weaker temperature dependence than the hydration shells of DFE and TFE. Our goal is to use these spectra to obtain the corresponding thermodynamics of forming the dangling OH defect structure around all three fluorinated ethanol solutes from a hydration shell that contains no dangling OH defects.

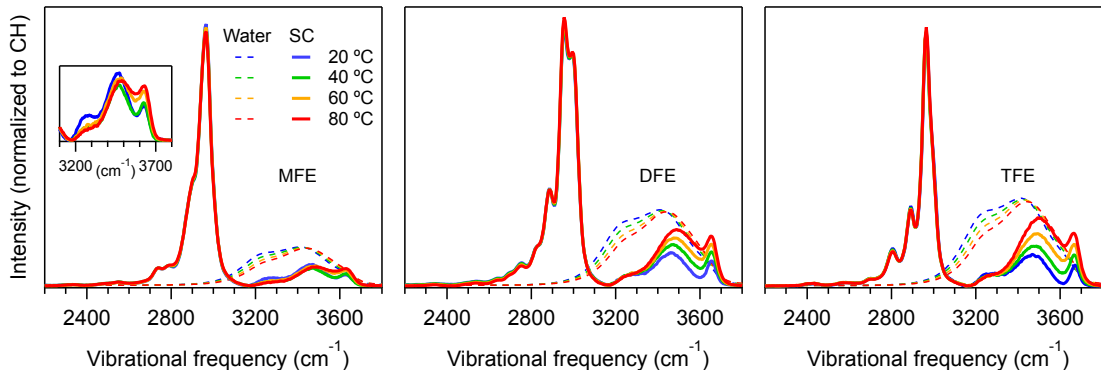


Figure 3.3. Hydration-shell spectra of MFE, DFE, and TFE normalized to the CH band area. The solid lines represent the solute-correlated (SC) spectra and the dashed lines represent the (arbitrarily scaled) spectra of pure water.

Since the intensity of the dangling OH band is proportional to the probability that such a structure will be found in the hydration shell, its temperature dependence may be used to obtain the Gibbs energy (ΔG), enthalpy (ΔH), and entropy (ΔS) of formation of these defects. However, obtaining the dangling OH band intensity requires subtracting the background intensity underlying the dangling OH band. Since the shape of the background is not precisely known, the background subtraction procedure is the most significant source of error in the resulting ΔG , ΔH and ΔS values. We have determined that the background can be reasonably well approximated by either a Gaussian or cubic polynomial function fit to the points on either side of the dangling OH band of interest. The following results pertain to the average dangling OH band intensities obtained using the two background fitting procedures,

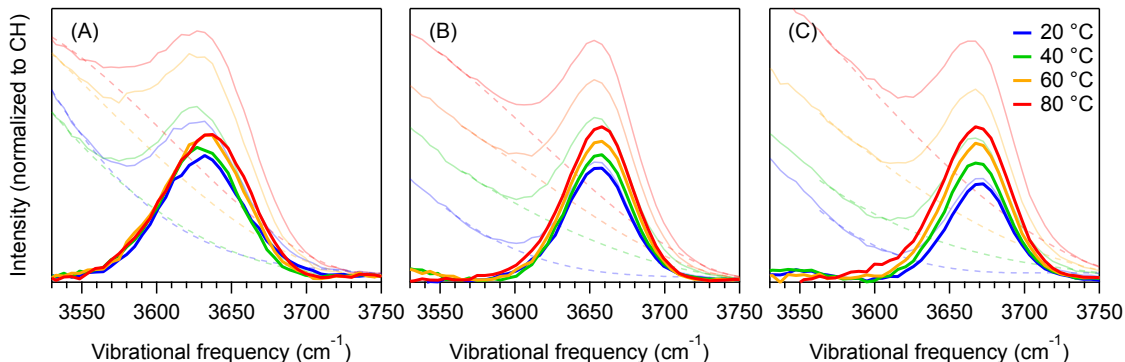


Figure 3.4. Temperature dependence of the dangling OH peaks in the hydration shell of (A) MFE, (B) DFE and (C) TFE. These peaks were obtained from the respective minimum area non-negative SC spectra (transparent solid lines), after subtracting the background (dashed lines) using a cubic polynomial function.

and the associated error bars reflect the difference between the band areas obtained in these two ways.

Figure 3.4 shows the dangling OH peaks (solid curves) obtained after subtracting the cubic background (dashed curves) from the SC hydration-shell spectra (transparent solid curves). The corresponding results obtained assuming a Gaussian background shape are shown in Figure B.3. The areas of these dangling OH peaks yield $\langle k \rangle$ through Equation 3.2, which corresponds to the average number of dangling OH defects in the solute hydration shell, as shown in Figure 3.5.

Figure 3.6 shows the ΔG , ΔH and ΔS values obtained from the experimental values of $\langle k \rangle$. As can be seen, the enthalpy of forming a dangling OH structure is invariably positive, but increases in magnitude with increasing number of fluorine atoms on the solute. This implies that the $\text{OH} \cdots \text{F}$ interaction is invariably less enthalpically favorable than a water $\text{OH} \cdots \text{O}$ hydrogen-bonded structure, but the $\text{OH} \cdots \text{F}$ interaction is more enthalpically favorable for MFE than for the other two solutes. Specifically, if we assume that the previously measured enthalpy of forming a dangling OH around EtOH ($\Delta H \approx 14 \text{ kJ mol}^{-1}$)⁵⁴ roughly corresponds to that of breaking a water–water hydrogen bond, then the above ΔH values provide the

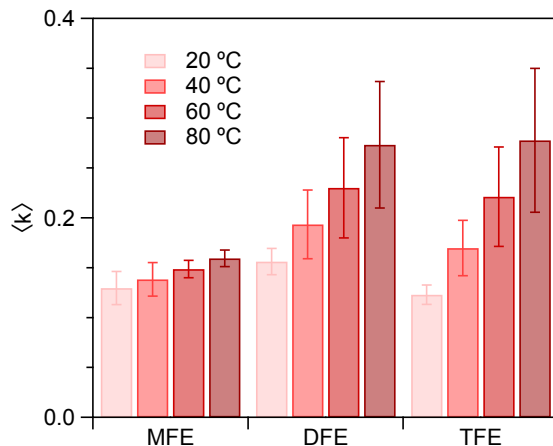


Figure 3.5. Average number, $\langle k \rangle$, of dangling OH structures per hydration shell determined experimentally using the high-frequency OH peak areas.

following estimates of the enthalpy of the $\text{OH} \cdots \text{F}$ hydrogen bond: $\Delta H_{\text{TFE}} \approx 12 - 14 = -2 \text{ kJ mol}^{-1}$, $\Delta H_{\text{DFE}} \approx 8 - 14 = -6 \text{ kJ mol}^{-1}$, and $\Delta H_{\text{MFE}} \approx 3 - 14 = -11 \text{ kJ mol}^{-1}$.

The results in Figure 3.6 further reveal that the entropy change associated with forming a dangling OH decreases with the number of fluorine atoms on the solute. Moreover, the dangling OH formation ΔS is positive for TFE and DFE but becomes negative for MFE. This implies that the dangling OH species around TFE and DFE are more flexible, while that around MFE is less flexible, relative to a water-water hydrogen-bond. Thus, both the ΔH and ΔS results imply that the single fluorine atom in MFE forms a relatively strong and rigid dangling OH structure, and thus may reasonably be described as an $\text{OH} \cdots \text{F}$ hydrogen bond, while adding more fluorine atoms to the terminal methyl group of ethanol weakens the associated $\text{OH} \cdots \text{F}$ structures and increases their flexibility.

Simulation results. Molecular dynamics (MD) simulations were used to determine the temperature dependence of the formation of non-water-bonded hydroxy structures in the hydration shell of the solutes. As mentioned above (Figure 3.1), this population actually comprises two subpopulations: hydroxy groups pointing to the tail of the solute (called hydrogen bond-like structures) and free hydroxy groups. In Figure 3.7(A), we quantify the non-water-bonded hydroxy structure population; the hydrogen bond-like subpopulation is

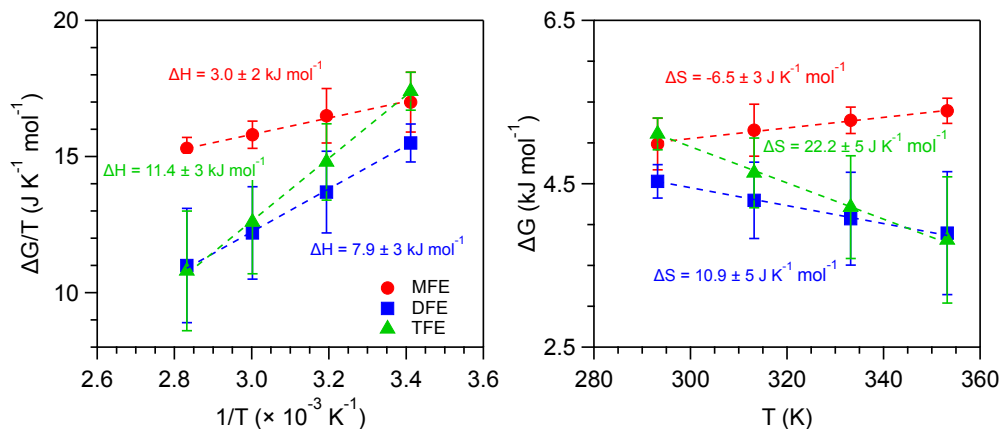


Figure 3.6. Enthalpy and entropy changes associated with the formation of dangling OH structures with increasing fluorination of the methyl group of ethanol using the experimental average $\langle k \rangle$ values.

shown in panel (B) of the same figure. Comparing these results with experiment (Figure 3.5) clarifies that the population, in the MD simulations, that best represents the spectroscopically active population giving rise to the dangling OH peak from experiment is that of non-water-bonded hydroxy groups, that is, both free hydroxy groups and hydrogen bond-like hydroxy groups pointing towards the solute. This conclusion is further supported by comparing the thermodynamics of formation of non-water-bonded hydroxy structures obtained with simulation (Figure 3.8) and experiment (Figure 3.6). Even though the absolute values of the enthalpy and entropy of formation differ between experiment and simulation, the observed trends are equivalent. More specifically, the enthalpy required to break a water-water hydrogen bond in the hydration shell of the solute to form either a free hydroxy or a hydrogen-bond-like structure becomes increasingly more unfavorable with increasing fluorine content. Conversely, the entropy change for the same process becomes increasingly more favorable with increasing degree of fluorination and shows a change in sign from MFE to DFE. This change in sign is of particular interest, since it implies that a non-water-bonded structure near a monofluoromethyl group has less conformational freedom than a water–water hydrogen bond in the same region, whereas structures near DFE and TFE are less conformationally restricted.

Direct solute–water interactions can be quantified using symmetry-adapted perturbation theory. The results of these calculations are shown in Figure 3.9A for several water–solute

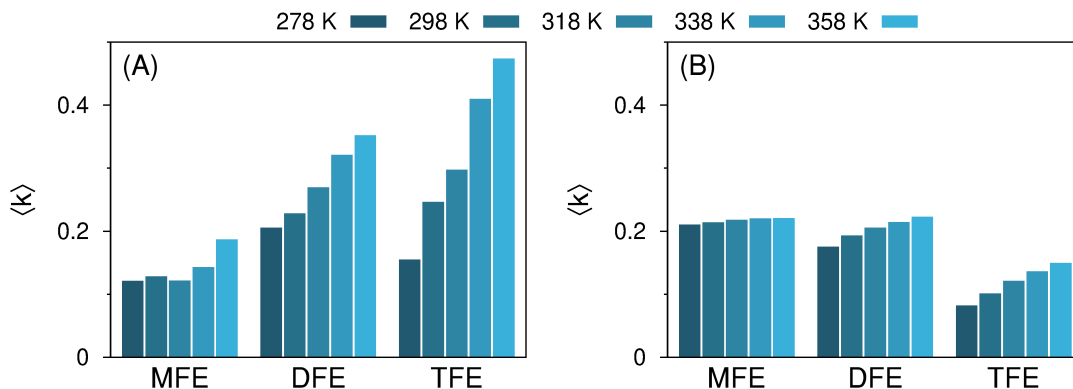


Figure 3.7. Average number $\langle k \rangle$ of non-water-bonded (panel A) and hydrogen bond-like (panel B) hydroxy structures *per* hydration shell, quantified with MD simulations in the $278 \leq T/K \leq 358$ range, for solutions of MFE, DFE and TFE.

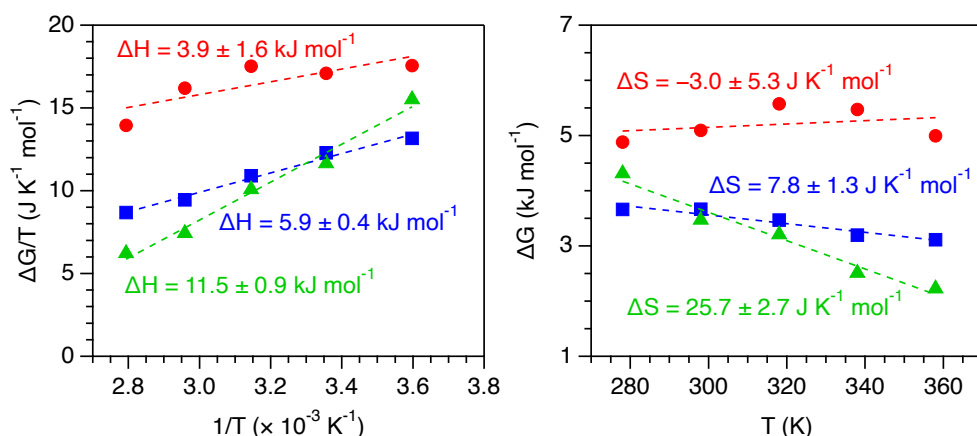


Figure 3.8. Free energy of formation of a non-water-bonded hydroxy structures (MFE as red circles, DFE as blue squares, TFE as green triangles) in the $278 \leq T/K \leq 358$ range, calculated from MD simulations. Dashed lines are linear fits to the data points from where the enthalpy (panel A), the entropy (panel B) and their respective errors are calculated.

dimer configurations in vacuum. These configurations were extracted from MD simulations of the solute in a water box, and are therefore representative of a fully hydrated solute. The variation of the total interaction energy between a solute and a single water molecule along the distance between the water oxygen atom and the solute's closest fluorine atom is distinct between MFE, DFE or TFE only when the water molecule forms a hydrogen bond-like

structure with the solute. For these configurations, the interaction becomes less favorable with increasing number of fluorine atoms (Figure 3.9A). The observed trend in stability is in agreement with the enthalpies of formation of hydrogen bond-like structures in Figures 3.6 and 3.8.

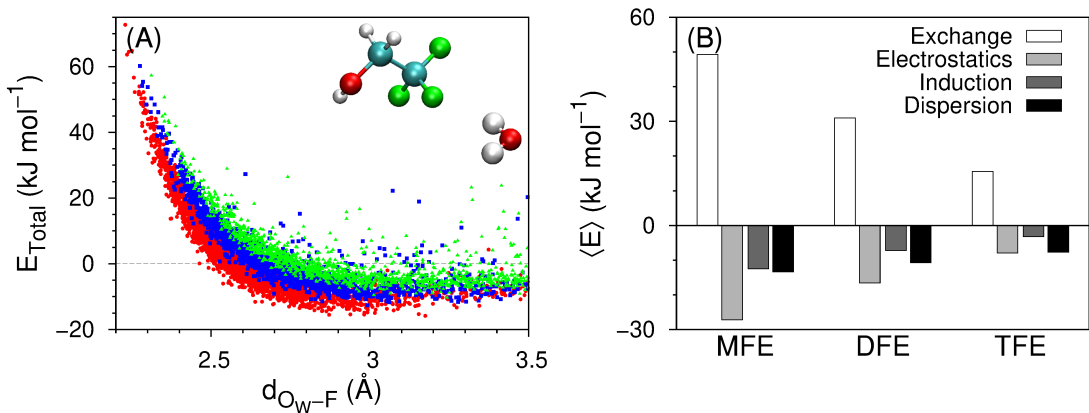


Figure 3.9. A) Total interaction energy *vs.* distance for water–solute dimers forming a hydrogen bond-like structure (water-MFE as red circles, water-DFE as blue squares, water-TFE as green triangles), calculated at the DF-SAPT2+(CCD) δ MP2/aug-cc-pVTZ level of theory. The distance corresponds to the closest water oxygen-fluorine pair. Configurations are extracted from MD simulations at 298 K. The inset molecules represent a conformation of a water–TFE dimer corresponding to one of the plotted data points. B) Average energy components $\langle E \rangle$, calculated for distances above which the total energy becomes attractive (2.5, 2.6 and 2.8 \AA for MFE, DFE and TFE, respectively). The number of points in each data set is MFE: 2890; DFE: 1537; TFE: 1314.

Additionally, SAPT calculations allow us to decompose the total interaction energy into electrostatics, London dispersion, induction and exchange contributions, which are shown as averages in Figure 3.9B. All contributions decrease in magnitude with increasing degree of fluorination. However, the ratio of different attractive contributions indicates that, while electrostatics is always twice as large as induction, the dispersion:induction ratio increases from one to two along the transition from MFE to TFE and the dispersion:electrostatics ratio increases from one-half to one.

3.5 Conclusions

We have investigated the sequential fluorination of a methyl group (in ethanol) and the associated changes in hydrophobicity, hydration shell structure and thermodynamics. The hydrophobicity of a methyl group scales non-monotonically with the degree of fluorination, as the hydrophobicity of a methyl group initially decreases and then increases with the addition of 1 to 3 fluorine atoms. We have shown that a specific hydration shell structure, $\text{CF}\cdots\text{HOH}$, meeting geometric criteria commonly used to define water–solute hydrogen bonds, is present in aqueous solutions of each of these alcohols. Furthermore, the free energy, enthalpy and entropy of formation of this structure, which are experimentally accessible using spectroscopic methods, are sufficiently different as to allow for a categorization of the structures into either hydrogen bond (MFE) or dangling hydroxy (TFE), or a structure exhibiting intermediate spectroscopic and thermodynamics features (DFE). Moreover, both enthalpy and entropy are indispensable for our understanding of hydrogen bonds. The hydrogen bond donated by water to the fluorine in MFE actually has comparable enthalpy to that of water–water hydrogen bonds; the former is overall much weaker than the latter only because of its high entropic cost. Finally, the balance of attractive solute–water interactions, namely London dispersion and electrostatics, closely follows the categorization: hydrogen bonds are highly directional owing to a large electrostatic stabilization from the aligned dipoles of the C–F and the H–O bonds; loosely bonded dangling hydroxys have a much weaker stabilizing contribution of electrostatics, which is near-exactly matched by London dispersion. Our results demonstrate that the combined use of Raman-MCR and theoretical calculations may be used to quantify and mechanistically explain subtle changes in hydrogen bond character and local hydrophobicity associated with sequential fluorination of a methyl group, and suggest that the same strategy could be extended to other solute–solvent interactions.

The effects of mono-, di-, and trifluorination on solute–water interactions reported here and, more generally, the importance of understanding the entropic and enthalpic signature of solute–water hydrogen bonds (relative to water–water hydrogen bonds in the bulk liquid) have potentially important implications for drug design and for our understanding of biological systems. This importance is illustrated by the surprising capability of fluorinated BPTI

derivatives to inhibit β -trypsin. The (β -trypsin) BPTI binding pocket contains up to five water molecules, which interact with nearby amino acids and play a role in the binding affinity. Wild-type BPTI has an arginine amino acid in the binding loop. Replacing arginine by ethylglycine dramatically reduces inhibitory capacity of BPTI — unsurprisingly, given that the long, positively charged side chain of arginine was replaced by a short and electrostatically neutral one (CH_2CH_3). Replacing the methyl group in ethylglycine by di- or trifluorinated variants, however, recovers inhibitory capacity of BPTI to wild-type levels.⁴⁰ Our results point towards a mechanistic explanation of these changes.

Predicting whether two molecules interact mainly through electrostatics or dispersion is a long-standing challenge that typically requires a combination of methods with limited application to condensed phase systems.^{69–71} Here, we have demonstrated that hydration shell spectroscopy accompanied by simulation can be used to elucidate such interactions. Increasing enthalpic cost and entropic gain of forming hydrogen bond-like structures *does* correlate with a decrease in the electrostatics:dispersion ratio for ethanol, MFE, DFE and TFE. Thus, it is possible to link electrostatic and dispersive contributions to the formation of different solute–water hydrogen bond-like structures and their influence on hydration thermodynamics.

4. SPECIFIC ION EFFECTS ON NON-IONIC MICELLE FORMATION

A version of this chapter was published in a peer-reviewed journal as:

Mendes de Oliveira, D.; Ben-Amotz, D. Spectroscopically quantifying the influence of salts on nonionic surfactant chemical potentials and micelle formation. *J. Phys. Chem. Lett.* **2021**, *12*, 355–360.

Abstract. The influence of two salts (NaSCN and Na₂SO₄) on the micellization of a non-ionic surfactant (1,2-hexanediol) is quantified using Raman multivariate curve resolution (Raman-MCR) spectroscopy, combined with a generalized theoretical analysis of the corresponding chemical potential changes. Although SCN[−] and SO₄^{2−} are on opposite ends of the Hofmeister series, they are both found to lower the critical micelle concentration. Our combined spectroscopic and theoretical analysis traces these observations to the fact that in both salt solutions the ions have a greater affinity for (or are less strongly expelled from) the hydration shell of the micelle than the free surfactant monomer, as quantified using the corresponding chemical potentials and Wyman-Tanford coefficients. This probe-free experimental and theoretical analysis strategy may readily be extended to micelle formation processes involving other surfactants, salts, and co-solvents, as well as to other sorts of aggregation and binding processes.

4.1 Introduction

Interactions between ions and aqueous molecular interfaces are important for numerous chemical and biological processes, including the solubility of nonelectrolytes,⁷² enzyme catalysis,^{73,74} molecular self-assembly,^{75–77} membrane permeability^{78,79} and cellular exocytosis.⁸⁰ Although the associated ion-specific (Hofmeister) effects^{81–83} are in principle traceable to the influence of salts on the corresponding chemical potentials, open questions remain regarding the corresponding ion-molecule interactions.^{83–86} Here we obtain such information by spectroscopically and theoretically analyzing the influence of two salts (NaSCN and Na₂SO₄) on the critical aggregation (micelle) concentration, C_A , of the non-ionic surfac-

tant 1,2-hexanediol (12HD). We do so by combining Raman multivariate curve resolution (Raman-MCR)^{2,3,8,31,87–90} measurements with a Wyman-Tanford^{88,91–93} theoretical analysis. The results provide a means of spectroscopically quantifying C_A as well as the differential partitioning of the two salts into the hydration shells of the free surfactant monomer and micelle, and the associated chemical potential changes. Our results reveal that the stabilization of the micelle by both salts is linked to the higher ion concentration in the hydration shell of the micelle than the free 12HD monomer. Thus, the stabilization of the non-ionic micelles by both these salts has much in common with the mechanisms by which polymer collapse and protein folding are enhanced by some salts and osmolytes.^{94,95}

Although some prior experimental and theoretical studies have described the influence of salts on the critical micelle concentration of 12HD and other non-ionic surfactants,^{96–98} none of these studies have characterized the effect of salts on the hydration shells of the monomeric and aggregated species, or quantitatively related the corresponding observations to the chemical potentials of both the free monomers and aggregates. The application of Raman-MCR to the elucidation of ionic micelle structures has previously been described,⁸⁷ but did not extend to non-ionic surfactants or the influence of salts on micelle formation. Prior theoretical treatments of micelle salt-effects have focused primarily on changes in the solubility of the free surfactant monomers, effectively treating the micelle as a reference state whose free energy is not significantly influenced by salts.^{96–98} Moreover, these prior theoretical analyses have not attempted to relate the influence of salts on micelle formation to Wyman-Tanford theory.^{88,91–93}

Raman-MCR is ideally suited to the quantitative analysis of surfactant solutions consisting of an equilibrium between free monomers and micelles,^{99,100} since each of these species have distinct hydration-shell spectra (and surfactant spectral shifts). The self modeling curve resolution (SMCR)^{5,31} strategy begins with a first round of SCMR that removes bulk solvent contributions from each surfactant solution spectrum, to yield the corresponding surfactant-correlated spectrum. A second round of SMCR is then used to decompose the first round surfactant-correlated spectra into a linear combination of free monomer and micelle components, and thus to quantify the micelle formation equilibrium and its salt dependence.

Wyman-Tanford theory^{88,91-93} can provide additional insight regarding the mechanism responsible for salt-induced changes in the critical micelle concentration. More specifically, this theory links the influence of salts on the micelle formation equilibrium ($n M \rightleftharpoons M_n$) to the partitioning of ions (and water) into the hydration shells of the micelle (M_n) and free monomer (M), as determined by the following partition coefficient.

$$\Gamma = \left\langle n_W \left(\frac{n_S}{n_W} - \frac{N_S - n_S}{N_W - n_W} \right) \right\rangle \quad (4.1)$$

The variables N_i are the total numbers of molecules of type i in the system (where $i = S$ for salt and $i = W$ for water), whose values are determined by the total concentration of the solution. The variables n_i are the corresponding numbers of molecules in the surfactant hydration shell. Note that Γ will be equal to zero if the local salt-to-water ratio in the surfactant hydration shell, n_S/n_W , is equal to that far from the surfactant, $(N_S - n_S)/(N_W - n_W)$, and Γ will be positive if salt ions accumulate around the surfactant or negative if salt ions are expelled from the surfactant hydration shell.

Wyman-Tanford theory⁸⁸ yields the following expression for the influence of a salt of concentration C_S on the micelle formation equilibrium constant, $K_n = [M_n]/[M]^n$.

$$\frac{d \ln K_n}{d \ln C_S} = C_S \left(\frac{d \ln K_n}{d C_S} \right) = \Delta \Gamma = \Gamma_A - \Gamma_F \quad (4.2)$$

Note that Γ_A pertains to partitioning of salt (and water) to the hydration shell of the entire aggregate (micelle) containing n monomers, and Γ_F pertains to the hydration shells of a collection of n free monomers.

The partition coefficient difference $\Delta \Gamma$ may be determined from the experimentally measured salt-induced change in the critical micelle concentration, $\Delta C_A = C_A^S - C_A$, where C_A and C_A^S represent the critical micelle concentrations in pure water and the salt solution, respectively. Moreover, $\Delta \Gamma$ may be quantitatively linked to the derivative of the surfactant chemical potential with respect to salt concentration, k_i (where $i = 1$ for the free monomer and

$i = n$ for the micelle). More specifically, the relationship between $\Delta\Gamma$, ΔC_A and $\Delta k = k_n - k_1$ is given by Eq. 4.3 (whose detailed derivation is provided in Appendix C.2).

$$\Delta\Gamma = -n \left(\frac{\Delta C_A}{C_A} \right) = -n \left(\frac{\Delta k C_S}{RT} \right) \quad (4.3)$$

Thus, a salt-induced decrease of the critical micelle concentration (i.e., $\Delta C_A < 0$, as observed experimentally) implies that $\Gamma_A > \Gamma_F$ and $k_1 > k_n$, independent of the signs of Γ_A , Γ_F , k_1 and k_n . In other words, if salt ions are expelled from the hydration shells of both the free monomer and micelle, then Eq. 4.3 implies that salt invariably increases the surfactant chemical potential, but more so for the free monomer than the micelle. Conversely, if the salt concentration is enhanced in the hydration shells of both the free monomer and micelle, then Eq. 4.3 implies that salt decreases the surfactant chemical potential, but less so for the micelle than the free monomer.

Here we used a probe-free Raman-MCR spectral decomposition strategy to determine both C_A and ΔC_A for 12HD in pure water and aqueous salt solutions. We thus demonstrate that Raman-MCR provides a direct means of experimentally determining both $\Delta\Gamma$ and Δk , using the previously reported light scattering measurement of the average micelle size of $n \approx 20$ for 12HD in pure water.¹⁰¹ Moreover, the previously reported critical micelle concentration of 12HD in pure water $0.53 \text{ M} \leq C_A \leq 0.75 \text{ M}$, obtained using various methods,^{96,101} is consistent with the value of $C_A = 0.60 \pm 0.02 \text{ M}$ that we have obtained using Raman-MCR.

4.2 Experimental Methods

Aqueous solutions of 12HD (1,2-hexanediol, Sigma-Aldrich, 98%), NaSCN (sodium thiocyanate, Sigma-Aldrich, $\geq 98\%$), and Na_2SO_4 (sodium sulfate, Sigma-Aldrich, $\geq 99\%$) were prepared with ultrapure filtered water (Milli-Q UF Plus, Millipore, $18.2 \text{ M}\Omega \text{ cm}$). Raman spectra were obtained at 20°C using an Ar-ion 514.5 nm laser with $\sim 20 \text{ mW}$ of power at the sample and 5 min of integration time. Backscattered Raman photons were collected from the sample using a $20\times$ long-working-distance microscope objective ($\text{NA} = 0.42$, Mitutoyo Inc.) and transmitted with an optical fiber to an imaging spectrograph (SpectraPro300i, Acton

Research Inc.) that was equipped with a 300 grooves/mm grating and a thermoelectrically cooled CCD camera (Princeton Instruments Inc.).

Self-modeling curve resolution (SMCR) was performed with pairs of solvent and solution spectra to obtain Raman-MCR solute-correlated (SC) spectra.^{2,5,31,90} In these spectral decompositions, the solvent spectrum was constrained to either being pure water or the corresponding salt solution. Thus, the SC spectra include vibrational bands arising from 12HD as well as features arising from solvent molecules whose vibrational spectra are perturbed by 12HD. When the solvent is a salt solution, the SC spectra may include features arising from 12HD-induced perturbation of the vibrational spectra of both the water and the salt molecular anions (SCN^- or SO_4^{2-}).

Monomer and aggregate concentrations of 12HD were estimated using total least squares (TLS) regression.^{102,103} In this procedure, the SC spectrum of a given 12HD solution is decomposed into a linear combination of free and aggregated components, obtained as follows: (i) the monomer spectrum is the SC spectrum of a sufficiently dilute solution of 12HD so that no aggregation has taken place; and (ii) the aggregate spectrum is obtained from a second round SMCR analysis performed on the first round SC spectra obtained at different 12HD concentrations.

The critical micelle concentration (C_A) was obtained from a plot of the resulting (TLS derived) monomer and aggregate concentrations as a function of the total surfactant concentration $[\text{12HD}]_T$. The C_A value was identified as the x -axis intercept of a linear fit to the concentration of aggregated 12HD as a function $[\text{12HD}]_T$, performed over a concentration range from 0.7 M to 2 M, which is well above C_A .

4.3 Results and Discussion

Figure 4.1A shows the measured Raman spectra of 12HD solutions at various concentrations. The corresponding Raman-MCR surfactant-correlated (SC) spectra, shown in Figure 4.1B, highlight differences between the solution and pure water spectra, revealing the following two changes with increasing 12HD concentration: (1) a decrease in the average CH frequency and (2) a decrease in the area of the hydration-shell OH stretch band.

The concentration dependence of the mean CH frequency shift, plotted in Figure 4.1C, has a sigmoidal shape characteristic of micelle formation, as the CH frequency of fully hydrated free monomers ($\omega_{\text{CH}} \sim 2907 \text{ cm}^{-1}$) decreases towards that in the substantially dehydrated micelles ($\omega_{\text{CH}} \sim 2902 \text{ cm}^{-1}$). The critical aggregation concentration C_A roughly corresponds to the concentration at which the CH frequency becomes markedly non-linearly concentration dependent. A more precise identification of C_A may be obtained from the x -axis intercept of the dashed line in Figure 4.1D, as further described below.

Since all the SC spectra in Figure 4.1B are normalized to the 12HD CH band area, the observed decrease of the SC OH stretch band with increasing 12HD concentration is consistent with the aggregation-induced dehydration of 12HD, as previously observed in the aggregation of various monoalcohols in water,^{104–106} as well as in the formation of micelles from ionic surfactants.⁸⁷ For dilute solutions ($[12\text{HD}]_{\text{T}} < 0.5 \text{ M}$), there is only a small change in intensity of the hydration shell OH band, indicating that small aggregates do not significantly expel water molecules from the 12HD hydration shell, and thus the dehydration that is evident in Figure 4.1B is due primarily to micelle formation.

The family of OH stretch bands in Figure 4.1B arise from water molecules that are perturbed by 12HD and thus have a spectral shape different from that of the OH stretch band of pure water, as indicated by the dashed blue curve in the inset panel in Figure 4.1B. Note that there are over 100 water OH groups in the first hydration shell of 12HD, so the two OH groups of 12HD do not significantly contribute to the SC spectra shown in Figure 4.1B, as further confirmed by the fact that the SC hydration shell OH band spectrum of dilute aqueous 12HD is essentially identical to that of 1-hexanol.³

The SC spectra in Figure 4.1B may be quantitatively decomposed into a linear combination of free and aggregated component spectra, using a second round SMCR analysis performed on all the SC spectra (over a frequency range of 2375 cm^{-1} to 3770 cm^{-1}). More specifically, the low concentration SC spectrum is assigned to the free monomer and the new second round SMCR component, indicated by the dotted-black curve in Figure 4.1B, is assigned to the 12HD molecules that are in a micelle. The robustness of this spectral decomposition is confirmed by noting that virtually identical aggregate spectra are obtained when using different high-concentration SC spectra as input for the second round SMCR decomposition.

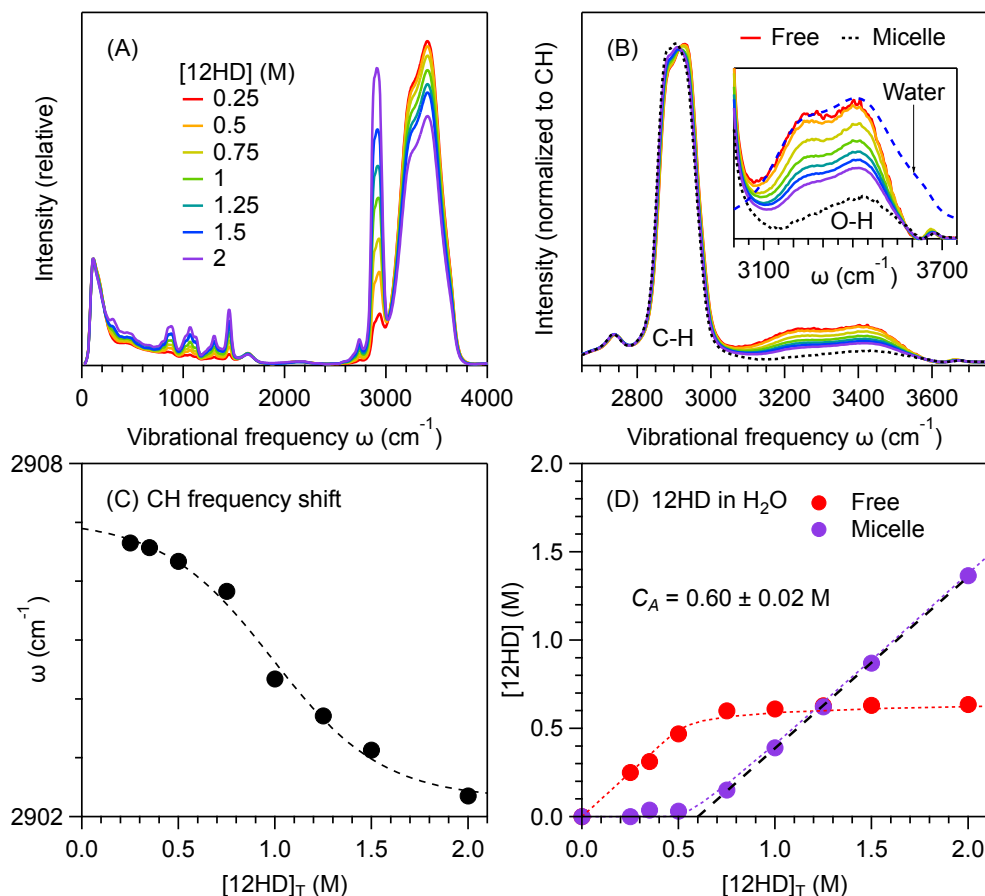


Figure 4.1. Experimental Raman spectra and Raman-MCR results pertaining to 12HD dissolved in pure water. (A) Measured Raman spectra of aqueous 12HD at 20 °C at various concentrations. (B) SC spectra of 12HD in the CH and OH stretch band region, after subtraction of a cubic polynomial background. The inset figure in (B) shows an expanded view of the SC hydration shell OH stretch band region, including the OH bands of pure water (dashed blue curve) and the micelle hydration shell (dotted-black curve). (C) The mean CH frequency of 12HD is plotted as a function of [12HD]_T. (D) The concentrations of free and aggregated 12HD plotted as a function of [12HD]_T, obtained from a TLS fit of the SC spectra in (A) to a linear combination of the free (solid red curve) and aggregated (dotted-black curve) spectra.

To determine the corresponding free and aggregated 12HD concentrations, we performed a total least squares (TLS) regression fit of all the SC spectra to a linear combination of the free monomer SC spectrum (obtained at [12HD]_T = 0.25 M) and micelle spectrum (dotted-black curve in Figure 4.1B). The results of this decomposition are indicated by the points in

Figure 4.1D. As can be seen, virtually no aggregation has taken place in dilute solutions of 12HD, but, as the 12HD concentration is increased above ~ 0.5 M, an abrupt change occurs, characterizing the formation of higher-order aggregates when $[12\text{HD}]_{\text{T}} > C_A$. More specifically, we identify C_A as the x -axis intercept of a linear fit (dashed line) to the points corresponding to the concentration of aggregated 12HD molecules, performed over a concentration range of $0.7 \text{ M} \leq [12\text{HD}]_{\text{T}} \leq 2 \text{ M}$, to obtain $C_A = 0.60 \pm 0.02 \text{ M}$ for 12HD in pure water, in good agreement with previous estimates.^{96,101} Further validation of our assignments of the component spectra is provided by the good agreement between the experimental points in Figure 4.1D and the dotted curves obtained assuming a micelle formation equilibrium with $n = 20$ and $C_A = 0.60 \text{ M}$ (obtained as described in Appendix C.2).

To quantify the influence of salts on the 12HD micelle formation, we performed Raman-MCR measurements on ternary mixtures containing 12HD, water, and either 2 M NaSCN or 0.25 M Na₂SO₄, as at these concentrations the two salts produced a similar influence on the 12HD micelle formation. The salt concentration was held constant while the 12HD concentration was varied, such that the aqueous salt solution was treated as the solvent and 12HD as the solute in the subsequent SMCR decompositions (which were otherwise performed as described above).

Figure 4.2 shows the concentrations of 12HD in the free monomer and micelle states in (A) 2 M NaSCN and (B) 0.25 M Na₂SO₄. These concentrations were obtained in the same way as those in Figure 4.1D, using the free monomer and micelle component spectra pertaining to the corresponding salt solution (shown in Appendix C.1). The resulting critical aggregation concentrations C_A^S and dotted curves in Figure 4.2 were also obtained in the same way as those in Figure 4.1D. Comparison of these C_A^S values with the C_A in pure water (see Figure 4.1D) reveals that the critical micelle concentrations in the salt solutions are both lower than that in pure water, thus indicating that both salts stabilize the micelle with respect to the free monomer.

More quantitative information regarding the influence of the salts on 12HD micelle formation may be obtained by using the measured $\Delta C_A = C_A^S - C_A$ to determine both Δk and $\Delta \Gamma$ (using Eq. 4.3), and thus quantify the differential affinities of the ions for the free and aggregated 12HD molecules, as well as the corresponding chemical potential changes. The salt-

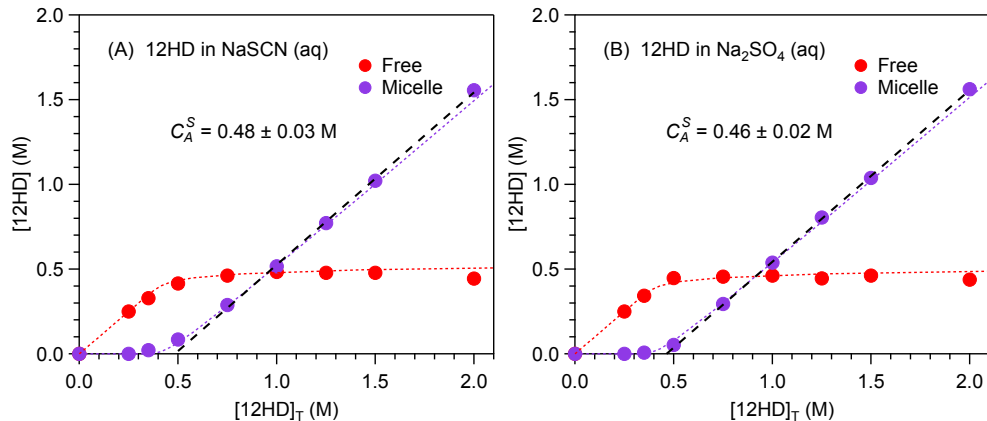


Figure 4.2. Raman-MCR results pertaining to 12HD dissolved in aqueous salt solutions containing either 2 M NaSCN or 0.25 M Na₂SO₄. (A) Free and aggregated 12HD concentrations in 2 M NaSCN. (B) Free and aggregated 12HD concentrations in 0.25 M Na₂SO₄.

induced decrease in the critical micelle concentration implies that $\Delta C_A/C_A = -0.20 \pm 0.01$ in 2 M NaSCN, and $\Delta C_A/C_A = -0.23 \pm 0.01$ in 0.25 M Na₂SO₄. Given that there are approximately $n = 20$ molecules of 12HD in each micelle,¹⁰¹ Eq. 4.3 implies that $\Delta\Gamma \approx 4.0$ in the aqueous NaSCN, and $\Delta\Gamma \approx 4.6$ in aqueous Na₂SO₄. Moreover, Eq. 4.3 further indicates that $\Delta k \approx -0.24$ (kJ/mol M⁻¹) and $\Delta k \approx -2.2$ (kJ/mol M⁻¹) in aqueous NaSCN and Na₂SO₄, respectively, in keeping with the fact that a nearly ten times higher NaSCN concentration is required to produce a similar decrease in C_A .

Although the values of $\Delta\Gamma$ and Δk are directly measurable, as described above, determining the signs and magnitudes of Γ_A , Γ_F , k_n , and k_1 requires additional information. Raman-MCR provides some of such information as it indicates that SCN⁻ anions penetrate significantly into the hydration shell of 12HD, while SO₄²⁻ anions do not. The interaction between 12HD and SCN⁻ is evidenced not only by the NaSCN-induced changes in the hydration shell spectra of both the free 12HD monomer and micelle (see Appendix Figure C.1) but also by changes in the C≡N band of SCN⁻ induced by its interactions with both the free monomer and micelle (see Appendix Figures C.2 and C.3). On the other hand, no such interactions are seen in 0.25 M Na₂SO₄ (Appendix Figures C.1 and C.4). These observations imply that the values of

both k_1 and k_n are positive for 12HD in 0.25 M Na_2SO_4 , while in 2 M NaSCN both k_1 and k_n have smaller magnitudes, and may perhaps be negative.

Additional constraints on the range of physically reasonable values of k_1 and k_n may be obtained by considering the consequences of assuming either that the salt has no effect on the chemical potential of the micelle or assuming that the local salt concentration in the hydration shell of 12HD is the same for the free monomer and micelle (as further explained in the SI, Section 4). Such considerations lead to the conclusion that $2.2 \leq k_1 \leq 5.9$ (kJ/mol M^{-1}) in 0.25 M Na_2SO_4 , while in 2 M NaSCN k_1 is approximately ten times smaller and k_n is smaller still, and may perhaps be negative. The corresponding range of Wyman-Tanford partition coefficient estimates are $-12 < \Gamma_F \leq -5$ in 0.25 M Na_2SO_4 and $-6 \leq \Gamma_F \leq -4$ in 2 M NaSCN (as further explained in Appendix C.3), and thus Γ_A in aqueous NaSCN must be near zero, and may perhaps be positive.

4.4 Conclusions

In summary, we used a new probe-free Raman-MCR based spectral decomposition strategy to determine the critical micelle concentration of a non-ionic surfactant 12HD in pure water and aqueous NaSCN and Na_2SO_4 . The resulting surfactant-correlated spectra revealed that SCN^- anions penetrate significantly into the hydration shell of 12HD, while SO_4^{2-} anions do not. A Wyman-Tanford theoretical analysis strategy was used to quantify the partitioning of these ions into the surfactant hydration shell and the resulting salt-induced chemical potential changes. Our results explain how it is that these ions on opposite ends of the Hofmeister series produce a similar reduction in the critical micelle concentration, as the ion-induced stabilization of the micelles is due to the greater ion affinity for (or weaker expulsion from) the hydration shell of the micelle than the free surfactant monomer. The Raman-MCR and Wyman-Tanford strategy is quite general and thus could be extended to other micelle formation, binding, and folding processes.

5. DIRECT-CONTACT ION PAIRING IN AQUEOUS ACETATE SOLUTIONS

A version of this chapter was published in a peer-reviewed journal as:

Mendes de Oliveira, D.; Zukowski, S. R.; Palivec, V.; Hénin, J.; Seara, H. M.; Ben-Amotz, D.; Jungwirth, P.; Duboué-Dijon, E. Binding of divalent cations to acetate: Molecular simulations guided by Raman spectroscopy. *Phys. Chem. Chem. Phys.* **2020**, 22, 24014–24027.

Abstract. In spite of the biological importance of the binding of Zn^{2+} , Ca^{2+} , and Mg^{2+} to the carboxylate group, cation-acetate binding affinities and binding modes remain actively debated. Here, we report the first use of Raman multivariate curve resolution (Raman-MCR) vibrational spectroscopy to obtain self-consistent free and bound metal acetate spectra and one-to-one binding constants, without the need to invoke any *a priori* assumptions regarding the shapes of the corresponding vibrational bands. The experimental results, combined with *ab initio* simulations, indicate that the measured binding constants pertain to direct (as opposed to water separated) ion pairing. The resulting binding constants do not scale with cation size, as the binding constant to Zn^{2+} is significantly larger than that to either Mg^{2+} or Ca^{2+} , although Zn^{2+} and Mg^{2+} have similar radii and are about 25% smaller than Ca^{2+} . Remaining uncertainties in the metal acetate binding free energies are linked to fundamental ambiguities associated with identifying the range of structures pertaining to non-covalently bound species.

5.1 Introduction

Divalent non-transition metal cations, in particular calcium (Ca^{2+}), magnesium (Mg^{2+}), and zinc (Zn^{2+}), play important roles in many biological processes and diseases.^{107–116} Calcium is one of the key signaling species triggering changes in conformations of proteins involved, among others, in interactions between neurons, contraction of muscle cells, or exocytosis.^{107,108} Magnesium is vital, for example, for enzymatic catalysis including ATP synthesis and for stabilizing nucleic acids.^{109–111} Similarly, zinc is essential for proper function of many enzymes involved, e.g., in cell growth and reproduction, as well as for DNA stability

and gene expression.^{112,113} The biological functions of these ions are realized by specialized ion-binding structures of the relevant biomolecules, such as the calcium-binding EF-hand motif¹¹⁴ and the zinc finger¹¹⁵ in proteins or phosphate-containing nucleic acid backbone motifs for binding of magnesium.¹¹⁶ Carboxylate of the side chain of glutamate or aspartate, or monovalent phosphate of the DNA/RNA backbone of phosphorylated biomolecules are examples of biologically relevant negatively charged groups that interact with divalent cations. Here, we focus on the former group with the aim to elucidate the structural and energetic details of the interaction between an acetate anion—previously shown to be a good proxy for ion pairing of biologically relevant carboxylate groups¹¹⁷—with $\text{Ca}^{2+}/\text{Mg}^{2+}/\text{Zn}^{2+}$ in an aqueous environment. Note that we aim to model here an isolated carboxylate group rather than any specific strong binding site made of multiple carboxylates.

Prior metal carboxylate binding constant compilations¹¹⁸ and individual studies include experimental potentiometric,^{119–123} NMR,¹²⁴ vibrational spectroscopic,^{125–127} and surface sum frequency^{128,129} measurements, as well as theoretical classical¹³⁰ and quantum¹³¹ calculations. In the case of acetate (Ac^-), the range of previously reported binding constants consistently point to weak pairing with divalent cations.^{118,120} However, previous works are not always in agreement regarding the relative binding strengths of these three cations (although studies that have included all three cations generally agree that Zn^{2+} binds more strongly to Ac^- than either Mg^{2+} or Ca^{2+}).^{118,119} In addition, molecular interpretation of such binding constants remains elusive, since it is often unclear to what kind of ion pairs the experiments are particularly sensitive. On the molecular modeling side, the description of the interactions of dications with their anionic binding partners can only be as trustworthy as the underlying force field. It is, therefore, crucial to properly benchmark the interaction parameters against experimental data.^{132,133}

Most prior experimental studies of metal acetate binding constants have utilized potentiometric measurements. Although such measurements have provided a vast data base of binding constant results,¹¹⁸ they are inherently ambiguous with regard to the structures of the bound species, and are susceptible to systematic errors associated with interfacial electrode effects.^{120,134} Vibrational spectroscopic methods offer an appealing alternative detection strategy, as the associated spectral changes contain molecularly detailed information

pertaining to both the free and bound species (and their hydration shells). However, prior attempts to use vibrational infrared and Raman spectroscopy to determine metal acetate binding constants were restricted to the use of Gaussian-Lorentzian fits to the acetate CC stretch band (near 940 cm^{-1})^{126,127} and did not report consistent binding constant results for Zn^{2+} , Mg^{2+} , and Ca^{2+} . These prior studies also concluded that the carboxylate COO^- stretch band (near 1400 cm^{-1}) was less quantitatively useful, presumably because of its overlap with to a CH_3 deformation mode, although the apparent splitting between the symmetric and antisymmetric carboxylate stretch sub-bands has been interpreted as providing some information regarding the presence of unbound (free acetate), monodentate, bidentate, and bridging complexes.^{125–127}

In an effort to resolve these discrepancies, we have used a new Raman multivariate curve resolution (Raman-MCR) measurement strategy to obtain self-consistent one-to-one $\text{Ac}^- \cdots \text{M}^{2+}$ binding free energies in aqueous MAc_2 solutions (where $\text{M} = \text{Zn}, \text{Mg}, \text{or Ca}$). We demonstrate that a Raman-MCR based spectral decomposition strategy may be used to obtain robust metal acetate binding constants, without relying on any *a priori* assumptions regarding the shapes of the unbound and bound acetate spectra. Our results further demonstrate that self-consistent one-to-one binding constants may be obtained from aqueous MAc_2 solutions with concentrations up to 0.5 M, using spectral decompositions of either the acetate CC or COO^- bands (or both). In addition, properly benchmarked simulations and quantum calculations allow us to address detailed structural and energetic issues concerning the modes of cation-carboxylate binding (i.e., contact vs. solvent-shared and, in the former case, monodentate vs. bidentate, see Figure 5.1), as deduced from spectroscopic measurements in this work as well as in previous studies.^{125,126,130,135–145}

5.2 Experimental Details

Sample preparation and Raman-MCR spectra. Sodium acetate (Mallinkrodt, 99+%), magnesium acetate tetrahydrate (Sigma Aldrich, 99+%), calcium acetate monohydrate (Sigma Aldrich, 99+%), zinc(II) acetate dihydrate (Sigma Aldrich, 98+%), and acetic acid (Sigma Aldrich, 99.7+%) were used without further purification. Aqueous solutions of sodium

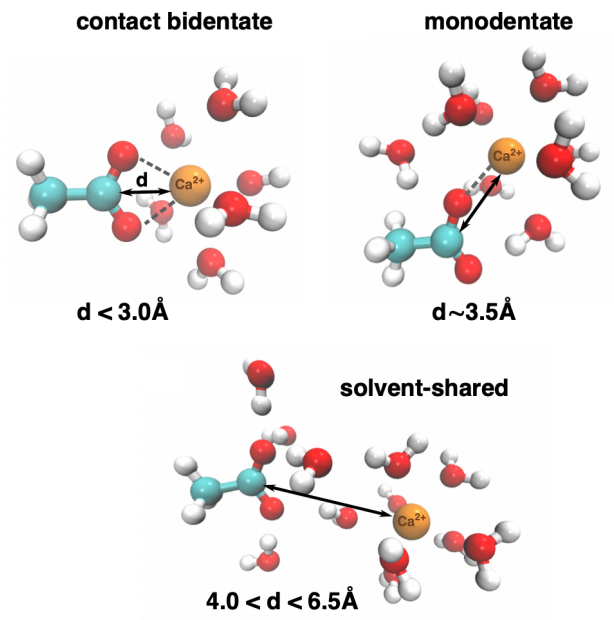


Figure 5.1. Sketch of the different cation-acetate ion pairing modes with the surrounding layer of water molecules, with typical associated C-cation distances (for a Ca^{2+} cation). Snapshots were prepared using the VMD software.¹⁴⁶

acetate (NaAc), magnesium acetate (MgAc_2), calcium acetate (CaAc_2), and zinc(II) acetate (ZnAc_2) were prepared by adding an appropriate mass of each solid to a volumetric flask and completing with ultra-purified water (Milli-Q UF Plus, 18.2 $\text{M}\Omega$ cm, Millipore) to obtain stock solutions of 4 M (Na^+ solutions), 2 M (Mg^{2+} and Ca^{2+} solutions), or 1.5 M (Zn^{2+} solutions). Solutions were sonicated for ~ 1 min to aid dissolution and were then diluted to obtain the desired concentrations.

Raman vibrational spectra were collected at 20 $^\circ\text{C}$ using a home-built instrument with a 514.5 nm Argon ion laser and 20 mW of power at the sample. For each sample, two to four spectra were collected with an integration time of 5 min. Raman-MCR spectra were obtained using the self-modeling curve resolution (SMCR) algorithm.^{2,3,5} In this procedure, measured Raman spectra of pure water and solutions were decomposed to obtain minimum area non-negative solute-correlated (SC) spectra, containing vibrational features arising from the solute itself and from the water molecules that are perturbed by the solute. Unless stated otherwise, all of the reported Raman-MCR solute-correlated (SC) spectra are normalized

to the solute CC band area. This normalization produces spectra whose CC band area is concentration independent, which is also the case when normalizing the SC spectra to the corresponding solute concentration. The CC normalization procedure is more effective than concentration normalization in suppressing variations due to drifts in the excitation laser intensity or optical alignment.

Binding constant determination. Raman-MCR SC spectra were used to determine the binding constants of acetate (Ac^-) to metal dications. For a given aqueous MAc_2 solution, the SC spectrum contains features arising from unbound Ac^- , bound Ac^- , and water molecules perturbed by these two acetate species as well as by the M^{2+} ions. Total least squares (TLS) analysis was applied to the SC spectra to estimate the concentrations of unbound Ac^- and bound Ac^- . This TLS procedure required obtaining the pure component spectra for the unbound and bound acetate species. The unbound component was chosen as the SC spectrum obtained from NaAc solutions (because the corresponding SC spectra are dominated by Ac^- , as Na^+ has a negligible influence on water structure,¹⁴⁷ and because there is little evidence of ion-pairing between Na^+ and Ac^- at concentrations up to 2 M, as further described in the Results section). The bound component, which is not readily evident in the measured SC spectra, was obtained using a second SMCR decomposition in which the contributions of unbound Ac^- (aqueous NaAc) were removed from the SC spectra pertaining to each MAc_2 solution (as described in Appendix D.1). The resulting second round SMCR SC spectrum contains vibrational features pertaining to the bound acetate MAc^+ species itself (as further described in the Results section).

For comparison of the Raman-MCR-based binding constants with previous estimates made at different ionic strengths, all values were extrapolated to zero ionic strength using the following Davies-like equation:^{148,149} $\Delta \log K = 0.51 \left(\frac{\sqrt{I}}{1+1.50\sqrt{I}} - 0.09I \right) \chi - 0.09I$, where I is the ionic strength, and χ is an integer that depends only on the charge and stoichiometry of the involved species ($\chi = 4$ for the dication/acetate systems).

5.3 Computational Details

All computational results presented in this chapter were obtained by the groups of Dr. Pavel Jungwirth (Academy of Sciences of the Czech Republic) and Dr. Elise Duboué-Dijon (CNRS, Université de Paris). The description of the computational methods can be found in our published work.¹⁰³ The computational work included classical molecular dynamics simulations performed with “scaled charge” force fields to compute ion-pairing binding free energy (results not shown here), DFT-based calculations of the Raman spectra of different ion pair configurations, and *ab initio* molecular dynamics to obtain free energy profiles of contact bidentate/monodentate ion pair conformations.

5.4 Results

Figure 5.2A shows Raman spectra of aqueous acetic acid and sodium acetate at similar concentrations. The major peaks in these spectra arise from the solute intra-molecular CC (near 900 cm^{-1}), COO^- (near 1500 cm^{-1}), and CH (near 2900 cm^{-1}) vibrational modes, as well as an OH band (near 3400 cm^{-1}) resulting primarily from water molecules. Comparison of the acetic acid and sodium acetate SC spectra reveals that deprotonation of carboxylic acid^{150,151} induces a significant redshift in the CO stretch band (from $\sim 1700 \text{ cm}^{-1}$ for COOH to $\sim 1400 \text{ cm}^{-1}$ for COO^-), as well as smaller shifts in the solute CC and CH bands. The observed redshift of the acetate COO^- band (relative to the acetic acid COOH band) is consistent with the fact that the extra electron is added to an antibonding orbital of the anion.^{151,152} Additionally, the larger intensity of the acetate COO^- band implies that the extra electron increases the corresponding polarizability derivative. Note that the acetic acid and acetate stretch CO bands overlap with smaller bands (shoulders) near 1350 cm^{-1} assigned to a CH_3 deformation mode.¹⁴¹

Figure 5.2B shows how the Raman-MCR SC spectra of sodium acetate vary with concentration (after normalization to the CC band area). These results indicate that there is essentially no concentration dependent shift or shape changes in the CC, COO^- , or CH bands in aqueous NaAc solutions, thus suggesting that there are no direct contacts between Na^+ and COO^- up to concentrations of $\sim 2 \text{ M}$ or that any direct contacts that are present do

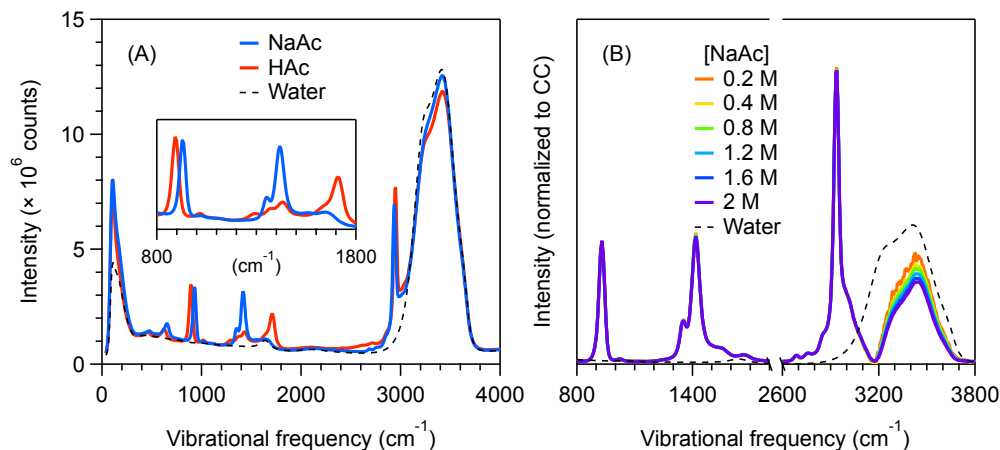


Figure 5.2. (A) Raman spectra of acetic acid and sodium acetate at approximately equal concentrations. (B) Raman-MCR SC spectra of sodium acetate solutions as a function of concentration. The water spectrum (dashed black) is for reference.

not significantly influence the acetate intramolecular vibrational modes. The only readily detectable concentration-dependent change in the aqueous NaAc Raman-MCR spectra is the slight decrease in the intensity of the NaAc Raman-MCR SC OH stretch band with increasing NaAc concentration, shown in Figure 5.2. This decrease in the OH band area suggests the presence of some water-separated contacts between Na^+ and Ac^- , as would be expected to occur even in a nominally non-ion-pairing mixture of Na^+ and Ac^- at concentrations above ~ 1 M.

Given the negligible concentration dependence of the acetate bands in aqueous NaAc Raman spectra, the SC spectrum of NaAc may be used as a free acetate reference to uncover evidence of acetate-dication binding in aqueous of $\text{M}(\text{Ac})_2$ solutions. Specifically, Figure 5.3 shows that the Raman-MCR SC spectra of $\text{Mg}(\text{Ac})_2$, $\text{Ca}(\text{Ac})_2$, and $\text{Zn}(\text{Ac})_2$ solutions are shifted with respect to that of aqueous NaAc, thus implying the presence of significant ion-pairing of acetate to Mg^{2+} , Ca^{2+} , and Zn^{2+} over this concentration range. Our assignment of these shifts primarily to direct-contact (as opposed to water separated) ion pairing is supported by the fact that the magnitudes of the observed blueshifts of the CC stretch band are consistent with those predicted by quantum calculations upon direct contact-ion pair formation, as further described in Appendix D.4.

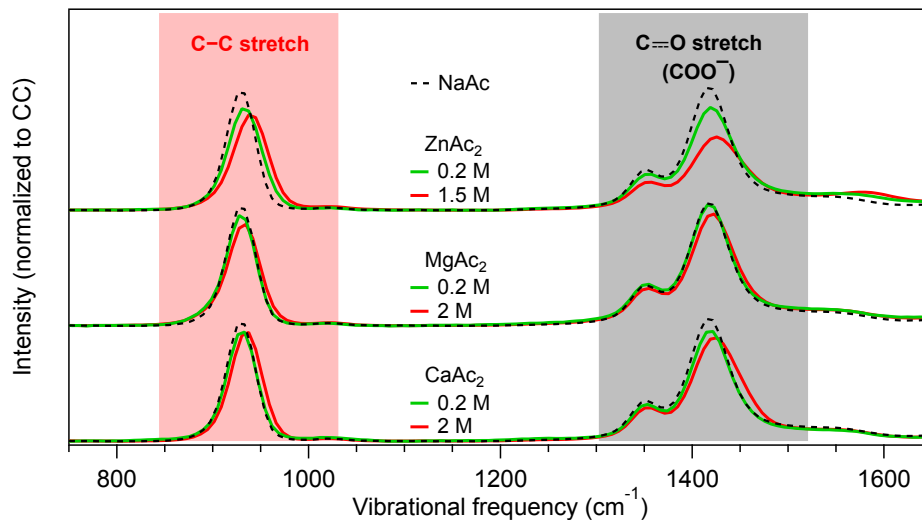


Figure 5.3. Concentration-dependent SC spectra of zinc(II) acetate (top), magnesium acetate (middle), and calcium acetate (bottom). The larger concentration dependent changes in the CC and COO^- stretching band intensity for ZnAc_2 clearly indicate that Zn^{2+} interacts more strongly with Ac^- than either Ca^{2+} or Mg^{2+} . The dashed black spectrum corresponds to aqueous sodium acetate and is included as reference for the unbound acetate spectrum. The spectra are vertically offset for clarity.

The results in Figure 5.3 further suggest that direct-contact ion-pairing of acetate to Zn^{2+} produces a larger spectral change than binding to either Ca^{2+} or Mg^{2+} , as evidenced by the larger concentration-dependent changes in the SC spectra of ZnAc_2 than either MgAc_2 and CaAc_2 at the same concentration. A quantitative experimental estimate of the corresponding binding constants can, in principle, be obtained by decomposing the measured spectra into a linear combination of the unbound and bound acetate spectra. This procedure requires knowing *a priori* the SC spectra of these two pure component acetate species. The spectrum of aqueous NaAc yields the unbound COO^- SC spectrum (as previously discussed). The spectrum of the bound acetate species is more difficult to unambiguously determine. However, we found that a self-consistent estimate of this spectrum may be obtained using a second round SMCR procedure in which the contribution of unbound acetate (obtained from the aqueous SC spectrum of NaAc) is removed from the SC spectra of aqueous MAc_2 solutions (as further described in Appendix D.1). Briefly, the second round SMCR analysis produces a

family of possible bound spectra, but only one member of this family is found to produce a self-consistent (concentration-independent) one-to-one binding constant over the experimental concentration range of 0.1 M to 0.5 M MAc_2 . The remaining members of the family of possible bound spectra include a mathematical lower bound minimum area spectrum (pertaining to the most tightly bound ion pairs with the smallest possible binding constant), as well as a distribution of other possible bound spectra whose shape approaches that of the free acetate (pertaining to the most loosely bound ion pairs with the largest binding constants). Although all of these bound spectra are mathematically possible, only one yields self-consistent one-to-one binding constants between acetate and each of the three cations. The robustness of the resulting binding constant is confirmed by very similar results obtained when performing the TLS spectral decomposition using only the CC or COO^- bands or by simultaneously fitting both bands.

Figure 5.4(A–C) shows the free (dashed black) and bound (dashed red) acetate spectra, obtained as described above, along with the measured SC spectrum for an aqueous 0.5 M MAc_2 solution (green curve). The inset spectra on the right-hand panels show the essentially perfect agreement between the TLS reconstructions (dotted black curves) and the measured 0.5 M SC spectra (solid green curves), where the TLS spectra represent a best-fit of the measured spectrum to a linear combination of the unbound and bound spectra. The yellow points in the right-hand panels in Figure 5.4 show the resulting bound acetate fraction obtained for solutions with MAc_2 concentrations up to 0.5 M, and thus total acetate concentrations up to 1 M. Note that these binding constants imply that Zn^{2+} has a binding constant to acetate ($K = 4.5 \pm 1.3$) that is about four times larger than Mg^{2+} ($K = 1.1 \pm 0.4$) and Ca^{2+} ($K = 1.1 \pm 0.4$). The experimental points in Figure 5.4 (D–F) are well fitted with a single 1:1 binding constant, which strongly suggests that no significant 2:1 binding occurs in this range of concentrations, in agreement with earlier ultrasonic absorption experiments.¹⁵³

5.5 Discussion

Several estimates of the cation–acetate binding constants are available in the literature and can be compared with the Raman-MCR results (Table 5.1). To do so, we extrapolated all the

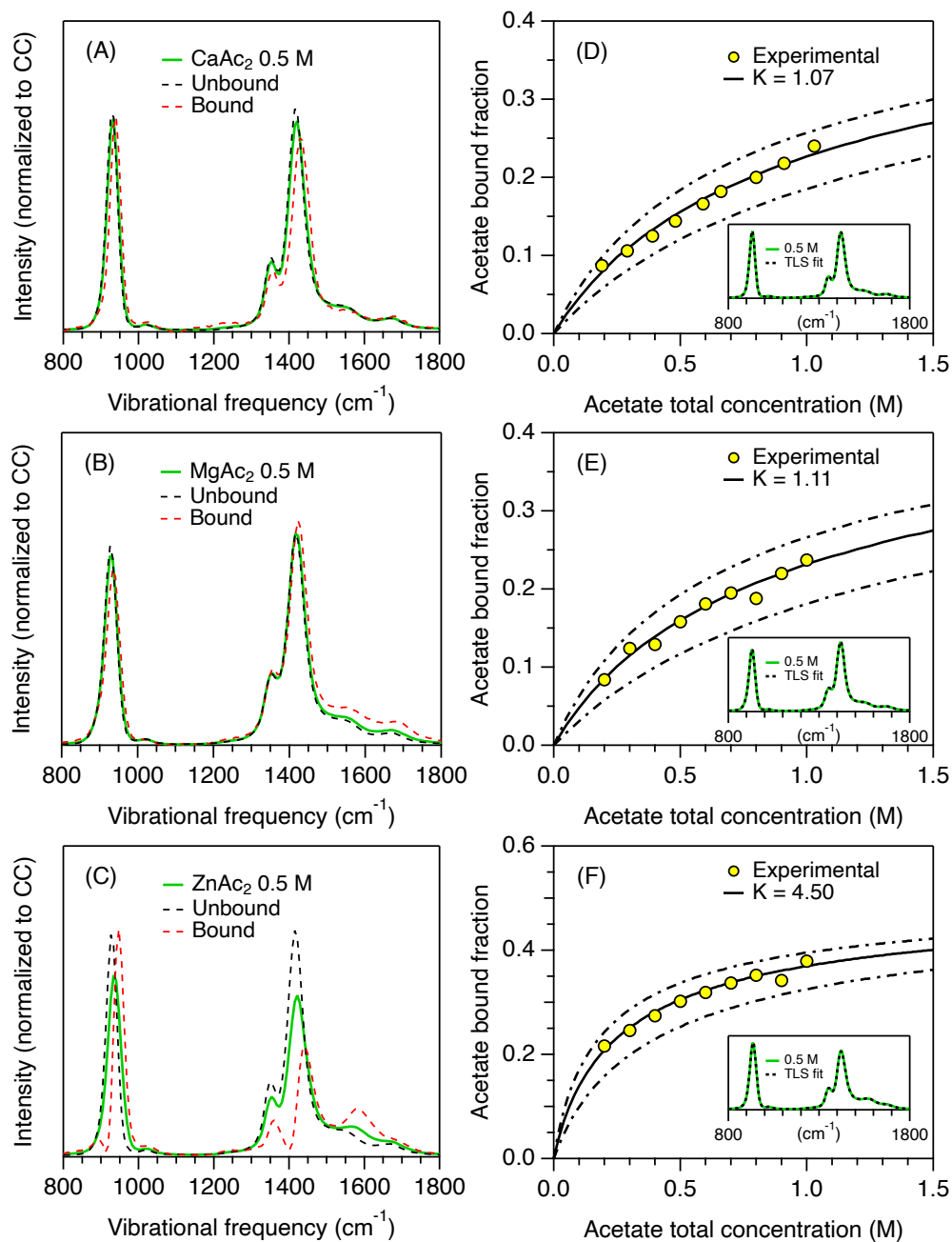


Figure 5.4. Free and bound component spectra (left-hand panels A–C) and binding curves (right-hand panels D–F) for magnesium (A and D), calcium (B and E) and zinc (C and F). The inset spectra in panels D–F compare the TLS reconstruction (dotted black curves) with the experimental SC spectrum (solid green curves) obtained for a 0.5 M solution of MAc_2 . The dot-dashed curves represent a 99% confidence interval for the binding constants.

values to zero ionic strength using a refined Davies-like equation¹⁴⁹ (if the extrapolation was not already performed in the original work). Note that previous data have been obtained with potentiometric measurements, with older reported data potentially suffering from the lack of correction for liquid junction potentials.^{120,134} In addition, while we have shown that the present Raman-derived binding constants mainly report on the formation of contact ion pair, it is not clear how sensitive the potentiometric measurements are with respect to different ion pair geometries, even if one would expect it to be also mostly, but probably not exclusively, sensitive to contact ion pairs. Keeping these remarks in mind, our results show that Zn^{2+} binds about four times more strongly to acetate than either Ca^{2+} or Mg^{2+} , in qualitative agreement with previous potentiometric measurements^{118,119} (and better quantitative agreement with more recently corrected potentiometric results¹²⁰ for acetate binding to Ca^{2+}). The difference between the binding constants of Ca^{2+} and Mg^{2+} is small and lies within experimental error. This is in line with all previous studies that reported very similar binding constants for the two cations, either slightly in favor of one or the other, the difference probably being in each case within experimental error.

Table 5.1. Comparison of the standard binding constant K° (extrapolated to zero ionic strength as described in Ref. [149]) for the formation of the 1:1 cation:acetate complex for different divalent cations, as obtained from Raman-MCR and previous studies.

	Raman-MCR	Ref. [119]	Ref. [118]	Ref. [123]	Ref. [120]
Ca^{2+}	3.6 ± 0.4	11.0	15.4 ± 1.1	10.4	2.7 ± 0.3
Mg^{2+}	3.9 ± 0.6	10.3	18.6 ± 1.0	9.5	n.a.
Zn^{2+}	16.0 ± 2.8	28.3	37.2	n.a.	n.a.

5.6 Conclusions

In this study, we quantified binding of Zn^{2+} , Ca^{2+} , and Mg^{2+} to acetate anions using a combination of Raman-MCR spectroscopic measurements and *ab initio* calculations. The Raman-MCR measurements yield self-consistent bound spectra and one-to-one binding

constants demonstrating that Zn^{2+} binds about four times more strongly to acetate than either Ca^{2+} or Mg^{2+} , in qualitative agreement with previous potentiometric measurements^{118,119} (and better quantitative agreement with more recently corrected potentiometric results¹²⁰ for acetate binding to Ca^{2+}). Quantum calculations further confirm that the Raman-MCR measurements are primarily sensitive to direct contact, as opposed to water-separated, ion pairing between the dications and the COO^- group, and suggest that the experimentally detected bound species may include both monodentate and bidentate binding to Zn^{2+} , but primarily monodentate binding to Mg^{2+} (over the experimental concentration range). Our results clearly demonstrate that the binding of acetate to these three cations does not scale with cation size, as both Zn^{2+} and Mg^{2+} are about 25% smaller than Ca^{2+} .¹⁵⁴ The observed binding constants also do not scale with ion polarizability, as Zn^{2+} and Ca^{2+} are about twice as polarizable as Mg^{2+} .¹⁵⁵ The more favorable binding of acetate to Zn^{2+} may perhaps be related to its higher electron binding affinity than either Mg^{2+} or Ca^{2+} (as inferred from the corresponding second ionization potentials),¹⁵⁶ and perhaps also to the fact that the valence electrons of Zn^{2+} are in d-orbitals while those of Mg^{2+} and Ca^{2+} are in p-orbitals.

Our combined experimental and theoretical results demonstrate both the promise and outstanding challenges associated with quantifying non-covalent ion-pairing interactions in aqueous solutions. The stronger acetate binding of Zn^{2+} than either Mg^{2+} or Ca^{2+} undoubtedly has biological implications to such processes as calcium signaling, stabilization of nucleic acids by magnesium, and zinc-mediated enzymatic activity. Our results also highlight the challenges associated with quantitatively linking experimental and theoretical ion-pairing results, including the need for improved cation force fields and improved procedures for resolving the range of ion-paired structures detected using different experimental methods.

6. WATER-SHARED ION PAIRING IN AQUEOUS HYDROXIDE SOLUTIONS

A version of this chapter was published in a peer-reviewed journal as:

Mendes de Oliveira, D.; Bredt, A. J.; Miller, T. C.; Corcelli, S. A.; Ben-Amotz, D. Spectroscopic and structural characterization of water-shared ion pairs in aqueous sodium and lithium hydroxide. *J. Phys. Chem. B* **2021**, 125, 1439–1446.

Abstract. The structures of the ion pairs formed in aqueous NaOH and LiOH solutions are elucidated by combining Raman multivariate curve resolution (Raman-MCR) experiments and *ab initio* molecular dynamics (AIMD) simulations. The results extend prior findings to reveal that the initially formed ion pairs are predominantly water-shared, with the hydroxide ion retaining its full first hydration shell, while direct contact ion pairing only becomes significant at higher concentrations. Our results confirm previous experiments and simulations indicating greater ion pairing in aqueous LiOH than NaOH as well as at high temperatures. Our results further imply that NaOH and LiOH ion pairing free energies have an approximately linear (rather than square-root) dependence on ion concentration (in the molar range), with positive enthalpies and entropies that increase with concentration, thus implying that water-mediated interactions enthalpically disfavor and entropically favor ion pair formation.

6.1 Introduction

The tactile slipperiness and chemical activity of alkaline water are linked to the influence of hydroxide (OH^-) ions and their counteranions on water structure and dynamics.^{157–164} The influence of the counteranion is evidenced, for example, by the marked differences between the conductivity^{158,159} and proton transfer dynamics¹⁵⁷ in aqueous NaOH and LiOH. Although these differences are due in part to the greater abundance of ion pairs in LiOH solutions, as well as in both solutions at higher temperatures,^{158,159,161,164} open questions remain as to whether the corresponding ion pairs are best characterized as direct, water-shared, or water-separated, depending on whether there are 0, 1, or 2 water molecules between the paired counterions.¹³⁴ To address this question, as well as to spectroscopically, structurally, and

thermodynamically quantify ion pairing in aqueous NaOH and LiOH solutions, we performed Raman multivariate curve resolution (Raman-MCR)⁶ experiments and *ab initio* molecular dynamics (AIMD) simulations. Our results confirm that strong $\text{HOH} \cdots \text{OH}^-$ hydrogen bonds stabilize the first hydration shell of OH^- and thus favor the formation of water-shared ion pairs between Na^+ or Li^+ and hydrated OH^- . Moreover, our concentration and temperature dependent measurements imply that the ion pairing free energies have an approximately linear (rather than square-root) concentration dependence and are enthalpically disfavored and entropically favored to a degree that increases with increasing concentration.

The present results may be viewed as extending a recently reported Raman-MCR and AIMD study,¹⁵⁷ as well as prior ion pairing^{164–170} and hydration^{171–175} studies, to better characterize and quantify ion pairing in aqueous NaOH and LiOH solutions. Our conclusion that the tightly bound hydration shell of OH^- promotes water-shared ion pairing is complementary to a recent Raman study of aqueous MgCl_2 and LaCl_3 that attributed water-shared ion pairing to the tightly bound hydration shells of the multivalent cations.¹⁷⁰ More generally, the high solubility of ions in water implies that ion-water interactions can overcome the intrinsic attraction of counter ions for each other. Such water-mediated interactions may in some cases even facilitate the pairing of like-charged ions in water and at air-water interfaces.^{176–178} Our results add to the associated intrigue by revealing that ion pairing can be entropically rather than enthalpically favored, thus providing further evidence that water-mediated interactions may be more significant facilitators of ion pairing than the electrostatic interactions between ions.

6.2 Methods

Experimental Measurement and Analysis Methods. Aqueous solutions of NaOH (sodium hydroxide, ACROS Organics, 98.5%) and LiOH (lithium hydroxide, Sigma-Aldrich, 98%) were prepared with ultrapure filtered water (Milli-Q UF Plus, Millipore, 18.2 M Ω cm). Raman spectra were obtained using an Ar-ion 514.5 nm laser with ~ 20 mW of power at the sample and 5 min of integration time, as previously described.³ Briefly, backscattered Raman photons were collected from the sample using a 20 \times long-working-distance microscope

objective (NA = 0.42, Mitutoyo Inc.) and transmitted with an optical fiber bundle to an imaging spectrograph (SpectraPro300i, Acton Research Inc.) equipped with a 300 grooves/mm grating and a thermoelectrically cooled CCD camera (Princeton Instruments Inc.).

Raman spectra were obtained at concentrations between 0.25 and 2 M at temperatures of 5, 10 and 20 °C for LiOH, as well as at 40 °C for NaOH. For NaOH at 5 °C, spectra were obtained over a wider concentration range of 0.25–10 M. In addition, temperature-dependent spectra were obtained from 0.5 M LiOH and NaOH solutions over a 0–100 °C temperature range. The measured spectra were all smoothed using a 15-point Savitzky-Golay filter. The spectra were subsequently treated using self-modeling curve resolution (SMCR) decomposition^{2,5,6,31} to obtain minimum area non-negative solute-correlated (SC) spectra from pairs of pure water and solution spectra collected under identical experimental conditions at ambient pressure and temperatures regulated to within < 0.1 °C. The minimum-area constraint was applied in the spectral region between 2000 and 4000 cm⁻¹ after subtraction of a broad low-intensity background using a fourth order polynomial fit to baseline points adjacent to the OH stretch band (see Appendix E.2). The SC spectra were divided by the corresponding total hydroxide concentration so that the resulting SC spectra are effectively normalized to the same concentration.

Estimates of the ion-pairing association constants in aqueous NaOH and LiOH were obtained from the SC intensities near 3500 cm⁻¹ (determined as described in Appendix E.1) which are found to decrease strongly upon ion pair formation. Thus, the fraction of free (non-ion-paired) hydroxide ions, x_F , may be experimentally estimated using Eq. 6.1, which equates x_F with the ratio of the measured intensity I of the normalized SC spectrum at a given concentration $c_T = [\text{MOH}]_T$ (where M = Na or Li) and the intensity I_0 in the dilute limit, at which the ions are assumed to be completely dissociated.

$$x_F = \frac{[\text{OH}^-]_F}{c_T} = \frac{[\text{M}^+]_F}{c_T} \approx \frac{I}{I_0} \quad (6.1)$$

The dissociated fraction x_F , pertaining to an ion pairing equilibrium of the form $M^+ + OH^- \rightleftharpoons MOH$, may further be related to the ion-pairing association constant K_A as follows.

$$x_F = \frac{-1 + \sqrt{1 + 4K_A c_T}}{2K_A c_T} \quad (6.2)$$

Note that we define the equilibrium constant as a ratio of concentrations (not activities). Thus, at higher concentrations, K_A is expected to be concentration dependent. As we will see, our experimental results imply that the corresponding free energy $\Delta G = -RT \ln K_A$ has an approximately linear concentration dependence, thus implying that K_A is described by Eq. 6.3, in which K_0 is the association constant at infinite dilution and the coefficient b dictates the linear concentration dependence of $\Delta G = \Delta G_0 - RT(bc_T)$, with ΔG_0 corresponding to the ion pairing free energy (potential of mean force) at infinite dilution.

$$K_A = K_0 \exp(bc_T) \quad (6.3)$$

Equations 6.2 and 6.3 may thus be used to obtain K_0 and b by fitting the experimentally determined x_F as a function of c_T (as described in greater Appendix E.1).

The ion pairing thermodynamic functions are related to K_A and its temperature dependence, as follows.

$$\Delta G = -RT \ln(K_A) \quad (6.4)$$

$$\Delta S = - \left(\frac{\partial \Delta G}{\partial T} \right)_P \quad (6.5)$$

$$\Delta H = \Delta G + T\Delta S \quad (6.6)$$

Simulation Methods. All simulation results presented here were obtained by the group of Dr. Steven Corcelli (University of Notre Dame). The following is a description of the methods used in the computational part of this work.

Simulation boxes of 1 M LiOH and 1 M NaOH were built with Packmol,¹⁷⁹ where each system contains 110 H₂O, 2 OH⁻, and 2 counterocations. *Ab initio* molecular dynamics (AIMD) simulations are performed utilizing the CP2K open source molecular dynamics package.¹⁸⁰

To start, a short geometry optimization of the atomic coordinates was performed before DFT-based AIMD equilibration (20 ps) and production (200 ps) in the NVT ensemble, similar to the protocol previously used for studying excess protons in water.^{181,182} Born-Oppenheimer molecular dynamics were implemented to propagate the nuclei with a timestep of 0.5 fs. CP2K uses the Quickstep method for force evaluations wherein the Gaussian and plane waves scheme is utilized.¹⁸³ We implemented the Goedecker-Teter-Hutter (GTH) pseudopotentials^{184–186} for treatment of the core electrons, the TZVP-GTH basis set, and the BLYP functional^{187,188} for exchange-correlation contributions with Grimme’s D3 correction.¹⁸⁹

The often-used radial distribution function loses or hides a large amount of structural information about the solvation environment when applied to molecules with a non-spherical symmetry. By introducing a second dimension to the distribution function, such as one along a bond axis, a two-dimensional mapping of the solvation environment around a cylindrical molecule can be calculated, i.e., a cylindrical distribution function (CDF).¹⁹⁰ The CDF, $g(r, z)$, depends on the radius of a ring, r , around the molecule of interest, and a “height” of the particle of interest in a plane about the central atom, z . Here the CDFs are centered on the hydroxide ion, thus the “height” parameter is defined as

$$z = \hat{\nu}_{\text{OH}} \cdot \vec{\nu}_{\text{O}i} \quad (6.7)$$

where $\hat{\nu}_{\text{OH}}$ is the unit vector from the hydroxide oxygen (defined as the $r = 0$, $z = 0$ position) to the hydroxide hydrogen, and $\vec{\nu}_{\text{O}i}$ is a vector from the central oxygen atom to the particle of interest. The radius of the ring for the particle of interest can then be obtained by

$$\vec{r} = \vec{\nu}_{\text{O}i} - z\hat{\nu}_{\text{OH}} \quad (6.8)$$

which gives the inner radius of a ring around the hydroxide oxygen that is shifted up or down by z . Each unique combination of r and z defines a ring around OH^- in which counterions or solvent molecules can reside. The resultant data set is visualized as a two-dimensional histogram in which the value at each (r, z) location represents the total population in the ring of radius r and displaced along the O–H axis by a distance z with respect to the oxygen atom.

6.3 Results

Figure 6.1 contains experimental (upper panels) and simulation (lower panels) results pertaining to aqueous NaOH and LiOH solutions. Figure 6.1(A) compares Raman spectra of pure water and aqueous NaOH, all of which look quite similar, although the 2 M NaOH solution spectra show evidence of an emerging OH^- stretch peak near 3600 cm^{-1} and a low frequency OH tail below 3000 cm^{-1} . These features are more clearly evident in the SC spectra shown in panel (B) obtained from 0.5 M and 2 M solutions at 20°C normalized to the same concentration. The normalization procedure highlights concentration dependent changes resulting from ion pairing, as all the normalized SC spectra would look identical if the ions remained fully dissociated. Note that such SC spectra may in general contain vibrational features arising from water molecules whose vibrations are perturbed by one or both of the counter-ions of NaOH and LiOH, as well as the OH stretch vibration of OH^- itself, which gives rise to the relatively sharp peak near 3600 cm^{-1} .^{157,191} The remaining hydration shell features that appear in the SC spectra in Figure 6.1(B) were assigned with the aid of AIMD simulations.

The broad low frequency feature in the SC spectra shown in Figure 6.1(B) is assigned to $\text{HOH}\cdots\text{OH}^-$ water molecules directly hydrogen bonded to OH^- .¹⁵⁷ The nearly constant intensity of this low frequency tail in all these normalized SC spectra indicates that the first hydration-shell of OH^- is strongly bound, thus suppressing the formation of direct contact ion pairs between OH^- and either Na^+ or Li^+ over this concentration range. This conclusion is consistent with the predicted distributions of Na^+ and Li^+ around OH^- at 1 M, shown in Figure 6.1(C) and (D), which indicate that water-shared ion pairs far outnumber direct contact ion pairs. Further support for this conclusion is provided by our additional AIMD simulation predictions that OH^- remains essentially fully hydrated in both 1 M NaOH and LiOH aqueous solutions (see Appendix E.3).

The simulation results shown in Figure 6.1(D) further reveal that the cations in the water-shared ion pairs are located about 3 \AA away from OH^- , consistent with the ion pairing induced displacement of water molecules from the second hydration shell of OH^- . Note that water-separated (rather than water-shared) ion pairs, in which both the cation and anion

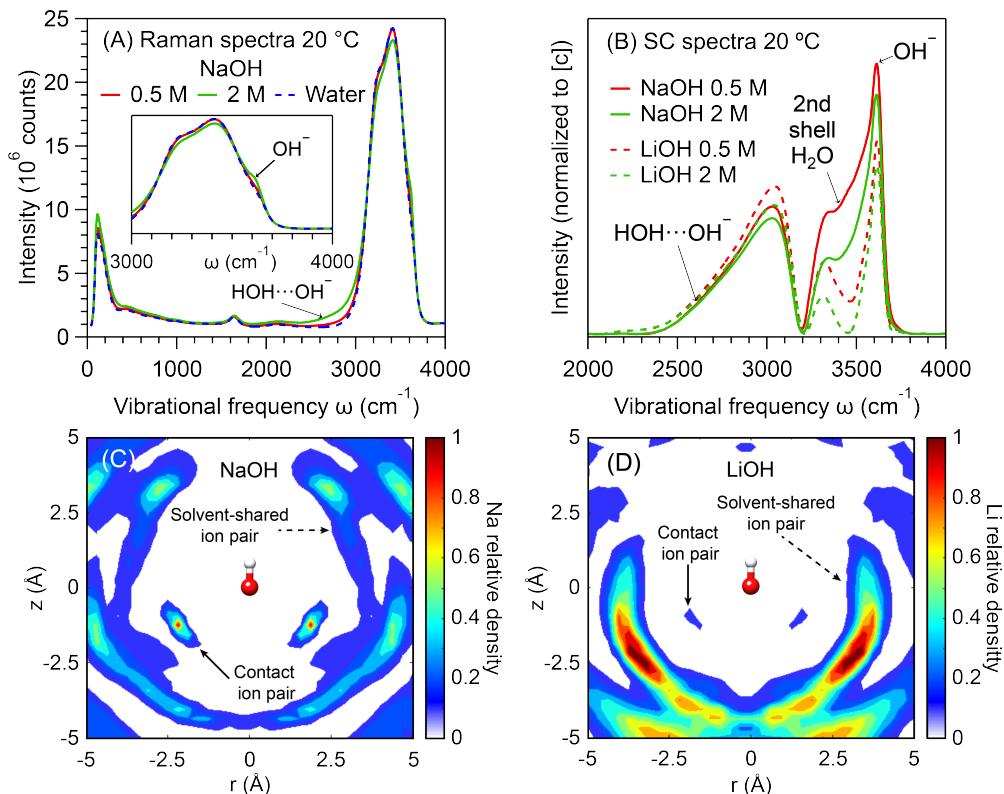


Figure 6.1. Experimental (upper panels) and simulation (lower panels) results for aqueous NaOH and LiOH. Experimental Raman spectra of aqueous NaOH (A) and Raman-MCR of aqueous NaOH and LiOH (B) at 20 °C and both 0.5 M and 2 M. AIMD predictions of the distributions of Na^+ (C) and Li^+ (D) around OH^- at 1 M and 25 °C. See the experimental and simulation methods for further details.

retain their first hydration shell, would have a larger cation-anion separation of at least 5 Å. Moreover, the structure and spectra of the hydration shell water molecules around such water-separated ion pairs would be expected to resemble the corresponding fully hydrated ions, and thus Raman-MCR is expected to be relatively insensitive to water-separated ion pairing.

Water-shared ion pairing, on the other hand, should significantly alter the ion pair hydration-shell structure and spectra. The concentration dependent decrease in the hydration shell intensity near 3500 cm^{-1} , shown in Figure 6.1(B), is thus assigned to the ion pairing induced displacement of second hydration-shell water molecules around OH^- . This assignment

is supported by the fact that the vibrational frequencies of such second hydration-shell water molecules are predicted to occur in this spectral region.¹⁵⁷ Moreover, the OH population whose frequency is near 3500 cm^{-1} is similar to that of water molecules directly hydrogen bonded to large anions such as I^- .³¹ Thus, the hydrogen bonds donated from the second hydration shell water molecules to the hydrated OH^- are apparently similar in strength to those of water molecules directly hydrogen bonded to I^- .

The SC spectral comparisons in Figure 6.1(B) further imply that there are fewer water-shared ion pairs in NaOH than in LiOH, as indicated by the larger intensity near 3500 cm^{-1} in NaOH than in LiOH. The greater ion pairing propensity of LiOH than NaOH is also consistent with the simulation results shown in Figure 6.1(C and D), as well as with prior potentiometric measurements indicating that the ion pairing association constant of LiOH is about three times larger than that of NaOH.¹⁵⁸

Although Na^+ has little influence of the vibrational spectrum of water,¹⁴⁷ that is not the case for the higher-charge density Li^+ cation, whose hydration shell spectrum gives rise to a SC OH stretch band extending from 3000 cm^{-1} to 3500 cm^{-1} (see SI Figure S10 for ref. [181]). Thus, while the SC spectrum of NaOH is due primarily to OH^- and its hydration shell, the LiOH SC spectra are also influenced by the hydration shell of Li^+ . Nevertheless, any concentration dependent changes in the SC spectra of either NaOH or LiOH must necessarily result from the formation ion pairs (while the infinitely dilute SC spectra pertain to two fully separated and hydrated ions). It has previously been suggested that the observed Raman intensity decrease in aqueous NaOH and LiOH near 3500 cm^{-1} may be influenced by a decrease in the Raman cross-section of the ion pair hydration shell water molecules.¹⁵⁷ Although such a cross section decrease is plausible, the observed intensity decrease is also consistent with that expected to result from the displacement of water molecules from the second hydration shell of OH^- by the countercations.

Figure 6.2 compares the concentration and temperature dependence of the SC spectra of aqueous NaOH and LiOH. The qualitative similarity of the NaOH SC in Figure 6.2(A and B), particularly over the 3200 cm^{-1} to 3500 cm^{-1} spectral range, implies that the increase in NaOH ion pairing between 0.25 and 10 M (at $5\text{ }^\circ\text{C}$) is similar to that in a 0.5 M solution over a temperature range between $5\text{ }^\circ\text{C}$ and $100\text{ }^\circ\text{C}$. The nearly zero intensity near 3500 cm^{-1}

in the highest concentration and temperature SC spectra implies that an aqueous NaOH solution is essentially completely ion paired both at 10 M and 5 °C and at 0.5 M and 100 °C.

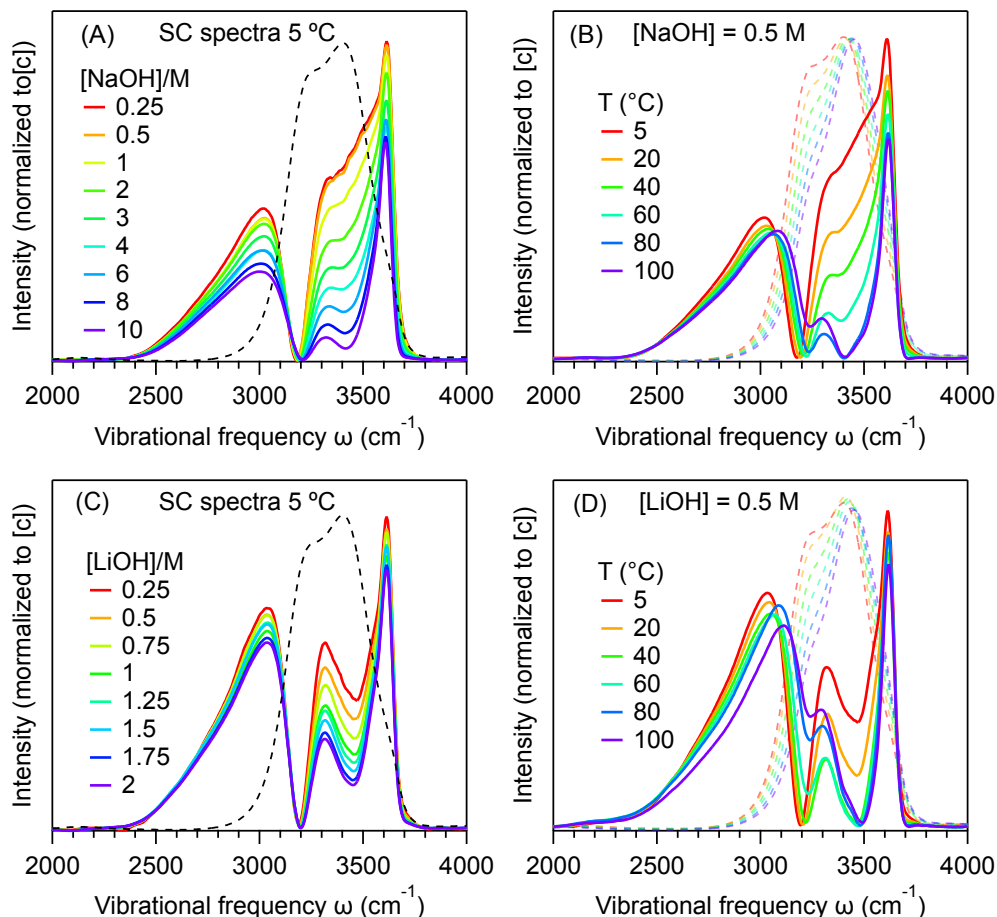


Figure 6.2. Comparison of the concentration (A and C) and temperature (B and D) dependent Raman-MCR hydration shell spectra of aqueous NaOH (A and B) and LiOH (C and D). The dashed curves are pure water spectra at the specified temperatures (scaled to approximately the same peak intensity).

The concentration dependence of the lower frequency HOH \cdots OH⁻ tail shown in Figure 6.2(A) differs somewhat from that of the temperature dependent spectra in Figure 6.2(B). Specifically, Figure 6.2(A) reveals a concentration dependent decrease in the area of the broad low frequency OH band, indicating that at concentrations above 2 M some of the water

molecules directly bound to OH^- are displaced by Na^+ , implying the formation of some direct contact ion pairs at such high concentrations, as previously determined using x-ray diffraction measurements.¹⁶² On the other hand, the temperature dependent spectra in Figure 6.2(B) reveal that the low frequency OH tail has an area that is nearly temperature independent, thus indicating that there are few direct contact ion pairs in a 0.5 M NaOH even at 100 °C, where the solution consists almost entirely of water-shared ion pairs. The temperature dependent spectra in Figure 6.2(B) further reveal a blue-shift in the low frequency OH band, consistent with the weakening of the $\text{HOH}\cdots\text{OH}^-$ hydrogen bonds with increasing temperature.

The SC spectra of LiOH shown in Figures 6.2(C and D) are qualitatively similar to those of NaOH in Figures 6.2(A and B), except for the lower intensity near 3500 cm^{-1} for LiOH than for NaOH, again reflecting the greater ion pairing in LiOH (as well as perhaps also some influence of the Li^+ hydration shell).^{147,181} Note that the concentration range of the aqueous LiOH solutions is smaller than that of the NaOH solution, due to the lower solubility of LiOH. Comparison of the concentration and temperature dependent SC spectra of aqueous LiOH indicates that the increased ion pairing in LiOH at concentration from 0.25 M to 2 M is somewhat smaller than that induced by increasing the temperature from 5 °C to 100 °C at 0.5 M. The nearly zero intensity near 3500 cm^{-1} in the SC spectra at 0.5 M and 100 °C again implies that this aqueous LiOH solution consists nearly entirely of water-shared ion pairs. Moreover, as in aqueous NaOH, the somewhat different concentration and temperature dependence of the low frequency OH band indicates that some direct contact ion pairs are formed at 2 M and 5 °C, while in a 0.5 M solution and 100 °C there are fewer direct contact ion pairs and the $\text{HOH}\cdots\text{OH}^-$ hydrogen bonds are again weakened with increasing temperature.

The spectra shown in Figure 6.2 also contain a peak near 3300 cm^{-1} that becomes most clearly evident at high concentrations and temperatures. This peak may perhaps be associated with the water OH groups in the first hydration shell of OH^- that are not hydrogen bonded to OH^- . This assignment is supported by prior predictions of the Raman and IR spectra of aqueous NaOH and LiOH solutions, indicating that such first hydration shell OH groups should have a vibrational frequency in this spectral range¹⁵⁷

Figure 6.3 shows results illustrating the more quantitative ion pairing information that may be obtained from the concentration dependent Raman-MCR results in Figure 6.1(A and C).

The points in Figure 6.3 correspond to the experimentally determined fraction of dissociated ion pairs, $x_F = I/I_0$ (see Eq. 6.1). Again, this expression for x_F assumes that a fully formed water-shared ion pair has a nearly vanishing intensity in the near 3500 cm^{-1} , as implied by the highest concentration and temperature spectra shown in Figure 6.2. Comparison of the NaOH and LiOH results in Figures 6.3(A and B) clearly reveal the greater degree of ion pairing (lower x_F values) in aqueous LiOH than in aqueous NaOH.

The dashed curves in Figure 6.3 are predictions obtained assuming that the ion pairing association constant is concentration independent, $K_A = K_0$, and has a value equal to that obtained from the experimental first derivative of x_F with respect to $[\text{MOH}]_T$ at infinite dilution. The discrepancy between the dashed curves and the data points at higher concentrations thus clearly indicates that the ion pair association constants increase with increasing $[\text{MOH}]_T$. The dotted curves in Figure 6.3 are obtained using Eq. 6.3, with K_0 and b taken from quadratic fits to the x_F values as a function of $c_T = [\text{MOH}]_T$ (as further described in Appendix E.1). Recall that b determines the linear increase in the ion pairing free energy ΔG with increasing ionic strength $\mu \sim c_T$. A significantly poorer fit to the x_F points is obtained if it is assumed that the ion-pairing free energy scales with either $\sqrt{\mu}$ or $\sqrt{\mu}/(1 - \sqrt{\mu})$, rather than μ . Moreover, when both a linear and a square-root dependence is included in the fit, the linear coefficient invariably dominates.

The ion pairing constants obtained using the results shown in Figure 6.3 may be compared with those previously obtained using potentiometric measurements. Specifically, ion pairing association constants of NaOH and LiOH, extrapolated to infinite dilution, are $K_0 = 0.25\text{ M}^{-1}$ and 0.61 M^{-1} , respectively. The factor ~ 2.5 difference between these two K_0 values is comparable to that obtained potentiometrically, although our K_0 values are roughly a factor of two smaller than the potentiometric values.¹⁵⁸ Our results further indicate that the ion pairing equilibrium constant K_A invariably increases with concentration, as does the ratio of the LiOH and NaOH ion pairing constants. For example, at $[\text{MOH}]_T = 2\text{ M}$ the ion pairing association constant ratio increases to $K_A(\text{LiOH})/K_A(\text{NaOH}) \sim 8$, as obtained using Eq. 6.3 with the coefficients shown in Figure 6.3 (and Table E.1).

The lower two panels in Figure 6.3 show the experimental ion pairing thermodynamic functions obtained using Eqs. 6.3–6.6, from the temperature and concentration dependence

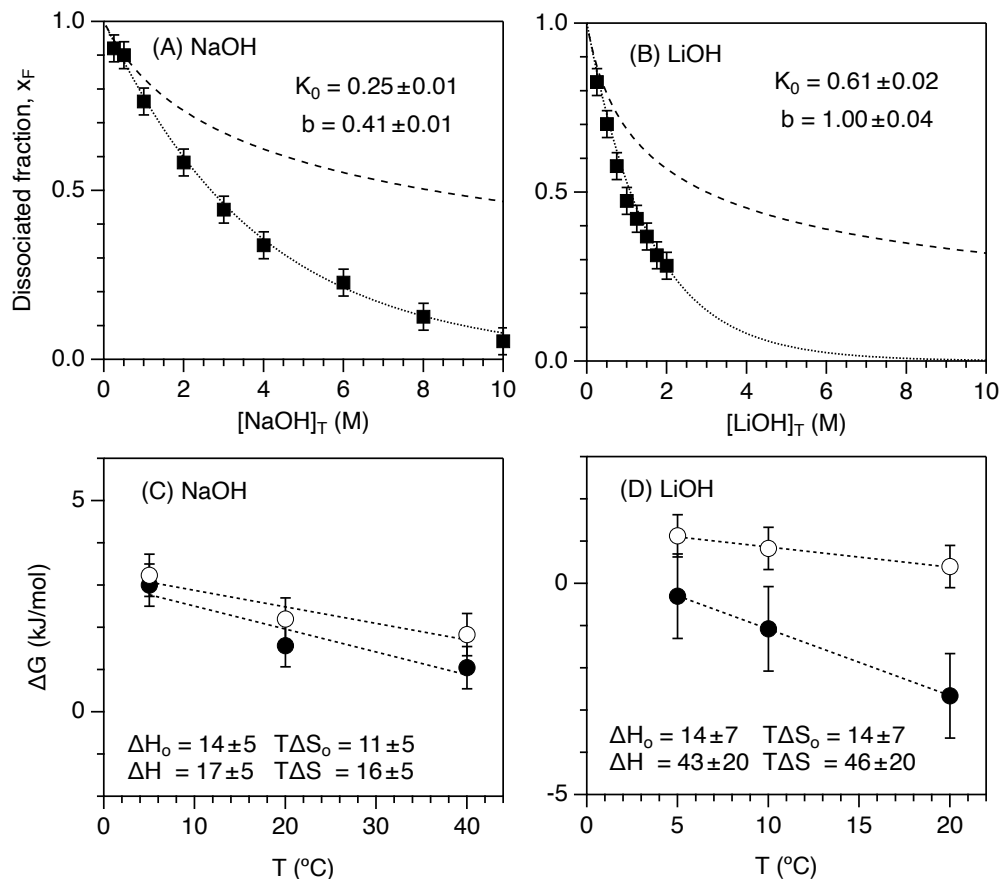


Figure 6.3. Ion pair dissociation fractions x_F (A and B) and thermodynamics (C and D) obtained from concentration dependent changes in the Raman-MCR SC spectra intensity near 3500 cm^{-1} in NaOH (A and C) and LiOH (B and D) solutions at 5°C . The experimental square points in (A) and (B) are compared with theoretical predictions obtained assuming a concentration independent ion pairing constant K_0 (match to the experimental results at infinite dilution), as well as a best fit of the experimental results to Eq. 6.3, which assumes that the ion pairing free energy decreases linearly with increasing concentration. The ion-pairing free energy ΔG , enthalpy ΔH and entropy ΔS (expressed in kJ mol^{-1}) at 20°C are obtained using Eqs. 6.4–6.6. The thermodynamic functions with a 0 subscript pertain to the dilute limit, and the non-subscripted functions pertain to a 1 M solution.

of x_F . Specifically, at each temperature the intensity near 3500 cm^{-1} was fit to a quadratic function of concentration. The SC intensities were measured at five neighboring frequency values near 3500 cm^{-1} , at each temperature and concentration. Results obtained at each of

the five frequencies were used to obtain the average and standard deviation of K_0 and b , as well as the corresponding ion pairing thermodynamic function (as further described in Appendix E.1).

The plots in Figure 6.3(C and D) reveal that the ion pairing free energy (obtained using Eq. 6.4) invariably decreases with increasing temperature, reflecting the increase in ion-pairing with increasing temperature. The negative slope of ΔG indicates that ΔS is positive (see Eq. 6.5). Since the magnitudes of $T\Delta S$ are invariably larger than ΔG , that further implies that $\Delta H = \Delta G + T\Delta S$ is also invariably positive. Although there is significant uncertainty associated with the magnitudes of ΔH and $T\Delta S$, their positive signs indicate that ion pairing is invariably enthalpically disfavored and entropically favored, contrary to ion pairing in the gas phase that must be strongly enthalpically favored and entropically disfavored. Our results further imply that the magnitudes of the positive ion pairing ΔH and ΔS values increase with increasing concentration, reflecting the larger solvent-mediated interactions in tin concentrated aqueous salt solutions.

6.4 Summary and Discussion

Our Raman-MCR experiments and AIMD simulations have confirmed that ion pairs in aqueous NaOH and LiOH solutions have a predominantly water-shared structure (rather than direct contact or water-separated structure). The stability of these ion pairs increases strongly with increasing temperature and is greater in LiOH than NaOH. The formation of the ion pairs leads to a decrease in the hydration-shell spectral intensity near 3500 cm^{-1} , in agreement with previously reported Raman-MCR and AIMD results.¹⁵⁷ Our findings go beyond previous work in experimentally quantifying the ion pairing equilibrium constant as a function of both concentration and temperature, to obtain the corresponding ion pairing thermodynamic functions, as well as a more detailed description of the water-shared ion pair structures.

Our observation that the ion-pairing free energy has an approximately linear concentration dependence appears to contradict the Debye-Hückel prediction that the activity coefficients of ions in water should scale as the square-root of ionic strength $\sqrt{\mu}$, or its generalizations

by Davies and others.^{148,149} However, those predictions pertain to concentrations well below 1 M. The observed linear, rather than square root, dependence that we have observed at higher concentrations is reminiscent of the fact that the experimental excess chemical potentials (solvation free energies) of various aqueous salt solutions are found to have an approximately quadratic dependence on $\sqrt{\mu}$ (and thus an approximately linear correlation with μ) at concentrations comparable to those of the present Raman-MCR measurements (see, for example, section 2.17 in ref. [192]).

We report the first measurements of ΔH and $T\Delta S$ for aqueous NaOH and LiOH, although prior potentiometric measurements have reported that ion pairing in these solutions increases with increasing temperature,^{158,159} thus confirming that ΔS is positive. Moreover, some other aqueous ion pairing processes have also been found to have positive ΔH and ΔS .^{134,158} Although our ion pairing ΔH and ΔS are significantly uncertain, in part because of the assumption that the formation of a water-shared ion pair fully depletes the SC spectral intensity near 3500 cm⁻¹, relaxing that assumption is not expected to change the derived ion pairing equilibrium constants by more than about a factor of two, and thus would only change ΔG by approximately $-RT \ln 2$ (of the order of 1 kJ mol⁻¹). Thus, there is little doubt regarding our conclusion that both ΔH and $T\Delta S$ are positive and large compared to ΔG .

Since the intrinsic interaction energy of the counter-ions with each other (in the absence of water) is necessarily negative, the observed positive sign of ΔH must arise from water-mediated interactions. These may include both direct ion-water interactions and indirect ion-induced changes in water-water interactions. In the linear response (and dielectric continuum) approximation, direct ion-water interaction energies are predicted to be twice as large in magnitude, and opposite in sign, to the corresponding indirect water-water interaction energies.¹⁹³ Thus, our experimentally observed positive sign of ΔH implies that it arises from the decrease in the large negative direct ion-water interaction energy upon ion pairing. Moreover, the fact that the magnitudes of ΔH increases with increasing concentration indicates that direct ion-solvent interactions are larger in concentrated aqueous ionic solvents than in pure water. Similarly, the positive sign of ΔS indicates that the thermally accessible

configurational phase space available to the solution increases upon ion pairing and is larger in concentrated aqueous NaOH and LiOH than at infinite dilution.

Our results suggest that Raman-MCR may be more generally applicable to other ion pairing process, as exemplified by the recent Raman-MCR investigation of the binding of Zn^{2+} , Ca^{2+} , and Mg^{2+} to carboxylate anions.¹⁹⁴ Our thermodynamic results also imply that it can be a mistake to assume that ion pairing in water is primarily driven by the electrostatic attraction between the oppositely charged ions. Rather, our results demonstrate the ion–water interactions can dominate the resulting thermodynamics, leading to enthalpic destabilization of the ion pair resulting from the loss of ion hydration energy, with a positive entropy change favoring ion pairing. Thus, ion pairing equilibrium constants and free energies can evidently be more significantly influenced by ion–water interaction than by the intrinsic electrostatic attraction of the oppositely charged counter ions for each other. The latter conclusion is consistent with results obtained for some other aqueous ion pairs^{134,158} and may also contribute to the observed ion pairing between two like-charge guanidinium cations,¹⁷⁶ as well as predictions of a water-shared free energy minimum in the ion pairing potential of mean force between other like-charged ions in water¹⁷⁷ and at an air water interface.¹⁷⁸

REFERENCES

- (1) Skoog, D. A.; Holler, F. J.; Crouch, S. R., *Principles of Instrumental Analysis*; Cengage Learning: 2018.
- (2) Gierszal, K. P.; Davis, J. G.; Hands, M. D.; Wilcox, D. S.; Slipchenko, L. V.; Ben-Amotz, D. π -Hydrogen bonding in liquid water. *J. Phys. Chem. Lett.* **2011**, *2*, 2930–2933.
- (3) Davis, J. G.; Gierszal, K. P.; Wang, P.; Ben-Amotz, D. Water structural transformation at molecular hydrophobic interfaces. *Nature* **2012**, *491*, 582–585.
- (4) De Juan, A.; Tauler, R. Multivariate curve resolution (MCR) from 2000: progress in concepts and applications. *Crit. Rev. Anal. Chem.* **2006**, *36*, 163–176.
- (5) Lawton, W. H.; Sylvestre, E. A. Self modeling curve resolution. *Technometrics* **1971**, *13*, 617–633.
- (6) Ben-Amotz, D. Hydration-shell vibrational spectroscopy. *J. Am. Chem. Soc.* **2019**, *141*, 10569–10580.
- (7) Savitzky, A.; Golay, M. J. Smoothing and differentiation of data by simplified least squares procedures. *Anal. Chem.* **1964**, *36*, 1627–1639.
- (8) Wu, X.; Lu, W.; Streacker, L. M.; Ashbaugh, H. S.; Ben-Amotz, D. Temperature-dependent hydrophobic crossover length scale and water tetrahedral order. *J. Phys. Chem. Lett.* **2018**, *9*, 1012–1017.
- (9) Morawietz, T.; Marsalek, O.; Pattenaude, S. R.; Streacker, L. M.; Ben-Amotz, D.; Markland, T. E. The interplay of structure and dynamics in the Raman spectrum of liquid water over the full frequency and temperature range. *J. Phys. Chem. Lett.* **2018**, *9*, 851–857.
- (10) Du, Q.; Superfine, R.; Freysz, E.; Shen, Y. R. Vibrational spectroscopy of water at the vapor/water interface. *Phys. Rev. Lett.* **1993**, *70*, 2313–2316.
- (11) Moore, F. G.; Richmond, G. L. Integration or segregation: How do molecules behave at oil/water interfaces?. *Acc. Chem. Res.* **2008**, *41*, 739–748.
- (12) Perera, P. N.; Fega, K. R.; Lawrence, C.; Sundstrom, E. J.; Tomlinson-Phillips, J.; Ben-Amotz, D. Observation of water dangling OH bonds around dissolved nonpolar groups. *Proc. Natl. Acad. Sci. U.S.A.* **2009**, *106*, 12230–12234.

- (13) Biedermann, F.; Nau, W. M.; Schneider, H.-J. [The hydrophobic effect revisited—Studies with supramolecular complexes imply high-energy water as a noncovalent driving force.](#) *Angew. Chem.* **2014**, *53*, 11158–11171.
- (14) Cremer, P. S.; Flood, A. H.; Gibb, B. C.; Mobley, D. L. [Collaborative routes to clarifying the murky waters of aqueous supramolecular chemistry.](#) *Nat. Chem.* **2018**, *10*, 8.
- (15) VanEtten, R. L.; Sebastian, J. F.; Clowes, G. A.; Bender, M. L. [Acceleration of phenyl ester cleavage by cycloamyloses. A model for enzymic specificity.](#) *J. Am. Chem. Soc.* **1967**, *89*, 3242–3253.
- (16) Cao, L.; Šekutor, M.; Zavalij, P. Y.; Mlinarić-Majerski, K.; Glaser, R.; Isaacs, L. [Cucurbit\[7\]uril-guest pair with an attomolar dissociation constant.](#) *Angew. Chem.* **2014**, *126*, 1006–1011.
- (17) Nau, W. M.; Florea, M.; Assaf, K. I. [Deep inside cucurbiturils: Physical properties and volumes of their inner cavity determine the hydrophobic driving force for host–guest complexation.](#) *Isr. J. Chem.* **2011**, *51*, 559–577.
- (18) Raffaini, G.; Ganazzoli, F. [Hydration and flexibility of \$\alpha\$ -, \$\beta\$ -, \$\gamma\$ -, and \$\delta\$ -cyclodextrin: A molecular dynamics study.](#) *Chem. Phys.* **2007**, *333*, 128–134.
- (19) Yong, C. W.; Washington, C.; Smith, W. [Structural behaviour of 2-hydroxypropyl- \$\beta\$ -cyclodextrin in water: Molecular dynamics simulation studies.](#) *Pharm. Res.* **2008**, *25*, 1092–1099.
- (20) Lawtrakul, L.; Viernstein, H.; Wolschann, P. [Molecular dynamics simulations of \$\beta\$ -cyclodextrin in aqueous solution.](#) *Int. J. Pharm.* **2003**, *256*, 33–41.
- (21) Betzel, C.; Saenger, W.; Hingerty, B. E.; Brown, G. M. [Topography of cyclodextrin inclusion complexes, part 20. Circular and flip-flop hydrogen bonding in \$\beta\$ -cyclodextrin undecahydrate: A neutron diffraction study.](#) *J. Am. Chem. Soc.* **1984**, *106*, 7545–7557.
- (22) Rasaiah, J. C.; Garde, S.; Hummer, G. [Water in nonpolar confinement: From nanotubes to proteins and beyond.](#) *Annu. Rev. Phys. Chem.* **2008**, *59*, 713–740.
- (23) Ewell, J.; Gibb, B. C.; Rick, S. W. [Water inside a hydrophobic cavitand molecule.](#) *J. Phys. Chem. B* **2008**, *112*, 10272–10279.
- (24) Qvist, J.; Davidovic, M.; Hamelberg, D.; Halle, B. [A dry ligand-binding cavity in a solvated protein.](#) *Proc. Natl. Acad. Sci. U. S. A.* **2008**, *105*, 6296–6301.

- (25) Collins, M. D.; Hummer, G.; Quillin, M. L.; Matthews, B. W.; Gruner, S. M. [Cooperative water filling of a nonpolar protein cavity observed by high-pressure crystallography and simulation](#). *Proc. Natl. Acad. Sci. U. S. A.* **2005**, *102*, 16668–16671.
- (26) Yoshizawa, M.; Kusakawa, T.; Kawano, M.; Ohhara, T.; Tanaka, I.; Kurihara, K.; Niimura, N.; Fujita, M. [Endohedral clusterization of ten water molecules into a “molecular ice” within the hydrophobic pocket of a self-assembled cage](#). *J. Am. Chem. Soc.* **2005**, *127*, 2798–2799.
- (27) Garel, L.; Dutasta, J.-P.; Collet, A. [Complexation of methane and chlorofluorocarbons by cryptophane-A in organic solution](#). *Angew. Chem.* **1993**, *32*, 1169–1171.
- (28) Setny, P.; Baron, R.; Kekenus-Huskey, P. M.; McCammon, J. A.; Dzubiella, J. [Solvent fluctuations in hydrophobic cavity–ligand binding kinetics](#). *Proc. Natl. Acad. Sci. U. S. A.* **2013**, *110*, 1197–1202.
- (29) Tucker, E. E.; Christian, S. D. [Vapor pressure studies of benzene-cyclodextrin inclusion complexes in aqueous solution](#). *J. Am. Chem. Soc.* **1984**, *106*, 1942–1945.
- (30) Trofymchuk, I.; Belyakova, L.; Grebenyuk, A. [Study of complex formation between \$\beta\$ -cyclodextrin and benzene](#). *J. Incl. Phenom. Macrocycl. Chem.* **2011**, *69*, 371–375.
- (31) Perera, P.; Wyche, M.; Loethen, Y.; Ben-Amotz, D. [Solute-induced perturbations of solvent-shell molecules observed using multivariate Raman curve resolution](#). *J. Am. Chem. Soc.* **2008**, *130*, 4576–4577.
- (32) Fourmentin, S.; Ciobanu, A.; Landy, D.; Wenz, G. [Space filling of \$\beta\$ -cyclodextrin and \$\beta\$ -cyclodextrin derivatives by volatile hydrophobic guests](#). *Beilstein J. Org. Chem.* **2013**, *9*, 1185–1191.
- (33) Hirose, K. [A practical guide for the determination of binding constants](#). *J. Incl. Phenom. Macrocycl. Chem.* **2001**, *39*, 193–209.
- (34) Alexander, D. M. [The solubility of benzene in water](#). *J. Phys. Chem.* **1959**, *63*, 1021–1022.
- (35) Arnold, D.; Plank, C.; Erickson, E.; Pike, F. [Solubility of benzene in water](#). *Ind. Eng. Chem. Chem. Eng. Data Series* **1958**, *3*, 253–256.
- (36) Ben-Amotz, D. [Interfacial solvation thermodynamics](#). *J. Phys. Condens. Matter* **2016**, *28*, 414013.
- (37) Wilhelm, E.; Battino, R.; Wilcock, R. J. [Low-pressure solubility of gases in liquid water](#). *Chem. Rev.* **1977**, *77*, 219–262.

- (38) Tretinnikov, O. N.; Ikada, Y. [Dynamic wetting and contact-angle hysteresis of polymer surfaces studies with the modified Wilhelmy balance method](#). *Langmuir* **1994**, *10*, 1606–1614.
- (39) Camerino, E.; Wong, D. M.; Tong, F.; Körber, F.; Gross, A. D.; Islam, R.; Viayna, E.; Mutunga, J. M.; Li, J.; Totrov, M. M.; Bloomquist, J. R.; Carlier, P. R. [Difluoromethyl ketones: Potent inhibitors of wild type and carbamate-insensitive G119S mutant *Anopheles gambiae* acetylcholinesterase](#). *Bioorganic Med. Chem. Lett.* **2015**, *25*, 4405–4411.
- (40) Ye, S.; Loll, B.; Berger, A. A.; Mülow, U.; Alings, C.; Wahl, M. C.; Kokschi, B. [Fluorine teams up with water to restore inhibitor activity to mutant BPTI](#). *Chem. Sci.* **2015**, *6*, 5246–5254.
- (41) Zheng, B. et al. [Potent inhibitors of hepatitis C virus NS3 protease: Employment of a difluoromethyl group as a hydrogen-bond donor](#). *ACS Med. Chem. Lett.* **2018**, *9*, 143–148.
- (42) Berger, A. A.; Völler, J. S.; Budisa, N.; Kokschi, B. [Deciphering the fluorine code—The many hats fluorine wears in a protein environment](#). *Acc. Chem. Res.* **2017**, *50*, 2093–2103.
- (43) Marsh, E. N. G. [Fluorinated proteins: From design and synthesis to structure and stability](#). *Acc. Chem. Res.* **2014**, *47*, 2878–2886.
- (44) Buer, B. C.; Levin, B. J.; Marsh, E. N. G. [Influence of fluorination on the thermodynamics of protein folding](#). *J. Am. Chem. Soc.* **2012**, *134*, 13027–13034.
- (45) Salwiczek, M.; Nyakatura, E. K.; Gerling, U. I. M.; Ye, S.; Kokschi, B. [Fluorinated amino acids: Compatibility with native protein structures and effects on protein–protein interactions](#). *Chem. Soc. Rev.* **2012**, *41*, 2135–2171.
- (46) Giménez, D.; Andreu, C.; del Olmo, M.; Varea, T.; Diaz, D.; Asensio, G. [The introduction of fluorine atoms or trifluoromethyl groups in short cationic peptides enhances their antimicrobial activity](#). *Bioorganic Med. Chem.* **2006**, *14*, 6971–6978.
- (47) Meng, H.; Kumar, K. [Antimicrobial activity and protease stability of peptides containing fluorinated amino acids](#). *J. Am. Chem. Soc.* **2007**, *129*, 15615–15622.
- (48) Robalo, J. R.; Vila Verde, A. [Unexpected trends in the hydrophobicity of fluorinated amino acids reflect competing changes in polarity and conformation](#). *Phys. Chem. Chem. Phys.* **2019**, *21*, 2029–2038.

- (49) Ben-Amotz, D. [Water-mediated hydrophobic interactions](#). *Annu. Rev. Phys. Chem.* **2016**, *67*, 617–638.
- (50) Mondal, S.; Biswas, B.; Nandy, T.; Singh, P. C. [Understanding the role of hydrophobic terminal in the hydrogen bond network of the aqueous mixture of 2,2,2-trifluoroethanol: IR, molecular dynamics, quantum chemical as well as atoms in molecules studies](#). *J. Phys. Chem. B* **2018**, *122*, 6616–6626.
- (51) Bergstrom, P. A.; Lindgren, J. [On the hydration of the trifluoroacetate ion \(\$\text{CF}_3\text{COO}^-\$ \) in aqueous solution](#). *J. Mol. Struct.* **1991**, *245*, 221–229.
- (52) Du, Q.; Freysz, E.; Shen, Y. [Surface vibrational spectroscopic studies of hydrogen-bonding and hydrophobicity](#). *Science* **1994**, *264*, 826–828.
- (53) Tomlinson-Phillips, J.; Davis, J.; Ben-Amotz, D.; Spångberg, D.; Pejov, L.; Hermansson, K. [Structure and dynamics of water dangling OH bonds in hydrophobic hydration shells. Comparison of simulation and experiment](#). *J. Phys. Chem. A* **2011**, *115*, 6177–6183.
- (54) Davis, J. G.; Rankin, B. M.; Gierszal, K. P.; Ben-Amotz, D. [On the cooperative formation of non-hydrogen-bonded water at molecular hydrophobic interfaces](#). *Nat. Chem.* **2013**, *5*, 796–802.
- (55) Ben-Amotz, D. [Hydrophobic ambivalence: Teetering on the edge of randomness](#). *J. Phys. Chem. Lett.* **2015**, *6*, 1696–1701.
- (56) Hsieh, C.-S.; Campen, R. K.; Vila Verde, A. C.; Bolhuis, P.; Nienhuys, H.-K.; Bonn, M. [Ultrafast reorientation of dangling OH groups at the air/water interface](#). *Phys. Rev. Lett.* **2011**, *107*, 116102.
- (57) Tong, Y.; Vila Verde, A.; Campen, R. K. [The free OD at the air/D₂O interface is structurally and dynamically heterogeneous](#). *J. Phys. Chem. B* **2013**, *117*, 11753–11764.
- (58) Stiopkin, I. V.; Weeraman, C.; Pieniazek, P. A.; Shalhout, F. Y.; Skinner, J. L.; Benderskii, A. V. [Hydrogen bonding at the water surface revealed by isotopic dilution spectroscopy](#). *Nature* **2011**, *474*, 192–195.
- (59) Jedlovszky, P. [The hydrogen bonding structure of water in the vicinity of apolar interfaces: A computer simulation](#). *J. Phys.: Condens. Matter* **2004**, *16*, S5389–S5402.
- (60) Stirnemann, G.; Rossky, P. J.; Hynes, J. T.; Laage, D. [Water reorientation, hydrogen-bond dynamics and 2D-IR spectroscopy next to an extended hydrophobic surface](#). *Faraday Discuss.* **2010**, *146*, 263–281.

- (61) Kühne, T. D.; Pascal, T. A.; Kaxiras, E.; Jung, Y. [New insights into the structure of the vapor/water interface from large-scale first-principles simulations.](#) *J. Phys. Chem. Lett.* **2011**, *2*, 105–113.
- (62) Vila Verde, A.; Bolhuis, P. G.; Campen, R. K. [Statics and dynamics of free and hydrogen-bonded OH groups at the air/water interface.](#) *J. Phys. Chem. B* **2012**, *116*, 9467–9481.
- (63) Kessler, J.; Elgabarty, H.; Spura, T.; Karhan, K.; Partovi-Azar, P.; Hassanali, A. A.; Kühne, T. D. [Structure and dynamics of the instantaneous water/vapor interface revisited by path-integral and ab initio molecular dynamics simulations.](#) *J. Phys. Chem. B* **2015**, *119*, 10079–10086.
- (64) Strazdaite, S.; Versluis, J.; Bakker, H. J. [Water orientation at hydrophobic interfaces.](#) *J. Chem. Phys.* **2015**, *143*, 084708.
- (65) Tang, F.; Ohto, T.; Hasegawa, T.; Xie, W. J.; Xu, L.; Bonn, M.; Nagata, Y. [Definition of free O-H groups of water at the air-water interface.](#) *J. Chem. Theory Comput.* **2018**, *14*, 357–364.
- (66) Zukowski, S. R.; Mitev, P. D.; Hermansson, K.; Ben-Amotz, D. [CO₂ hydration shell structure and transformation.](#) *J. Phys. Chem. Lett.* **2017**, *8*, 2971–2975.
- (67) Robalo, J. R.; Mendes de Oliveira, D.; Imhof, P.; Ben-Amotz, D.; Vila Verde, A. [Quantifying how step-wise fluorination tunes local solute hydrophobicity hydration shell thermodynamics and the quantum mechanical contributions of solute–water interactions.](#) *Phys. Chem. Chem. Phys.* **2020**, *22*, 22997–23008.
- (68) Robalo, J. R.; Streacker, L. M.; Mendes de Oliveira, D.; Imhof, P.; Ben-Amotz, D.; Verde, A. V. [Hydrophobic but water-friendly: Favorable water–perfluoromethyl interactions promote hydration shell defects.](#) *J. Am. Chem. Soc.* **2019**, *141*, 15856–15868.
- (69) Gottschalk, H. C. et al. [The furan microsolvation blind challenge for quantum chemical methods: First steps.](#) *J. Chem. Phys.* **2018**, *148*, 14301.
- (70) Wagner, J. P.; Schreiner, P. R. [London dispersion in molecular chemistry – Reconsidering steric effects.](#) *Angew. Chem. Int. Ed.* **2015**, *54*, 12274–12296.
- (71) Mata, R. A.; Suhm, M. A. [Benchmarking quantum chemical methods: Are we heading in the right direction?.](#) *Angew. Chem. Int. Ed.* **2017**, *56*, 11011–11018.
- (72) Pegram, L. M.; Record, M. T. [Thermodynamic origin of Hofmeister ion effects.](#) *J. Phys. Chem. B* **2008**, *112*, 9428–9436.

- (73) Salis, A.; Bilaničová, D.; Ninham, B. W.; Monduzzi, M. [Hofmeister effects in enzymatic activity: Weak and strong electrolyte influences on the activity of *Candida rugosa* lipase](#). *J. Phys. Chem. B* **2007**, *111*, 1149–1156.
- (74) Bilaničová, D.; Salis, A.; Ninham, B. W.; Monduzzi, M. [Specific anion effects on enzymatic activity in nonaqueous media](#). *J. Phys. Chem. B* **2008**, *112*, 12066–12072.
- (75) Abezgauz, L.; Kuperkar, K.; Hassan, P. A.; Ramon, O.; Bahadur, P.; Danino, D. [Effect of Hofmeister anions on micellization and micellar growth of the surfactant cetylpyridinium chloride](#). *J. Colloid Interf. Sci.* **2010**, *342*, 83–92.
- (76) Lin, S.-T.; Lin, C.-S.; Chang, Y.-Y.; Whitten, A. E.; Sokolova, A.; Wu, C.-M.; Ivanov, V. A.; Khokhlov, A. R.; Tung, S.-H. [Effects of alkali cations and halide anions on the self-assembly of phosphatidylcholine in oils](#). *Langmuir* **2016**, *32*, 12166–12174.
- (77) Mortara, L.; Lima, F. d. S.; Cuccovia, I. M.; Nazet, A.; Horinek, D.; Buchner, R.; Chaimovich, H. [Specific ion effects on zwitterionic micelles are independent of interfacial hydration changes](#). *Langmuir* **2018**, *34*, 11049–11057.
- (78) Visser, H. C.; Rudkevich, D. M.; Verboom, W.; de Jong, F.; Reinhoudt, D. N. [Anion carrier mediated membrane transport of phosphate: Selectivity of \$\text{H}_2\text{PO}_4^-\$ over \$\text{Cl}^-\$](#) . *J. Am. Chem. Soc.* **1994**, *116*, 11554–11555.
- (79) Petrache, H. I.; Zemb, T.; Belloni, L.; Parsegian, V. A. [Salt screening and specific ion adsorption determine neutral-lipid membrane interactions](#). *Proc. Natl. Acad. Sci. U. S. A.* **2006**, *103*, 7982.
- (80) He, X.; Ewing, A. G. [Counteranions in the stimulation solution alter the dynamics of exocytosis consistent with the Hofmeister series](#). *J. Am. Chem. Soc.* **2020**, 12591–12595.
- (81) Hofmeister, F. [Zur Lehre von der Wirkung der Salze](#). *Arch. Exp. Pathol. Pharmacol.* **1888**, *25*, 1–30.
- (82) Kunz, W.; Henle, J.; Ninham, B. W. [‘Zur Lehre von der Wirkung der Salze’ \(About the science of the effect of salts\): Franz Hofmeister’s historical papers](#). *Curr. Opin. Colloid Interface Sci.* **2004**, *9*, 19–37.
- (83) Jungwirth, P.; Cremer, P. S. [Beyond Hofmeister](#). *Nat. Chem.* **2014**, *6*, 261–263.
- (84) Gurau, M. C.; Lim, S.-M.; Castellana, E. T.; Albertorio, F.; Kataoka, S.; Cremer, P. S. [On the mechanism of the Hofmeister effect](#). *J. Am. Chem. Soc.* **2004**, *126*, 10522–10523.

- (85) Zhang, Y.; Cremer, P. S. [The inverse and direct Hofmeister series for lysozyme.](#) *Proc. Natl. Acad. Sci. U. S. A.* **2009**, *106*, 15249–15253.
- (86) Zhang, Y.; Furyk, S.; Bergbreiter, D. E.; Cremer, P. S. [Specific ion effects on the water solubility of macromolecules: PNIPAM and the Hofmeister series.](#) *J. Am. Chem. Soc.* **2005**, *127*, 14505–14510.
- (87) Long, J. A.; Rankin, B. M.; Ben-Amotz, D. [Micelle structure and hydrophobic hydration.](#) *J. Am. Chem. Soc.* **2015**, *137*, 10809–10815.
- (88) Mochizuki, K.; Pattenau, S. R.; Ben-Amotz, D. [Influence of cononsolvency on the aggregation of tertiary butyl alcohol in methanol-water mixtures.](#) *J. Am. Chem. Soc.* **2016**, *138*, 9045–9048.
- (89) Wu, X.; Lu, W.; Streacker, L. M.; Ashbaugh, H. S.; Ben-Amotz, D. [Methane hydration-shell structure and fragility.](#) *Angew. Chem. Int. Ed.* **2018**, *57*, 15133–15137.
- (90) Rankin, B. M.; Hands, M. D.; Wilcox, D. S.; Fega, K. R.; Slipchenko, L. V.; Ben-Amotz, D. [Interactions between halide anions and a molecular hydrophobic interface.](#) *Faraday Discuss.* **2013**, *160*, 255–270.
- (91) Mondal, J.; Halverson, D.; Li, I. T.; Stirnemann, G.; Walker, G. C.; Berne, B. J. [How osmolytes influence hydrophobic polymer conformations: A unified view from experiment and theory.](#) *Proc. Natl. Acad. Sci. U. S. A.* **2015**, *112*, 9270–9275.
- (92) Wyman Jr, J. In *Advances in protein chemistry*; Elsevier: 1964; Vol. 19, pp 223–286.
- (93) Tanford, C. [Extension of the theory of linked functions to incorporate the effects of protein hydration.](#) *J. Mol. Biol.* **1969**, *39*, 539–544.
- (94) Bruce, E. E.; Okur, H. I.; Stegmaier, S.; Drexler, C. I.; Rogers, B. A.; van der Vegt, N. F. A.; Roke, S.; Cremer, P. S. [Molecular mechanism for the interactions of Hofmeister cations with macromolecules in aqueous Solution.](#) *J. Am. Chem. Soc.* **2020**, *142*, 19094–19100.
- (95) Ganguly, P.; Polák, J.; van der Vegt, N. F. A.; Heyda, J.; Shea, J.-E. [Protein stability in TMAO and mixed urea-TMAO solutions.](#) *J. Phys. Chem. B* **2020**, *124*, 6181–6197.
- (96) Francisco, O. A.; Glor, H. M.; Khajepour, M. [Salt effects on hydrophobic solvation: Is the observed salt specificity the result of excluded volume effects or water mediated ion-hydrophobe association?.](#) *ChemPhysChem* **2020**, 484–493.
- (97) Ray, A.; Nemethy, G. [Effects of ionic protein denaturants on micelle formation by nonionic detergents.](#) *J. Am. Chem. Soc.* **1971**, *93*, 6787–6793.

- (98) Koroleva, S. V.; Korchak, P.; Victorov, A. I. [Molecular thermodynamic modeling of the specific effect of salt on the aggregation of nonionic surfactants](#). *J. Chem. Eng. Data* **2020**, *65*, 987–992.
- (99) Ben-Amotz, D., *Understanding Physical Chemistry*; John Wiley and Sons: New York, 2014.
- (100) Israelachvili, J. N., *Intermolecular and Surface Forces*, 2nd; Academic Press: San Diego, 1991.
- (101) Hajji, S. M.; Errahmani, M. B.; Coudert, R.; Durand, R. R.; Cao, A.; Taillandier, E. [A comparative study of 1,2-hexanediol and 1,2,3-octanetriol in aqueous solutions by different physical techniques](#). *J. Phys. Chem.* **1989**, *93*, 4819–4824.
- (102) Mendes de Oliveira, D.; Ben-Amotz, D. [Cavity hydration and competitive binding in methylated \$\beta\$ -cyclodextrin](#). *J. Phys. Chem. Lett.* **2019**, *10*, 2802–2805.
- (103) Mendes de Oliveira, D.; Zukowski, S. R.; Palivec, V.; Hénin, J.; Seara, H. M.; Ben-Amotz, D.; Jungwirth, P.; Duboué-Dijon, E. [Binding of divalent cations to acetate: Molecular simulations guided by Raman spectroscopy](#). *Phys. Chem. Chem. Phys.* **2020**, *22*, 24014–24027.
- (104) Wilcox, D. S.; Rankin, B. M.; Ben-Amotz, D. [Distinguishing aggregation from random mixing in aqueous t-butyl alcohol solutions](#). *Faraday Discuss.* **2013**, *167*, 177–190.
- (105) Rankin, B. M.; Ben-Amotz, D.; van der Post, S. T.; Bakker, H. J. [Contacts between alcohols in water are random rather than hydrophobic](#). *J. Phys. Chem. Lett.* **2015**, *6*, 688–692.
- (106) Bredt, A. J.; Ben-Amotz, D. [Influence of crowding on hydrophobic hydration-shell structure](#). *Phys. Chem. Chem. Phys.* **2020**, *22*, 11724–11730.
- (107) Brini, M.; Ottolini, D.; Calì, T.; Carafoli, E. In *Interrelations between essential metal ions and human diseases*, Sigel, A., Sigel, H., Sigel, R. K. O., Eds.; Springer Netherlands: Dordrecht, 2013, pp 81–137.
- (108) Clapham, D. E. [Calcium signaling](#). *Cell* **2007**, *131*, 1047–1058.
- (109) Yamanaka, R.; Shindo, Y.; Oka, K. [Magnesium is a key player in neuronal maturation and neuropathology](#). *Int. J. Mol. Sci.* **2019**, *20*, 3439.
- (110) Romani, A. M. In *Interrelations between essential metal ions and human diseases*; Springer: 2013, pp 49–79.

- (111) De Baaij, J. H. F.; Hoenderop, J. G. J.; Bindels, R. J. [Magnesium in man: Implications for health and disease](#). *Physiol. Rev.* **2015**, *95*, 1–46.
- (112) Coleman, J. E. [Zinc proteins: Enzymes storage proteins transcription factors and replication proteins](#). *Annu. Rev. Biochem.* **1992**, *61*, 897–946.
- (113) Frassinetti, S.; Bronzetti, G. L.; Caltavuturo, L.; Cini, M.; Della Croce, C. [The role of zinc in life: A review](#). *J. Environ. Pathol., Toxicol. Oncol.* **2006**, *25*.
- (114) Gifford, J. L.; Walsh, M. P.; Vogel, H. J. [Structures and metal-ion-binding properties of the \$\text{Ca}^{2+}\$ -binding helix-loop-helix EF-hand motifs](#). *Biochem. J.* **2007**, *405*, 199–221.
- (115) Klug, A.; Schwabe, J. W. R. [Zinc fingers](#). *FASEB J.* **1995**, *9*, 597–604.
- (116) Hsiao, C.; Williams, L. D. [A recurrent magnesium-binding motif provides a framework for the ribosomal peptidyl transferase center](#). *Nucleic Acids Res.* **2009**, *37*, 3134–3142.
- (117) Mason, P. E.; Jungwirth, P.; Duboué-Dijon, E. [Quantifying the strength of a salt bridge by neutron scattering and molecular dynamics](#). *J. Phys. Chem. Lett.* **2019**, *10*, 3254–3259.
- (118) Martell, A. E.; Smith, R. M., *Other organic ligands*; Critical stability constants, Vol. 3; Springer US: New York., 1977.
- (119) Bunting, J. W.; Thong, K. M. [Stability constants for some 1:1 metal-carboxylate complexes](#). *Can. J. Chem.* **1970**, *48*, 1654–1656.
- (120) Stumpff, F.; McGuigan, J. A. [Measuring \$\text{Ca}^{2+}\$ binding to short chain fatty acids and gluconate with a \$\text{Ca}^{2+}\$ electrode: Role of the reference electrode](#). *Anal. Biochem.* **2014**, *459*, 46–52.
- (121) Bretti, C.; Majlesi, K.; De Stefano, C.; Sammartano, S. [Thermodynamic study on the protonation and complexation of GLDA with \$\text{Ca}^{2+}\$ and \$\text{Mg}^{2+}\$ at different ionic strengths and ionic media at 298.15 K](#). *J. Chem. Eng. Data* **2016**, *61*, 1895–1903.
- (122) McGuigan, J. A. S.; Kay, J. W.; Elder, H. Y. [Ionised concentrations in calcium and magnesium buffers: Standards and precise measurement are mandatory](#). *Prog. Biophys. Mol. Biol.* **2016**, *121*, 195–211.
- (123) Emara, M. M.; Farid, N. A.; Wasfi, A. [Thermodynamics of ionic association in aqueous solutions of Ca and Mg organic salts using ion-selective electrode technique – I. Formates acetates propionates and butyrates](#). *Electrochim. Acta* **1981**, *26*, 1705–1708.

- (124) Wallace, M.; Hicks, T.; Khimyak, Y. Z.; Angulo, J. [Self-correcting method for the measurement of free calcium and magnesium concentrations by \$^1\text{H}\$ NMR](#). *Anal. Chem.* **2019**, *91*, 14442–14450.
- (125) Tackett, J. E. [FT-IR characterization of metal acetates in aqueous solution](#). *Appl. Spectrosc.* **1989**, *43*, 483–489.
- (126) Quilès, F.; Burneau, A. [Infrared and Raman spectra of alkaline-earth and copper\(II\) acetates in aqueous solutions](#). *Vib. Spectrosc.* **1998**, *16*, 105–117.
- (127) Rudolph, W. W.; Irmer, G. [A Raman spectroscopic study of aqueous \$\text{La}\(\text{CH}_3\text{CO}_2\)_3\$ solutions and \$\text{La}\(\text{CH}_3\text{CO}_2\)_3 \cdot 1.5 \text{H}_2\text{O}\$ cr.](#) *J. Solution Chem.* **2017**, *46*, 190–214.
- (128) Tang, C. Y.; Huang, Z.; Allen, H. C. [Binding of \$\text{Mg}^{2+}\$ and \$\text{Ca}^{2+}\$ to palmitic acid and deprotonation of the COOH headgroup studied by vibrational sum frequency generation spectroscopy](#). *J. Phys. Chem. B* **2010**, *114*, 17068–17076.
- (129) Denton, J. K.; Kelleher, P. J.; Johnson, M. A.; Baer, M. D.; Kathmann, S. M.; Mundy, C. J.; Rudd, B. A. W.; Allen, H. C.; Choi, T. H.; Jordan, K. D. [Molecular-level origin of the carboxylate head group response to divalent metal ion complexation at the air–water interface](#). *Proc. Natl. Acad. Sci. U. S. A.* **2019**, *116*, 14874–14880.
- (130) Wahab, A.; Mahiuddin, S.; Hefter, G.; Kunz, W.; Minofar, B.; Jungwirth, P. [Ultrasonic velocities, densities, viscosities, electrical conductivities, Raman spectra, and molecular dynamics simulations of aqueous solutions of \$\text{Mg}\(\text{OAc}\)_2\$ and \$\text{Mg}\(\text{NO}_3\)_2\$: Hofmeister effects and ion pair formation](#). *J. Phys. Chem. B* **2005**, *109*, 24108–24120.
- (131) Mehandzhiyski, A. Y.; Riccardi, E.; van Erp, T. S.; Trinh, T. T.; Grimes, B. A. [Ab initio molecular dynamics study on the interactions between carboxylate ions and metal ions in water](#). *J. Phys. Chem. B* **2015**, *119*, 10710–10719.
- (132) Martinek, T.; Duboué-Dijon, E.; Timr, Š.; Mason, P. E.; Baxová, K.; Fischer, H. E.; Schmidt, B.; Pluhařová, E.; Jungwirth, P. [Calcium ions in aqueous solutions: Accurate force field description aided by ab initio molecular dynamics and neutron scattering](#). *J. Chem. Phys.* **2018**, *148*, 222813.
- (133) Duboué-Dijon, E.; Mason, P. E.; Fischer, H. E.; Jungwirth, P. [Hydration and ion pairing in aqueous \$\text{Mg}^{2+}\$ and \$\text{Zn}^{2+}\$ solutions: Force-field description aided by neutron scattering experiments and ab initio molecular dynamics simulations](#). *J. Phys. Chem. B* **2017**, *122*, 3296–3306.
- (134) Marcus, Y.; Hefter, G. [Ion pairing](#). *Chem. Rev.* **2006**, *106*, 4585–4621.

- (135) Caminiti, R.; Cucca, P.; Monduzzi, M.; Saba, G.; Crisponi, G. [Divalent metal–acetate complexes in concentrated aqueous solutions. An x-ray diffraction and NMR spectroscopy study.](#) *J. Chem. Phys.* **1984**, *81*, 543–551.
- (136) Dudev, T.; Lim, C. [Principles governing Mg, Ca, and Zn binding and selectivity in proteins.](#) *Chem. Rev.* **2003**, *103*, 773–788.
- (137) Dudev, T.; Lim, C. [Effect of carboxylate–binding mode on metal binding/selectivity and function in proteins.](#) *Acc. Chem. Res.* **2007**, *40*, 85–93.
- (138) Ryde, U. [Carboxylate binding modes in zinc proteins: A theoretical study.](#) *Biophys. J.* **1999**, *77*, 2777–2787.
- (139) Paterová, J.; Heyda, J.; Jungwirth, P.; Shaffer, C. J.; Révész, Á.; Zins, E. L.; Schröder, D. [Microhydration of the magnesium\(II\) acetate cation in the gas phase.](#) *J. Phys. Chem. A* **2011**, *115*, 6813–6819.
- (140) Semmler, J.; Irish, D. E.; Ozeki, T. [Vibrational spectral studies of solutions at elevated temperatures and pressures. 12. Magnesium acetate.](#) *Geochim. Cosmochim. Acta* **1990**, *54*, 947–954.
- (141) Wang, L.-Y.; Zhang, Y.-H.; Zhao, L.-J. [Raman spectroscopic studies on single super-saturated droplets of sodium and magnesium acetate.](#) *J. Phys. Chem. A* **2005**, *109*, 609–614.
- (142) Einspahr, H.; Bugg, C. E. [The geometry of calcium carboxylate interactions in crystalline complexes.](#) *Acta Crystallogr., Sect. B: Struct. Crystallogr. Cryst. Chem.* **1981**, *37*, 1044–1052.
- (143) Yang, M. M.; Crerar, D. A.; Irish, D. E. [A Raman spectroscopic study of lead and zinc acetate complexes in hydrothermal solutions.](#) *Geochim. Cosmochim. Acta* **1989**, *53*, 319–326.
- (144) Katz, A. K.; Glusker, J. P.; Markham, G. D.; Bock, C. W. [Deprotonation of water in the presence of carboxylate and magnesium ions.](#) *J. Phys. Chem. B* **1998**, *102*, 6342–6350.
- (145) Dudev, T.; Lim, C. [Monodentate versus bidentate carboxylate binding in magnesium and calcium proteins: What are the basic principles?.](#) *J. Phys. Chem. B* **2004**, *108*, 4546–4557.
- (146) Humphrey, W.; Dalke, A.; Schulten, K. [VMD: Visual molecular dynamics.](#) *J. Mol. Graphics* **1996**, *14*, 33–38.

- (147) Perera, P. N.; Browder, B.; Ben-Amotz, D. [Perturbations of water by alkali halide ions measured using multivariate Raman curve resolution](#). *J. Phys. Chem. B* **2009**, *113*, 1805–1809.
- (148) Davies, C. W. [397. The extent of dissociation of salts in water. Part VIII. An equation for the mean ionic activity coefficient of an electrolyte in water and a revision of the dissociation constants of some sulphates](#). *J. Chem. Soc.* **1938**, 2093–2098.
- (149) Sun, M. S.; Harriss, D. K.; Magnuson, V. R. [Activity corrections for ionic equilibria in aqueous solutions](#). *Can. J. Chem.* **1980**, *58*, 1253–1257.
- (150) Davis, J. G.; Zukowski, S. R.; Rankin, B. M.; Ben-Amotz, D. [Influence of a neighboring charged group on hydrophobic hydration shell structure](#). *J. Phys. Chem. B* **2015**, *119*, 9417–9422.
- (151) Quilès, F.; Burneau, A.; Gross, N. [Vibrational spectroscopic study of the complexation of mercury\(II\) by substituted acetates in aqueous solutions](#). *Appl. Spectrosc.* **1999**, *53*, 1061–1070.
- (152) Uejio, J. S.; Schwartz, C. P.; Duffin, A. M.; Drisdell, W. S.; Cohen, R. C.; Saykally, R. J. [Characterization of selective binding of alkali cations with carboxylate by x-ray absorption spectroscopy of liquid microjets](#). *Proc. Natl. Acad. Sci. U. S. A.* **2008**, *105*, 6809–6812.
- (153) Atkinson, G.; Emara, M. M.; Fernandez-Prini, R. [Ultrasonic absorption in aqueous solutions of calcium acetate and other bivalent metal acetates](#). *J. Phys. Chem.* **1974**, *78*, 1913–1917.
- (154) Shannon, R. [Revised effective ionic radii and systematic studies of interatomic distances in halides and chalcogenides](#). *Acta Crystallogr., Sect. A* **1976**, *32*, 751–767.
- (155) Shannon, R. D.; Fischer, R. X. [Empirical electronic polarizabilities of ions for the prediction and interpretation of refractive indices: Oxides and oxysalts](#). *Am. Mineral.* **2016**, *101*, 2288–2300.
- (156) Linstrom, P. [NIST Chemistry WebBook, NIST Standard Reference Database 69](#), 1997.
- (157) Drexler, C. I.; Miller, T. C.; Rogers, B. A.; Li, Y. C.; Daly Jr., C. A.; Yang, T.; Corcelli, S. A.; Cremer, P. S. [Counter cations affect transport in aqueous hydroxide solutions with ion specificity](#). *J. Am. Chem. Soc.* **2019**, *141*, 6930–6936.

- (158) Gimblett, F. G. R.; Monk, C. B. [E.M.F. studies of electrolytic dissociation. Part 7 — Some alkali and alkaline earth metal hydroxides in water.](#) *Trans. Faraday Soc.* **1954**, *50*, 965–972.
- (159) Corti, H.; Crovetto, R.; Fernández-Prini, R. [Aqueous solutions of lithium hydroxide at various temperatures: Conductivity and activity coefficients.](#) *J. Solution Chem.* **1979**, *8*, 897–908.
- (160) Corti, H. R.; Prini, R. F.; Svarc, F. [Densities and partial molar volumes of aqueous solutions of lithium sodium and potassium hydroxides up to 250°C.](#) *J. Solution Chem.* **1990**, *19*, 793–809.
- (161) Nasirzadeh, K.; Neueder, R.; Kunz, W. [Vapor pressures and osmotic coefficients of aqueous LiOH solutions at temperatures ranging from 298.15 to 363.15 K.](#) *Ind. Eng. Chem. Res.* **2005**, *44*, 3807–3814.
- (162) Megyes, T.; Bálint, S.; Grósz, T.; Radnai, T.; Bakó, I.; Sipos, P. [The structure of aqueous sodium hydroxide solutions: A combined solution x-ray diffraction and simulation study.](#) *J. Chem. Phys.* **2008**, *128*, 044501.
- (163) Hellström, M.; Behler, J. [Concentration-dependent proton transfer mechanisms in aqueous NaOH solutions: From acceptor-driven to donor-driven and back.](#) *J. Phys. Chem. Lett.* **2016**, *7*, 3302–3306.
- (164) Shao, Y.; Hellström, M.; Yllö, A.; Mindemark, J.; Hermansson, K.; Behler, J.; Zhang, C. [Temperature effects on the ionic conductivity in concentrated alkaline electrolyte solutions.](#) *Phys. Chem. Chem. Phys.* **2020**, 10426–10430.
- (165) Moskovits, M.; Michaelian, K. H. [Alkali hydroxide ion pairs. A Raman study.](#) *J. Am. Chem. Soc.* **1980**, *102*, 2209–2215.
- (166) Van der Vegt, N. F. A.; Haldrup, K.; Roke, S.; Zheng, J. R.; Lund, M.; Bakker, H. J. [Water-mediated ion pairing: Occurrence and relevance.](#) *Chem. Rev.* **2016**, *116*, 7626–7641.
- (167) Tielrooij, K. J.; Garcia-Araez, N.; Bonn, M.; Bakker, H. J. [Cooperativity in ion hydration.](#) *Science* **2010**, *328*, 1006–1009.
- (168) Okur, H. I.; Hladilkova, J.; Rembert, K. B.; Cho, Y.; Heyda, J.; Dzubiella, J.; Cremer, P. S.; Jungwirth, P. [Beyond the Hofmeister series: Ion-specific effects on proteins and their biological functions.](#) *J. Phys. Chem. B* **2017**, *121*, 1997–2014.

- (169) Baer, M. D.; Fulton, J. L.; Balasubramanian, M.; Schenter, G. K.; Mundy, C. J. [Persistent ion pairing in aqueous hydrochloric acid](#). *J. Phys. Chem. B* **2014**, *118*, 7211–7220.
- (170) Roy, S.; Patra, A.; Saha, S.; Palit, D. K.; Mondal, J. A. [Restructuring of hydration shell water due to solvent-shared ion pairing SSIP: A case study of aqueous MgCl₂ and LaCl₃ solutions](#). *J. Phys. Chem. B* **2020**, *124*, 8141–8148.
- (171) Agmon, N.; Bakker, H. J.; Campen, R. K.; Henchman, R. H.; Pohl, P.; Roke, S.; Thamer, M.; Hassanali, A. [Protons and hydroxide ions in aqueous systems](#). *Chem. Rev.* **2016**, *116*, 7642–7672.
- (172) Hermansson, K.; Bopp, P. A.; Spångberg, D.; Pejov, L.; Bakó, I.; Mitev, P. D. [The vibrating hydroxide ion in water](#). *Chem. Phys. Lett.* **2011**, *514*, 1–15.
- (173) Galib, M.; Baer, M. D.; Skinner, L. B.; Mundy, C. J.; Huthwelker, T.; Schenter, G. K.; Benmore, C. J.; Govind, N.; Fulton, J. L. [Revisiting the hydration structure of aqueous Na⁺](#). *J. Chem. Phys.* **2017**, *146*, 084504.
- (174) Kebede, G. G.; Mitev, P. D.; Broqvist, P.; Kullgren, J.; Hermansson, K. [Hydrogen-bond relations for surface OH species](#). *J. Phys. Chem. C* **2018**, *122*, 4849–4858.
- (175) Mandal, A.; Tokmakoff, A. [Vibrational dynamics of aqueous hydroxide solutions probed using broadband 2DIR spectroscopy](#). *J. Chem. Phys.* **2015**, *143*, 194501.
- (176) Vazdar, M.; Heyda, J.; Mason, P. E.; Tesei, G.; Allolio, C.; Lund, M.; Jungwirth, P. [Arginine “magic”: Guanidinium like-charge ion pairing from aqueous salts to cell penetrating peptides](#). *Acc. Chem. Res.* **2018**, *51*, 1455–1464.
- (177) Pratt, L. R.; Hummer, G.; Garcia, A. E. [Ion pair potentials-of-mean-force in water](#). *Biophys. Chem.* **1994**, *51*, 147–165.
- (178) Venkateshwaran, V.; Vembanur, S.; Garde, S. [Water-mediated ion-ion interactions are enhanced at the water vapor-liquid interface](#). *Proc. Natl. Acad. Sci. U. S. A.* **2014**, *111*, 8729–8734.
- (179) Martínez, L.; Andrade, R.; Birgin, E. G.; Martínez, J. M. [PACKMOL: A package for building initial configurations for molecular dynamics simulations](#). *J. Comput. Chem.* **2009**, *30*, 2157–2164.
- (180) Hutter, J.; Iannuzzi, M.; Schiffmann, F.; VandeVondele, J. [CP2K: Atomistic simulations of condensed matter systems](#). *Wiley Interdiscip. Rev. Comput. Mol. Sci.* **2014**, *4*, 15–25.

- (181) Daly, C. A.; Streacker, L. M.; Sun, Y.; Pattenaude, S. R.; Hassanali, A. A.; Petersen, P. B.; Corcelli, S. A.; Ben-Amotz, D. [Decomposition of the experimental Raman and infrared spectra of acidic water into proton special pair and counterion contributions](#). *J. Phys. Chem. Lett.* **2017**, *8*, 5246–5252.
- (182) Hassanali, A.; Giberti, F.; Cuny, J.; Kühne, T. D.; Parrinello, M. [Proton transfer through the water gossamer](#). *Proc. Natl. Acad. Sci. U. S. A.* **2013**, *110*, 13723.
- (183) VandeVondele, J.; Krack, M.; Mohamed, F.; Parrinello, M.; Chassaing, T.; Hutter, J. [Quickstep: Fast and accurate density functional calculations using a mixed Gaussian and plane waves approach](#). *Comput. Phys. Commun.* **2005**, *167*, 103–128.
- (184) Goedecker, S.; Teter, M.; Hutter, J. [Separable dual-space Gaussian pseudopotentials](#). *Phys. Rev. B* **1996**, *54*, 1703–1710.
- (185) Hartwigsen, C.; Goedecker, S.; Hutter, J. [Relativistic separable dual-space Gaussian pseudopotentials from H to Rn](#). *Phys. Rev. B* **1998**, *58*, 3641–3662.
- (186) Krack, M. [Pseudopotentials for H to Kr optimized for gradient-corrected exchange-correlation functionals](#). *Theor. Chem. Acc.* **2005**, *114*, 145–152.
- (187) Becke, A. D. [Density-functional exchange-energy approximation with correct asymptotic behavior](#). *Phys. Rev. A* **1988**, *38*, 3098–3100.
- (188) Lee, C.; Yang, W.; Parr, R. G. [Development of the Colle-Salvetti correlation-energy formula into a functional of the electron density](#). *Phys. Rev. B* **1988**, *37*, 785–789.
- (189) Grimme, S.; Antony, J.; Ehrlich, S.; Krieg, H. [A consistent and accurate ab initio parametrization of density functional dispersion correction DFT-D for the 94 elements H-Pu](#). *J. Chem. Phys.* **2010**, *132*, 154104.
- (190) Daly, C. A.; Brinzer, T.; Allison, C.; Garrett-Roe, S.; Corcelli, S. A. [Enthalpic driving force for the selective absorption of CO₂ by an ionic liquid](#). *J. Phys. Chem. Lett.* **2018**, *9*, 1393–1397.
- (191) Fega, K. R.; Wilcox, A. S.; Ben-Amotz, D. [Application of Raman multivariate curve resolution to solvation-shell spectroscopy](#). *Appl. Spectrosc.* **2012**, *66*, 282–288.
- (192) Ben-Naim, A., *Solvation thermodynamics*; Plenum Press: New York, 1987.
- (193) Ben-Amotz, D.; Underwood, R. [Unraveling water’s entropic mysteries: A unified view of nonpolar polar and ionic hydration](#). *Acc. Chem. Res.* **2008**, *41*, 957–967.

- (194) Mendes de Oliveira, D.; Zukowski, S. R.; Palivec, V.; Hénin, J.; Martinez-Seara, H.; Ben-Amotz, D.; Jungwirth, P.; Duboué-Dijon, E. [Binding of biologically relevant divalent cations to aqueous acetate: Molecular simulations guided by Raman spectroscopy.](#) *Phys. Chem. Chem. Phys.* **2020**, *22*, 24014–24027.
- (195) Mondal, S.; Biswas, B.; Sarkar, S.; Singh, P. C. [A combined molecular dynamics simulation atoms in molecule analysis and IR study on the biologically important bulk fluorinated ethanols to understand the role of weak interactions in their cluster formation and hydrogen bond network.](#) *J. Mol. Liq.* **2017**, *240*, 708–716.
- (196) Perttilä, M. [Vibrational spectra and normal coordinate analysis of 2,2,2-trichloroethanol and 2,2,2-trifluoroethanol.](#) *Spectrochim. Acta A* **1979**, *35*, 585–592.
- (197) Koroleva, S. V.; Victorov, A. I. [Modeling of the effects of ion specificity on the onset and growth of ionic micelles in a solution of simple salts.](#) *Langmuir* **2014**, *30*, 3387–3396.
- (198) Long, F. A.; McDevit, W. F. [Activity coefficients of nonelectrolyte solutes in aqueous salt solutions.](#) *Chem. Rev.* **1952**, *51*, 119–169.

A. SUPPLEMENTARY METHODS AND EXPERIMENTAL RESULTS FOR HOST-GUEST BINDING STUDIES

This appendix provides derivations of important equations used to obtain results relevant to the study of host-guest binding systems using Raman-MCR. Although most results are presented for the benzene/Me- β -CD system, the equations are of general use.

A.1 Total least squares regression

Let X be the spectrum of a solution of some mixture of host and/or guest molecules, represented as a $1 \times n$ vector (where n is the number of frequency values in the spectrum). If the spectra of the unbound and bound species are known, then total least squares (TLS) can be used to decompose X into unbound and bound components. Specifically, let P be a $2 \times n$ matrix of pure components (unbound and bound) spectra and b be a 1×2 vector that contains the (as yet unknown) spectral weights of the two components in X , such that

$$X = bP \tag{A.1}$$

The coefficients b may be determined using TLS by multiplying both sides of Equation A.1 by the Moore–Penrose inverse of P , as follows

$$b = XP^T(PP^T)^{-1} \tag{A.2}$$

In Equation A.2, P^T represents the transpose of matrix P . Note that if the spectra X and the two component spectra in P are all normalized to unit area (over the frequency range of the band of interest), then the elements of the vector b are the spectral weights of the unbound and bound components.

A.2 Determination of the host–guest binding constant and Raman cross section change

A total least squares (TLS) fit of the C–D band obtained from a mixture of benzene-d₆ and Me- β -CD to a linear combination of the unbound and bound benzene-d₆ C–D bands can be used to retrieve the relative areas of unbound and bound benzene-d₆ in the mixture. More specifically, when this fit is performed with all the C–D bands normalized to unit area, the results yield the relative spectral weight of the unbound and bound components in the mixture C–D band. Converting these spectral weights to the corresponding component concentrations requires knowing the relative Raman cross sections of the unbound and bound benzene-d₆ C–D stretch band. In the present case, the unbound benzene cross section is implicitly known (e.g., from measuring a saturated solution of benzene), and thus the concentration of unbound benzene-d₆ in the mixture can be determined from the TLS fit results. If the mixtures used to perform these fits are all constrained to have a known total benzene-d₆ concentration (e.g., 10 mM in our experiments), then mass balance (combined with the measured spectrum of a saturated aqueous benzene solution) can be used to obtain the concentration of bound benzene using the following equations

$$c_{\text{unbound}} = f_{\text{unbound}} \left(\frac{A_{\text{mix}}}{A_{\text{sat}}} \right) c_{\text{sat}} \quad (\text{A.3})$$

$$c_{\text{bound}} = c_{\text{total}} - c_{\text{unbound}} \quad (\text{A.4})$$

where A_{sat} and c_{sat} are the area and concentration (22.9 mM) of a saturated solution of benzene, respectively; A_{mix} is the area of a solution with a known total benzene concentration; and f_{unbound} is the TLS fraction (spectral weight) of the unbound benzene in the mixture. Thus, the ratio of the C–D stretch Raman cross sections of the bound and unbound benzene may be obtained as follows (where subscripts indicate the area and concentration of unbound and bound benzene obtained as explained above):

$$\frac{\sigma_{\text{bound}}}{\sigma_{\text{unbound}}} = \frac{A_{\text{bound}}/c_{\text{bound}}}{A_{\text{unbound}}/c_{\text{unbound}}} \approx 1.4 \pm 0.1 \quad (\text{A.5})$$

The above considerations may also be used to quantify the host-guest binding equilibrium constant. The formation of a 1:1 host/guest complex is usually represented by a complexation reaction of the form



with an equilibrium constant given by

$$K = \frac{[\text{HG}]}{[\text{H}][\text{G}]} \quad (\text{A.7})$$

Thus, the measured fraction of bound benzene-d₆ (guest) along with the total concentrations of benzene-d₆ and Me- β -CD (host) may be used to obtain K , as illustrated in Figure 2.2 in Chapter 2. Alternatively, given the Raman cross section ratio in Equation A.5, one may determine K from measurements of aqueous solutions in equilibrium with a liquid benzene-d₆ phase. In this case, the unbound benzene concentration is pinned to its saturated concentration and the measured C–D band of the aqueous solution can be used to obtain the concentration of bound benzene-d₆ and the ratio of the complexed and unbound host concentrations.

The above equations do not include the water molecules in the unbound host which are displaced upon binding the guest. This is equivalent to assuming that the concentration of pure water is expressed in mole fraction units. In order to directly consider competitive binding of water and benzene, it is more convenient to use the same units for all concentrations, and thus express the above equilibrium and equilibrium constant as follows:



$$K' = \frac{[\text{HG}][\text{H}_2\text{O}]^n}{[\text{H}(\text{H}_2\text{O})_n][\text{G}]} \quad (\text{A.9})$$

Note that $K' = K[\text{H}_2\text{O}]^n$, where n is the number of water molecules bound in the cavity of the unbound host, and thus K and K' have substantially different numerical values. For the complexation of benzene with Me- β -CD, our results indicate that $K \sim 101$ (1/M) and thus $K' = K[\text{H}_2\text{O}]^n$ (M^{n-1}) is estimated to be $5 \times 10^{10} \leq K' \leq 3 \times 10^{12}$, since $5 \leq n \leq 6$ is

the average number of cavity-bound water molecules in the unbound host, as determined from our Raman-MCR measurements (obtained as further described in the next section). Thus, the equilibrium constant K' provides a direct measure of the competitive binding of water and benzene in the host cavity, as Equation A.9 indicates that the ratio of benzene-complexed to water-filled host cavities would be equal to K' if the concentrations of unbound water and benzene were both (hypothetically) scaled to a value of 1 M.

A.3 Determination of the number of water molecules in the Me- β -CD cavity

The number of water molecules (n) in the Me- β -CD cavity was evaluated using Equation A.10:

$$n = \frac{55.4}{[\text{HG}]} \frac{A_{\text{w}} - A_{\text{b}}}{A_{\text{water}}} \quad (\text{A.10})$$

where $[\text{HG}]$ is estimated using the determined binding constant K above; 55.4 (M) is the concentration of pure water at 20 °C; and A_{w} , A_{b} and A_{water} represent the areas under the OH stretch band for the water-filled Me- β -CD, benzene-filled Me- β -CD, and pure water (as depicted in Figure 2.1c in Chapter 2), respectively. The A_{w} area was scaled to reflect the same concentration as that of benzene-filled Me- β -CD. Thus, given that our results indicate that $92 \leq K \leq 110$, Equation A.10 implies that $5 \leq n \leq 6$. Note that this estimated range of the number of cavity-bound water molecules assumes that there is no binding-induced change in the Raman cross section of water.

B. SUPPORTING INFORMATION FOR DANGLING HYDROXY FORMATION IN AQUEOUS SOLUTIONS OF FLUORINATED ETHANOL

This Appendix provides additional experimental results to supplement discussions in Chapter 3.

B.1 Solute-correlated hydration-shell spectrum of ethanol

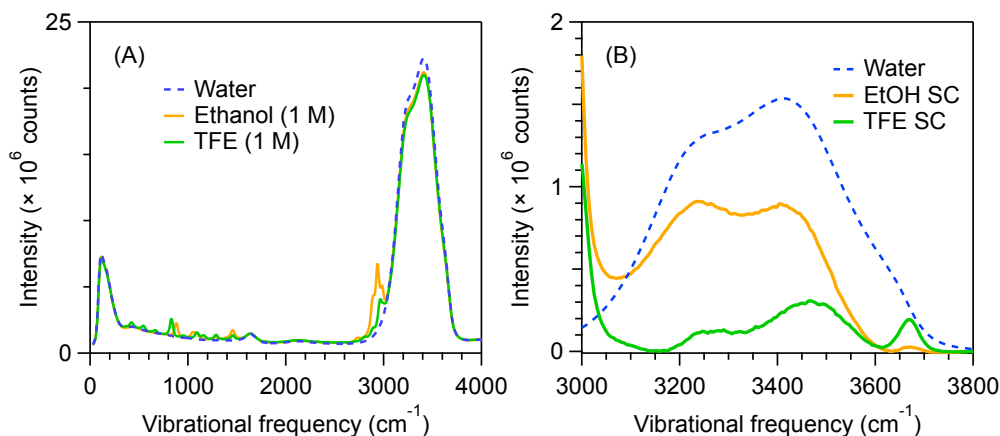


Figure B.1. Measured Raman spectra (A) and Raman-MCR SC spectra (B) obtained from water and 1 mol dm^{-3} aqueous solutions of ethanol (EtOH) and 2,2,2-trifluoroethanol (TFE). The Raman spectra in (A) are unprocessed. The solid curves spectra in (B) are solute-correlated (SC) spectra of EtOH and TFE (with their experimental intensities, pertaining to the same 1 mol dm^{-3} concentration), and the inset panel shows an expanded view of the OH stretch region, compared to that of pure water (arbitrarily scaled to the same peak intensity as the EtOH SC OH band).

B.2 Assignment of the high frequency OH peak

We have assigned the high frequency OH peak appearing in the SC spectra of TFE to water dangling OH groups. To confirm this assignment, it is important to exclude the

possibility that this dangling OH peak results from an intramolecular interaction between the OH and $-\text{CF}_3$ groups of TFE, as well as to confirm that the water dangling OH peak has a different frequency than a dangling OH arising from the TFE hydroxy group. To do so, we obtained Raman spectra of pure and mixed TFE and EtOH solutions at 20 °C. Figure B.2(A) shows the spectra of pure TFE and EtOH, and Figure B.2(B) shows the SC spectra obtained from 1 mol dm⁻³ and 2 mol dm⁻³ solutions of TFE in EtOH. The inset panel

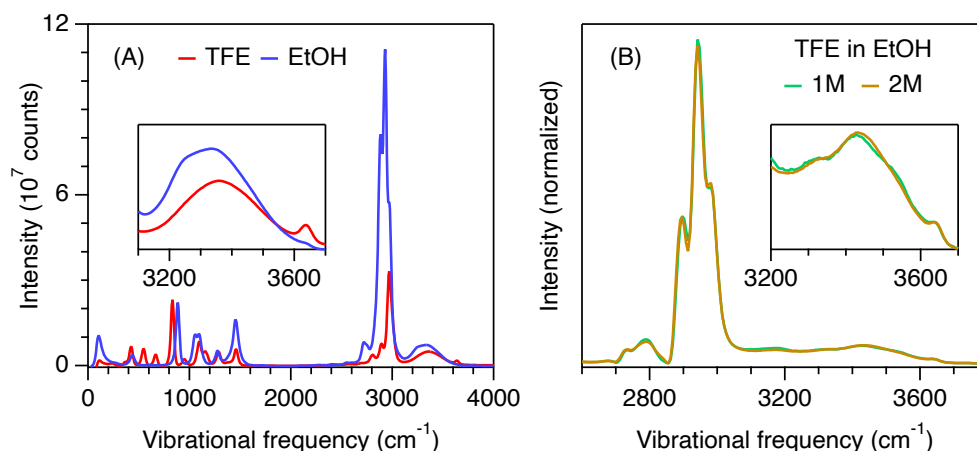


Figure B.2. (A) Raman spectra of TFE and EtOH. (B) Raman-MCR SC spectra of TFE in EtOH, obtained from solutions with TFE concentrations of 1 mol dm⁻³ and 2 mol dm⁻³. The inset panels show expanded views of the corresponding OH bands. The SC spectra in (B) are normalized to the same CH band intensity.

in Figure B.2(A) reveals the relatively sharp dangling OH peak of pure TFE at a frequency of ~ 3639 cm⁻¹.^{195,196} The inset panel in Figure B.2(B) shows the smaller dangling OH peak with a frequency of ~ 3642 cm⁻¹. (These peak positions were obtained after subtracting the underlying hydrogen bonded OH background). The different frequencies of the dangling OH peaks imply that the dangling OH peak in panel (B) is due to EtOH molecules in the solvation shell of TFE. This assignment is also consistent with the smaller intensity of the dangling OH band in panel (B) than that in panel (A). Specifically, if the dangling OH bands in Figure B.2(A) and (B) were all due to an intramolecular interaction between the TFE

OH group and its own CF_3 group then one would expect the dangling OH intensity to scale linearly with TFE concentration. The intensity of the dangling OH peak for 1 mol dm^{-3} TFE in EtOH is about 45 times smaller than that of pure TFE, while the corresponding TFE concentration is only 13 times smaller. Finally, the dangling OH peak observed in the SC spectra of TFE in water has a frequency $\sim 27 \text{ cm}^{-1}$ higher than the dangling OH peak in pure TFE, which further supports our assignment of that dangling OH peak obtained from aqueous TFE solutions to a water dangling OH rather than an intramolecular TFE dangling OH.

B.3 Dangling OH bands after subtracting a Gaussian background

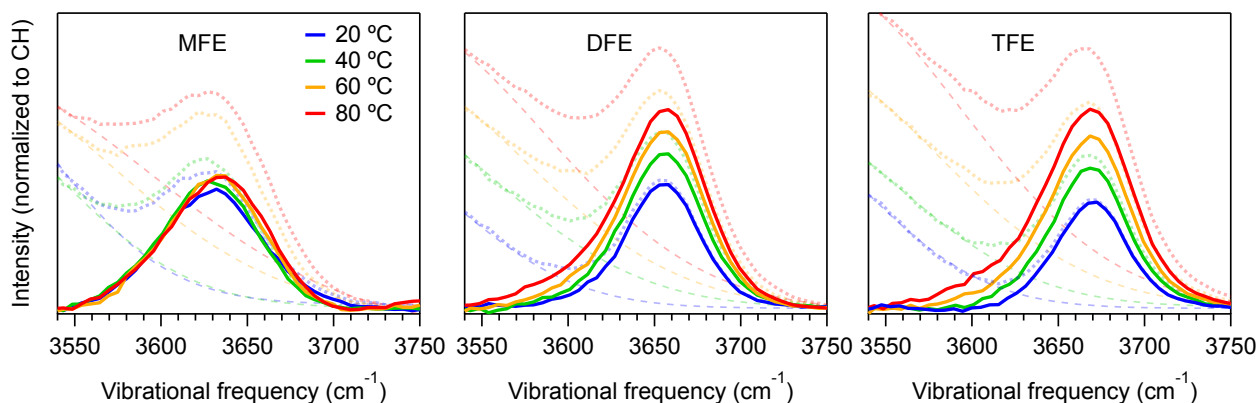


Figure B.3. Temperature dependence of the dangling OH peaks in the hydration shell of MFE, DFE and TFE. These peaks were obtained from the respective minimum area non-negative SC spectra (transparent solid lines), after subtracting the background (dashed lines) using a Gaussian fit. Analogous to Figure 3.4 in Chapter 3.

B.4 Hydration thermodynamics

Table B.1 compiles Henry’s law coefficients of EtOH, MFE, DFE, and TFE obtained from different literature sources.

Table B.1. Henry’s law coefficients of EtOH, MFE, DFE, and TFE.

Solute	K_H	Units	T (K)	Reference DOI
EtOH	20 ± 3	kPa	293.2	10.1021/je900711h
EtOH	184 ± 35	M atm ⁻¹	298.2	10.5194/acp-15-4399-2015
MFE	120 ± 20	kPa	293.2	10.1021/je900711h
DFE	60 ± 20	kPa	293.2	10.1021/je900711h
TFE	59 ± 6	M atm ⁻¹	298.2	10.5194/acp-15-4399-2015

The coefficients in Table B.1 were used to estimate the experimental hydration free energy of MFE, DFE, and TFE relative to that of EtOH as indicated in Table B.2. The experimental hydration free energy varies as $\text{MFE} < \text{DFE} < \text{EtOH} < \text{TFE}$.

Table B.2. Experimental hydration free energy of EtOH, MFE, DFE, and TFE.

Solute	K_H ratio (f)	$-RT \ln(f)$ (kJ mol ⁻¹)	ΔG_{hyd} (kJ mol ⁻¹)
EtOH	—	—	-21.0 ± 0.8
MFE	6.0	-4.4	-25.3 ± 0.9
DFE	3.0	-2.7	-23.6 ± 0.9
TFE	0.3	2.8	-18.2 ± 0.9

C. ADDITIONAL METHODS AND EXPERIMENTAL RESULTS FOR RAMAN-MCR OF MICELLE FORMATION

This appendix provides additional Raman-MCR results obtained for the micellization of 1,2-hexanediol in aqueous solutions with and without salt addition, as described in Chapter 4. The derivations of the micellization and Wyman-Tanford expressions are also presented.

C.1 Additional experimental results

Figure C.1 compares the free monomer (solid curves) and micelle (dotted curves) SC spectra of 12HD in pure water (blue), aqueous 0.25 M Na_2SO_4 (green), and aqueous 2 M NaSCN (red). Note that both the free monomer and micelle hydration shell spectra of 12HD in aqueous Na_2SO_4 are quite similar to those in pure water. This indicates that there is little direct interaction between either Na^+ or SO_4^{2-} and 12HD, although the small influence of this salt on the micelle hydration-shell spectrum may indicate a slight penetration of SO_4^{2-} ions into the hydration shell of the micelle. In aqueous NaSCN, on the other hand, both the free monomer and micelle spectra are significantly different than those in pure water, thus indicating a significant interaction between SCN^- ions and the hydration shells of both the free monomers and micelles. The decrease in the OH band area of the free monomer in aqueous NaSCN is consistent with the penetration of SCN^- into the first hydration shell of 12HD, thus expelling some water molecules out to the surrounding solvent. The increase in area of the micelle hydration shell spectrum in aqueous NaSCN implies that interactions between the SCN^- ions and the micelle alters the micelle hydration-shell water structure, relative to that of the hydration shell of a micelle in pure water.

It is also noteworthy that in all the solutions the hydration shell band of the free monomer has a more prominent shoulder near 3200 cm^{-1} , relative to that in pure water. An increase in the 3200 cm^{-1} shoulder implies an increase tetrahedral ordering in the hydration shell of the free monomer, as is the case in the hydration shell of other alcohols,^{3,8} as well as methane⁸⁹ dissolved in water. On the other hand, the hydration shell OH band of the micelle has a less prominent 3200 cm^{-1} shoulder and is shifted to higher frequency (relative to the monomer

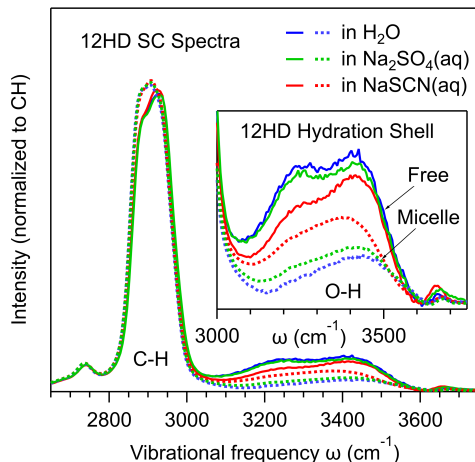


Figure C.1. Raman-MCR SC spectra of free (solid curves) and aggregated (dotted curves) 12HD in pure water (blue), aqueous 0.25 M Na_2SO_4 (green), and aqueous 2 M NaSCN (red).

hydration shell), thus indicating that the micelle hydration shell is less ordered (and more weakly hydrogen-bonded) than the hydration shell of the free monomer, as is also the case in other concentrated (crowded) aqueous alcohol solutions.¹⁰⁶ Moreover, the smaller area of the micelle hydration shell band is consistent with the aggregation-induced expulsion of water molecules from the oily tails of some of the 12HD molecules, as also observed in other micelle Raman-MCR spectra.⁸⁷

Further evidence of the interaction between SCN^- and 12HD is provided by the spectra shown in Figure C.2, which compares the $\text{C}\equiv\text{N}$ stretch band features that appear in aqueous NaSCN (dashed black curve) with those in the 12HD SC spectra (solid curves). Comparison of the dashed black and high concentration solid purple curve clearly reveals that the interaction between SCN^- and the micelles produces a significant red-shift in the $\text{C}\equiv\text{N}$ stretch band of SCN^- . At the lowest 12HD concentrations, the $\text{C}\equiv\text{N}$ stretch band appears to split into two sub-bands. A clue regarding the assignment of these sub-bands is provided by additional measurements, performed in aqueous solutions with a lower NaSCN concentration of 0.5 M, in which the free monomer SC spectrum has a single $\text{C}\equiv\text{N}$ band that is blue-shifted relative to the $\text{C}\equiv\text{N}$ of aqueous NaSCN, as shown in Figure C.3.

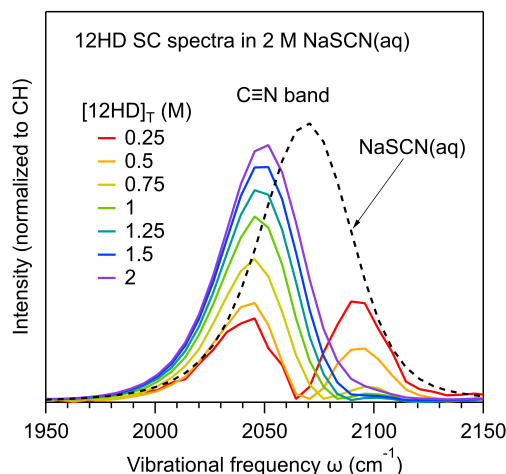


Figure C.2. The SC $\text{C}\equiv\text{N}$ stretch band of aqueous 2 M NaSCN (dashed black curve) is compared with the $\text{C}\equiv\text{N}$ bands appearing in the concentration dependent SC spectra of 12HD.

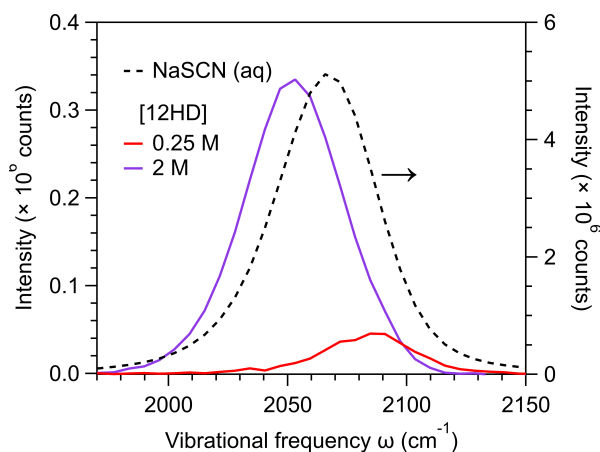


Figure C.3. The $\text{C}\equiv\text{N}$ band in aqueous NaSCN (dashed-black band) is compared with that in the SC spectrum of 12HD dissolved in 0.5 M NaSCN. Note that interaction of SCN^- with 12HD monomers at low concentration shifts the $\text{C}\equiv\text{N}$ band to higher frequency, while the interaction of SCN^- with 12HD micelles at high concentration shifts the $\text{C}\equiv\text{N}$ band to lower frequency.

The two bands in the red (and orange) spectrum in Figure C.2 are apparently due to SCN^- ions interacting both with free 12HD monomers and with some small aggregates of 12HD. Note that the red bands pertain to a 12HD concentration of 0.25 M, which is well

below C_A and so there should be virtually no micelles in this solution, but there may be some lower order aggregates of 12HD. Thus, the appearance of a low frequency C \equiv N sub-band in Figure C.2 at 12HD concentrations down to 0.25 M indicates that low order aggregates of 12HD are stabilized in 2 M NaSCN. It is also important to note that the appearance of two bands in a SC spectrum can also arise when a single hydration shell band is broader than the corresponding solvent band,¹⁹¹ and so the two red (and orange) bands in Figure C.2 could also arise from a single broad hydration shell C \equiv N band, resulting from a distribution of 12HD monomers and small aggregates.

The fact that the strongly kosmotropic anion SO_4^{2-} is expelled from the hydration shell of 12HD is evidenced not only by the similarity of the free monomer hydration shell spectra in pure water and aqueous Na_2SO_4 (Figure C.1) but also by the fact that the S=O stretch band of SO_4^{2-} is not perturbed by 12HD, and does not appear in the SC spectra of 12HD (Figure C.4). This absence of an S=O band in the SC spectrum of 12HD at all concentrations implies that sulfate ions are expelled from both the monomer and micelle hydration shells.

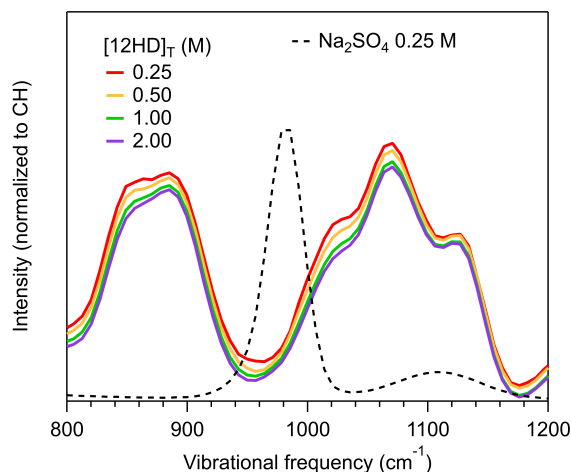


Figure C.4. The S=O band in aqueous Na_2SO_4 (dashed-black band) is compared with that in the SC spectrum of 12HD dissolved in 0.25 M Na_2SO_4 . Note that the solid curves reveal bands due to 12HD (normalized to the same CH band area), and show no evidence of a perturbed S=O band, thus confirming that there is no indication of any interaction between SO_4^{2-} and either the free monomers or micelles of 12HD.

C.2 Derivation of micellization and Wyman-Tanford expressions

The formation of micelles in an aqueous solution is driven by the equilibrium between free surfactant monomers (M) and micelle aggregates (M_n) of size n , dictated by the following difference between the corresponding chemical potentials.⁹⁹

$$\Delta\mu_n^\circ = \mu_n^\circ - \mu_1^\circ \quad (\text{C.1})$$

Note that μ_i° is the chemical potential of a monomer in an aggregate of size i at a standard state concentration of $C_i = 1 \text{ M}$, and C_i is the total concentration of monomers that reside in an aggregate of size i . If the concentrations remain sufficiently low that interactions between free monomers and micelles may be neglected, the concentrations may be equated with the corresponding activities. Under these conditions, the micelle formation equilibrium constant, $K_n = [M_n]/[M]^n = (C_n/n)/C_1^n = e^{-\beta n \Delta\mu_n^\circ}$, will be approximately independent of the total surfactant concentration (and if the chemical potentials are expressed in molar units, then $\beta = 1/RT$, where T is the absolute temperature and R is the gas constant). Thus, Equation C.2 may be used to relate the aggregated and free monomer concentrations.⁹⁹

$$C_n = n \left(C_1 e^{-\beta \Delta\mu_n^\circ} \right)^n \quad (\text{C.2})$$

Equation C.2 further implies that the critical aggregation concentration (C_A) is approximately related to $\Delta\mu_n^\circ$ as follows

$$C_A \approx e^{+\beta \Delta\mu_n^\circ} \quad \text{or equivalently,} \quad \Delta\mu_n^\circ \approx RT \ln C_A. \quad (\text{C.3})$$

Note that the latter expression is equivalent to the usual relation between the standard chemical potential of a micelle and the corresponding critical micelle concentration (C_A),^{96,100,197} although here all concentrations are expressed in molar (rather than mole fraction) units. The above expressions pertain to any reasonable definition of C_A , including that at which $C_1 = C_n$ or $C_1 = \frac{1}{n}C_n$, as long as $n \gg 1$ (as is typically the case for micelles).

If the critical micelle concentration is defined as $C_1 = C_n = C_A$, then it follows that $C_A = \left(\frac{1}{nK_n}\right)^{\frac{1}{n-1}}$. Moreover, since the total monomer concentration C_T is the sum of the free and aggregated monomer concentrations, then $C_T = C_1 + C_n = C_1[1 + (C_1/C_A)^{n-1}]$. The second equality was obtained using $K_n = (C_n/n)/C_1^n$ to equate $C_n = nK_n C_1^n = C_1^n/C_A^{n-1}$. Thus, given C_A and n , one may predict C_T as a function of C_1 , and then plot C_1 and $C_n = C_T - C_1$ as functions of C_T , which is how the dotted curves in Figure 4.1D and Figure 4.2 in Chapter 4 were generated for the formation of 12HD micelles.

If the aqueous solution also contains salt of concentration C_S (pertaining to the concentration of the neutral combination of cations and anions), then the chemical potentials of the free and aggregated monomers in the salt solution may be expressed as follows.

$$\mu_{1,S}^\circ = \mu_1^\circ + k_1 C_S \quad (\text{C.4})$$

$$\mu_{n,S}^\circ = \mu_n^\circ + k_n C_S \quad (\text{C.5})$$

The coefficients k_i , which are closely related to the so-called Setschenow (or Setchenov) constants,^{96,98,198} quantify the influence of the salt on the chemical potentials of the free and aggregated surfactant molecules in the low salt concentration limit. By subtracting Equation C.4 from Equation C.5, we obtain the following difference between the micelle and monomer chemical potentials in the salt solution (where $\Delta k = k_n - k_1$).

$$\Delta\mu_{n,S}^\circ = \Delta\mu_n^\circ + \Delta\mu_{n,S}^\times = \Delta\mu_n^\circ + \Delta k C_S \quad (\text{C.6})$$

The last term in Equation C.6 may also be expressed as $\Delta k C_S = RT(\beta\Delta k C_S)$, where $\beta\Delta k C_S = \Delta k C_S/RT$ is a dimensionless quantity whose magnitude may safely be assumed to be much less than 1 (as long as the salt concentration is sufficiently low that $\Delta k C_S \ll RT$). In this limit, to first order in $\beta\Delta k C_S$, we may equate $\Delta k C_S = RT \ln(1 + \beta\Delta k C_S)$ and thus

$$\Delta\mu_{n,S}^\circ = RT \ln C_A + RT \ln(1 + \beta\Delta k C_S) = RT \ln[C_A(1 + \beta\Delta k C_S)] = RT \ln C_A^S \quad (\text{C.7})$$

where the critical aggregate concentration in the presence of the salt solution, C_A^S , is related to that in the absence of salt, C_A , as follows.

$$C_A^S = C_A(1 + \beta\Delta k C_S) \quad (\text{C.8})$$

This further implies that one may experimentally determine Δk from the measured influence of a salt on the critical aggregate concentration, where $\Delta C_A = C_A^S - C_A$,

$$\Delta k \approx RT \left(\frac{\Delta C_A}{C_A C_S} \right) \quad (\text{C.9})$$

or equivalently

$$\Delta\mu_{n,S}^\times = \Delta k C_S \approx RT \left(\frac{\Delta C_A}{C_A} \right) \quad (\text{C.10})$$

The above results may further be related to Wyman-Tanford theory, which links the aggregation equilibrium constant to the excess partitioning of salt (and water) to the free and aggregated surfactant hydration shells.

The Wyman-Tanford excess partition coefficient is defined as^{88,91–93}

$$\Gamma = \left\langle n_W \left(\frac{n_S}{n_W} - \frac{N_S - n_S}{N_W - n_W} \right) \right\rangle \quad (\text{C.11})$$

where N_i are the total number of molecules of type i in the system (where $i = S$ for salt and $i = W$ for water), and n_i are the corresponding number of molecules in the hydration shell of the surfactant. Note that Γ will be equal to zero if the local salt to water ratio in the surfactant hydration shell, n_S/n_W , is equal to that far from the surfactant, $(N_S - n_S)/(N_W - n_W)$, and Γ will be positive when salt ions accumulate around the surfactant, such that $n_S/n_W > (N_S - n_S)/(N_W - n_W)$, and conversely Γ will be negative if salt ions are expelled from the surfactant hydration shell. Note that in the extreme expulsion limit $n_S = 0$ and thus $(N_S - n_S)/(N_W - n_W) = N_S/(N_W - n_W) > N_S/N_W$, as expulsion of salt from the surfactant hydration shell will increase the salt concentration in the surrounding solvent. It is also important to note that the above expression implies that when Γ is not equal to zero, its

magnitude is expected to increase with increasing salt concentration, because both n_S/n_W and $(N_S - n_S)/(N_W - n_W)$ increase with increasing salt concentration.

Wyman-Tanford theory, combined with Equation C.10, yields the following relationship between the salt concentration derivative of $\ln K_n$ and the corresponding excess partition coefficients:

$$\frac{d \ln K_n}{d \ln C_S} = C_S \left(\frac{d \ln K_n}{d C_S} \right) = \frac{-n C_S}{RT} \left(\frac{d \Delta \mu_{n,S}^{\circ}}{d C_S} \right) = \frac{-n \Delta k C_S}{RT} = \Gamma_A - \Gamma_F \quad (\text{C.12})$$

Note that Γ_A pertains to partitioning of salt to the hydration shell of the entire aggregate (micelle) containing n monomers, and Γ_F pertains to partitioning of the salt to the hydration shells of a collection of n free monomers, and thus the magnitudes of both Γ_A and Γ_F are expected to increase with increasing micelle size. Equations C.10 and C.12 imply that the measured salt-induced change in the critical micelle concentration may be used to experimentally determine $\Delta \Gamma = \Gamma_A - \Gamma_F$ as follows

$$\Delta \Gamma = -n \left(\frac{\Delta C_A}{C_A} \right) = -n \left(\frac{C_S \Delta k}{RT} \right) = -n \beta \Delta \mu_{n,S}^{\times} \quad (\text{C.13})$$

Thus, a salt-induced decrease in C_A implies that $\Gamma_A > \Gamma_F$, independent of the signs of Γ_A and/or Γ_F . In other words, a decrease in C_A may occur either when salt has a net affinity for both the free and aggregated surfactant or a net expulsion from both, as long as the salt ions have a greater affinity for the micelle than the free surfactant monomers.

C.3 Wyman-Tanford partition coefficient bounds

The salt-induced changes in 12HD critical micelle concentration, C_A , have been used to directly determine that $\Delta \Gamma \approx 4.6$ in 0.25 M Na_2SO_4 and $\Delta \Gamma \approx 4.0$ in 2 M NaSCN , as described in Chapter 4. Reasonable ranges of values for Γ_F and Γ_A in the two salt solutions may be established by considering the following limiting scenarios: i) assuming that the salts do not change the micelle chemical potential ii) assuming that the salt concentration is the same in the hydration shells of the free surfactant monomers and micelles.

The first of the above two scenarios amounts to assuming that $\Gamma_A = 0$, in which we obtain $\Gamma_F \approx -4.6$ in 0.25 M Na_2SO_4 and $\Gamma_F \approx -4.0$ in 2 M NaSCN . The second scenario implies that $\frac{n_s}{n_w} - \frac{N_s - n_s}{N_w - n_w}$ is the same for the free and aggregated 12HD solutions, and thus $\frac{\Gamma_A}{\Gamma_F} \approx \frac{\langle n_w \rangle_A}{\langle n_w \rangle_F}$. The latter ratio (which corresponds to the ratio of the number of water molecules in the hydration shell of the aggregated and free monomers) is estimated to be $\frac{\langle n_w \rangle_A}{\langle n_w \rangle_F} \approx 0.27$, obtained from the ratio of the areas of the OH band in the hydration shell spectra of the aggregated (micelle) and free monomers, corresponding to the dotted-black and solid-red OH bands in Figure 4.1(B) of Chapter 4. Thus, this second scenario would imply that $\Gamma_F \approx \frac{4.6}{0.27-1} = -6.3$ and $\Gamma_A \approx -1.7$ in 0.25 M Na_2SO_4 , and $\Gamma_F \approx \frac{4.0}{0.27-1} = -5.5$ and $\Gamma_A \approx -1.5$ in 2 M NaSCN .

Although the above two scenarios provide a physically reasonable range of Γ values, they do not necessarily represent firm upper and lower limits on the possible values of Γ . For example, our Raman-MCR spectra indicate that SCN^- penetrates more significantly into the hydration shell of the micelle than the free 12HD monomer, as evidenced by the surfactant correlated $\text{C}\equiv\text{N}$ bands shown in Figure C.3. Specifically, the red-shifted $\text{C}\equiv\text{N}$ band arising from SCN^- in the micelle hydration shell has a larger area than the blue-shifted $\text{C}\equiv\text{N}$ band arising from the hydration shell of the free monomer (both of which have been normalized to pertain to the same 12HD concentration). This suggests $\frac{n_s}{n_w} - \frac{N_s - n_s}{N_w - n_w}$ has a larger (more positive or less negative) value in the hydration shell of the micelle than the free monomer, and thus in 2 M NaSCN our results are also consistent with $\Gamma_F > -4$ and $\Gamma_A \gtrsim 0$. On the other hand, our Raman-MCR of 12HD in 0.25 M Na_2SO_4 indicate that sulfate ions are strongly expelled from the hydration shell of a free 12HD monomer, thus implying that $n_s \approx 0$, and thus $\Gamma_F = -\left\langle \frac{n_w N_s}{N_w - n_w} \right\rangle \sim -12$ (obtained as described below), which is beyond the range of $-4.6 \geq \Gamma_F \geq -6.3$ established using the two scenarios described in the previous paragraph. Thus, in 0.25 M Na_2SO_4 the bounds on Γ_F may be extended to $-5 \geq \Gamma_F > -12$.

The lower bound of $\Gamma_F \approx -12$ for 12HD in Na_2SO_4 is obtained assuming that there are approximately $n_W \sim 63 \times 20 = 1260$ water molecules in the first hydration shells of 20 free 12HD molecules, and $N_W \sim (55/0.46) \times 20 = 2400$ when $[\text{12HD}]_T = C_A^S = 0.46$ M, and thus $N_S = N_W(0.25/55) \sim 11$ at a salt concentration of 0.25 M. The value of 63 ± 4 for the water molecules in the hydration shell of a fully hydrated 12HD was obtained by performing a molecular dynamics simulation with two 12HD molecules and 400 water molecules at 20 °C

(and 0.1 MPa), with TIP4P-2005 and OPLS-AA force fields and a first hydration-shell cut-off distance of 0.58 nm, for the water oxygen (O_w) atoms relative to any of the 12HD heavy atoms (C or O).

Note that the above Γ_i values also provide estimates of the k_i coefficients that dictate the influence of the salts on the chemical potential of the free and aggregated 12HD molecules, since $k_i = -\left(\frac{RT}{nC_s}\right) \Gamma_i$. Thus, in 2 M NaSCN the above results imply that $k_1 \leq 0.34$ (kJ/mol M⁻¹) and k_n has smaller magnitude and may have either a positive or negative sign. On the other hand, in 0.25 M Na₂SO₄, the above results imply that $2.2 \leq k_1 < 5.9$ (kJ/mol M⁻¹) while k_n has a smaller magnitude and a positive sign.

D. SUPPLEMENTARY INFORMATION FOR ION PAIRING IN ACETATE SOLUTIONS

This Appendix provides additional results to supplement discussions in Chapter 5.

D.1 Raman spectra of bound acetate

Extracting the bound acetate spectrum for a series of measured MAc_2 ($M = \text{Ca}, \text{Mg}, \text{Zn}$) solutions is non-trivial because little is known about the bound spectrum band shapes. While MCR does not require information about band profiles, a family of curves representing possible bound components can be obtained. Specifically, this involves performing a second round SMCR analysis of the first round SC spectra, including the SC spectra of NaAc and MAc_2 , performed over a frequency range of 800 cm^{-1} to 1800 cm^{-1} . This second round SMCR decomposition effectively removes the unbound contribution from the first round 0.5 M MAc_2 SC spectra. However, the resulting bound spectra may be any one of a family of possible bound spectra, as indicated by the blue regions in the spectra shown in Figure D.1. A strict boundary to this spectral family is established by a non-negativity constraint to avoid unphysical spectral components, yielding the blue spectra that differ most from the unbound acetate (dashed black spectrum). The range of possible bound spectra shown in Figure D.1 pertain to bound spectra with different spectral weights of the unbound acetate spectrum.

The MAc_2 measured spectra indicate that the CC Raman cross section is unchanged upon cation binding and thus all spectra were divided by the CC band area, so as to correspond to the same acetate concentration. The bound component that best describes ion pairing in MAc_2 solutions (dashed red curves in Figure D.1) was obtained by determining which of the possible bound spectra yielded the most self-consistent (least concentration dependent) one-to-one binding constant. The resulting variance in the binding constants across the series of possible bound spectra is shown in Figure D.2. The location of the minimum in each curve identifies the particular bound spectrum that produces the most self-consistent one-to-one binding constant. The end point of each curve represents the limiting bound

spectrum determined by the non-negativity constraint (corresponds to the blue spectra in Figure D.1 that differ most from the unbound spectrum).

D.2 Binding constant determination using TLS regression

The SC spectrum of a MAc_2 solution can be represented by a linear combination of the unbound (free) and bound acetate spectra. Thus, ion-pairing binding constants can be estimated by determining the relative contributions of these two species to the measured spectrum. Total least squares (TLS) regression can be used to obtain these relative contributions as long as the two pure component spectra are known a priori. We have shown that the NaAc SC spectrum can be taken as the spectrum of the unbound species and have obtained the bound acetate spectrum using the procedure described above. Therefore, if X is the spectrum of some mixture of Ac^- and M^{2+} , represented by a $1 \times n$ vector (where n is the number of frequency values in the spectrum), TLS can be used to decompose such spectrum into the unbound and bound components. Specifically, let P be a $2 \times n$ matrix of pure component (unbound and bound) spectra and b be a 1×2 vector that contains the spectral weights of the two components in X , such that

$$X = bP \tag{D.1}$$

The coefficients b are estimated by inverting Equation D.1 as follows

$$b = XP^T(PP^T)^{-1} \tag{D.2}$$

where P^T represents the transpose of matrix P . Note that if the spectra X and the two component spectra in P are all normalized so as to pertain to the same solute concentration, then the elements of the vector b are the percentages of the total concentration corresponding to the bound and unbound acetate species. In this work, the X spectrum was taken as the SC spectrum obtained from an aqueous MAc_2 solution, and the component spectra were the SC spectrum of the free acetate (obtained from aqueous NaAc) and the bound M^{2+}Ac^- contact-ion pair spectrum was obtained as described above. All of the spectra were normalized

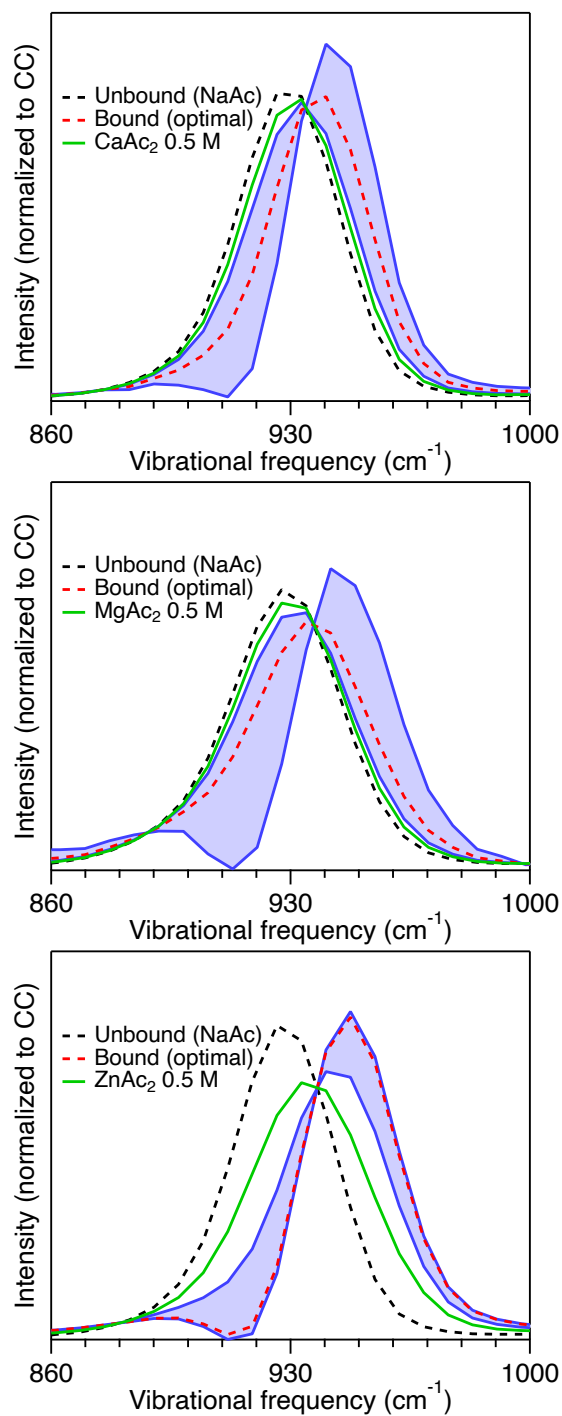


Figure D.1. Family of possible bound spectra (blue shade) in the CC region obtained for MAC₂. All spectra shown are normalized to unit area over the CC stretch band.

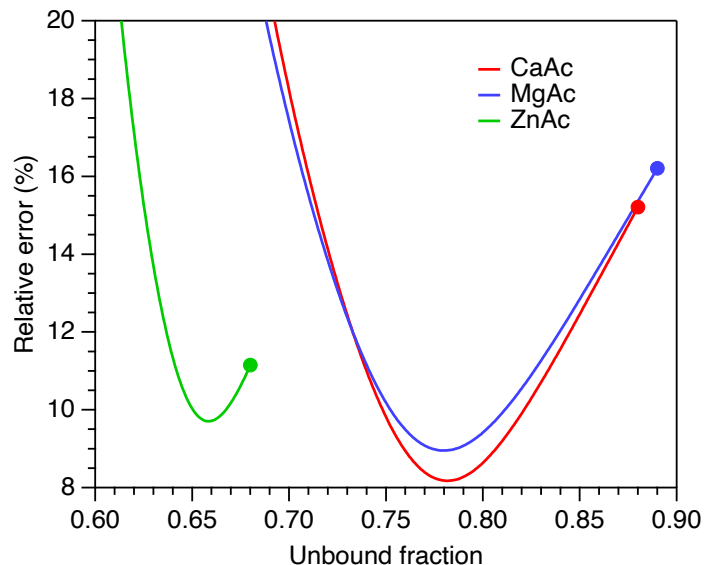


Figure D.2. Relative error with respect to the mean value of the binding constants estimated using the range of bound spectrum candidates shown in Figure D.1

to CC stretch band area to obtain concentration-independent spectra given that the CC Raman cross section is unchanged upon ion pairing.

Binding constants calculated from performing TLS on the CC band are reported in Figure 5.4 (and Table 5.1 after extrapolation to zero ionic strength) of Chapter 5. Those results do not change significantly using the COO^- or the CC and COO^- bands together when performing the TLS fits (Table D.1). Note, however, that the spectral region near the

Table D.1. Ion-pairing binding constants obtained from TLS fits to different vibrational bands. Errors correspond to the standard deviation of the values of K obtained in the 0.2 to 1 M total acetate concentration range.

Vibrational bands	MgAc ₂	CaAc ₂	ZnAc ₂
CC	1.1 ± 0.1	1.1 ± 0.1	4.5 ± 0.4
COO^-	1.2 ± 0.1	1.1 ± 0.1	4.0 ± 0.3
CC and COO^-	1.2 ± 0.2	1.1 ± 0.1	4.2 ± 0.3

OH stretch band cannot be included in the TLS regression because the free acetate spectrum was obtained with a monovalent cation (Na^+) while the other solutions contained M^{2+} ions which have a more dramatic effect on water structure.

D.3 Influence of ion pairing on acetate hydration shell spectra

The decrease in intensity of the hydration-shell OH band in Figure D.3 and Figure 5.2B in Chapter 5 as function of acetate concentration is due to the interaction of acetate with the counterions. It is likely that the small depletion of SC OH stretch band for NaAc is due to

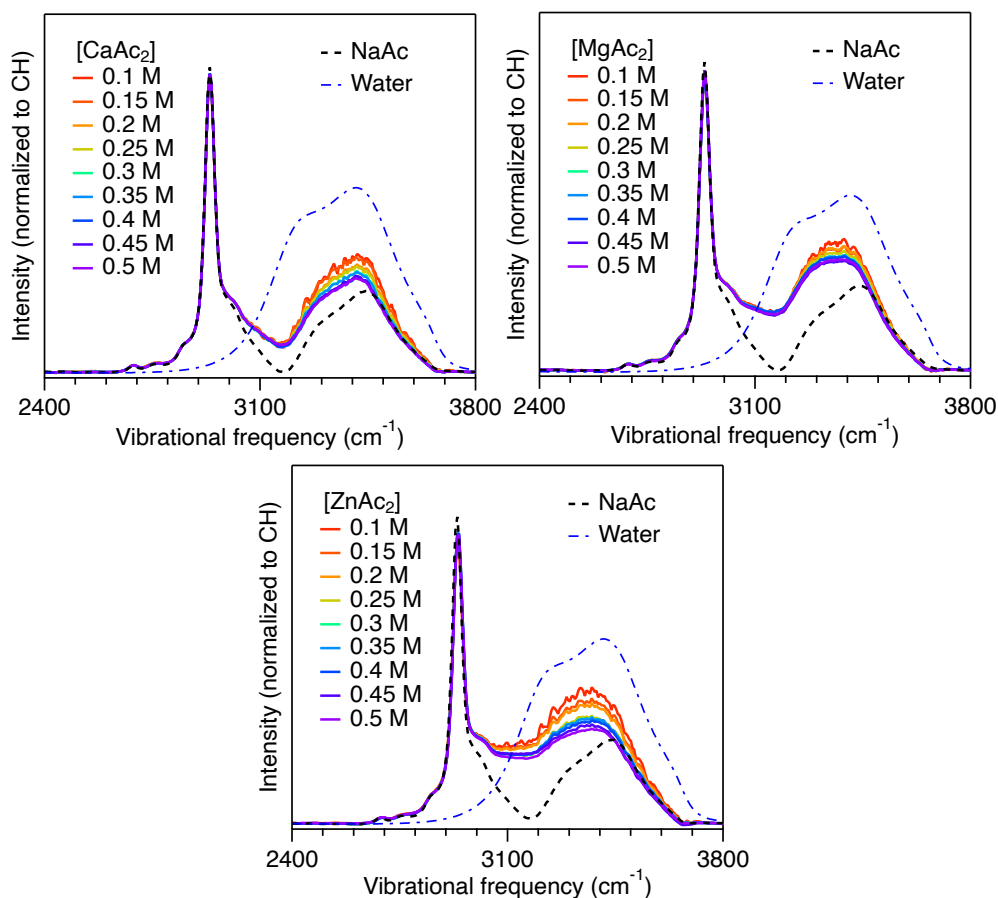


Figure D.3. Hydration-shell spectra for magnesium acetate (top), calcium acetate (middle) and zinc(II) acetate (bottom).

solvent-shared ion-pair formation since there are no significant frequency shifts of the COO^- , CC or CH, bands, thus implying that there are no direct-contact ion pairs between Na^+ and Ac^- over our experimental concentration range. However, our results are also consistent with the possibility that there are some Na^+Ac^- contact-ion pairs, but such contacts do not detectably influence the COO^- , CC or CH band shape, frequency, or intensity, as is the case for M^{2+}Ac^- contact ion pairs (with $\text{M} = \text{Ca}$, Mg , or Zn).

D.4 Simulated Raman spectra

While the Raman experiments described in Chapter 5 provide an experimental measure of the binding constant between divalent cations and acetate, they cannot determine the geometry of the observed ion pairs and have a quite limited ability to distinguish different types of ion pairs: contact monodentate, contact bidentate or solvent shared ion pairs. In order to determine which type of ion pairs can lead to a shift in the measured Raman spectra, we computed the spectra (Figure D.4) of acetate involved in different ion pair configurations with Ca^{2+} , Mg^{2+} , Zn^{2+} , and Na^+ using quantum chemical (DFT-based) calculations on a large number of snapshots extracted from molecular dynamics simulations (see Methods). Although the shape of the band near $\sim 1450\text{ cm}^{-1}$ is not perfectly reproduced, both peaks ($\sim 950\text{ cm}^{-1}$ and $\sim 1450\text{ cm}^{-1}$) exhibit a blue shift when in contact ion pair with Ca^{2+} , Mg^{2+} , and Zn^{2+} . This is more pronounced for the bidentate ion pair and for Zn^{2+} and Mg^{2+} than Ca^{2+} , which is in very good agreement with the experiment, and thus validates the procedure used to extract the signal of the bound acetate from the raw spectra. The first important finding is that the simulated spectra show that no significant shift is observed between the reference spectrum of acetate in pure water, and that of acetate ion paired with Na^+ . This validates the use of the sodium acetate solution as the “unbound” reference in the experiment. It also shows that even if there was significant pairing between acetate and sodium cations, the Raman experiment would not be able to capture it. The computed spectra for the contact ion pairs with Ca^{2+} , Mg^{2+} , and Zn^{2+} exhibit a blueshift in the CC stretch band (near 940 cm^{-1}) that is more pronounced for Zn^{2+} and Mg^{2+} than Ca^{2+} and are larger for the bidentate than the monodentate ion pairs. It is also clear that the formation

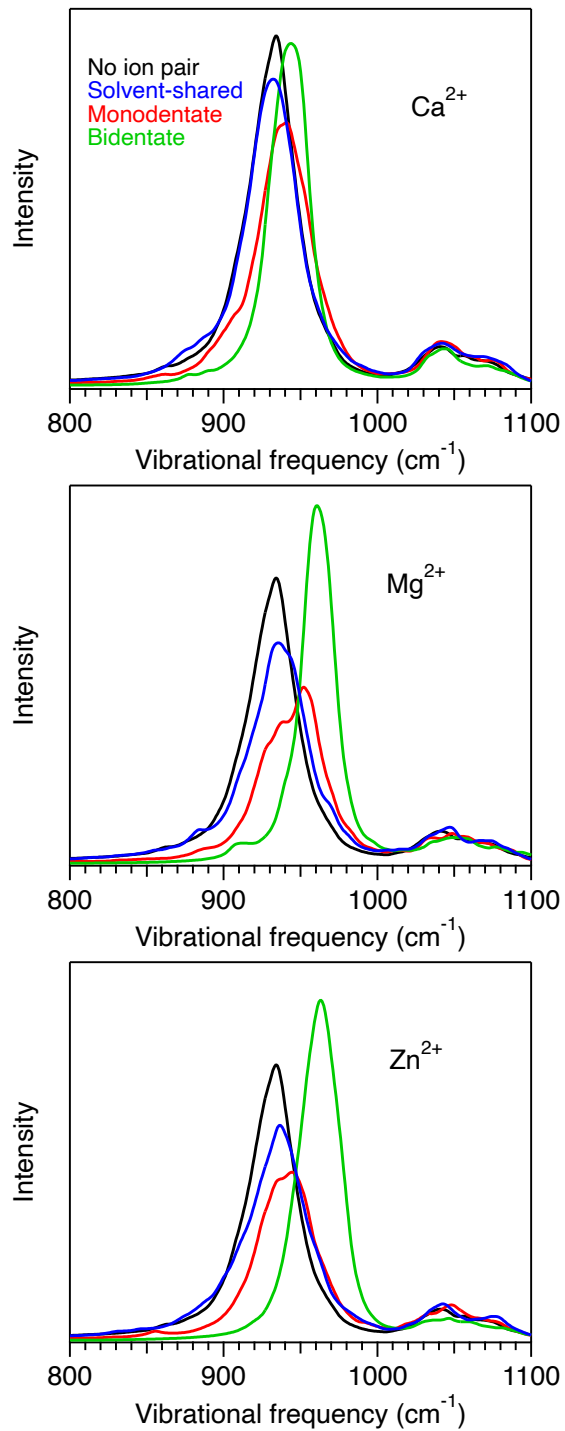


Figure D.4. Simulated Raman spectra for acetate in pure water (black) or involved in a contact monodentate (red), contact bidentate (green) or solvent-shared (blue) ion pair with a calcium, magnesium and zinc cation.

of solvent-shared ion pairs (for all cations) does not significantly affect the peak positions. Hence, the experimental binding-induced spectral changes are evidently due primarily to the formation of direct contact ion pairs. The fact that the predicted $\text{Zn}^{2+} \cdots \text{Ac}^-$ bidentate shift of $\sim 30 \text{ cm}^{-1}$ is comparable to the experimentally observed shift of $\sim 20 \text{ cm}^{-1}$ suggests that the experimental ZnAc_2 solutions may include bidentate bound species (over the experimental concentration range up to 0.5 M), probably in addition to monodentate ones. In contrast, the smaller experimental binding-induced CC band shifts of $\sim 10 \text{ cm}^{-1}$ for Mg^{2+} may imply that the binding is primarily monodentate over the experimental concentration range. For Ca^{2+} , the calculated shifts for bidentate and monodentate ion pairs are much more similar, so that no clear conclusion regarding the contact ion pair structure can be drawn.

D.5 Binding patterns from DFT-based *ab initio* molecular dynamics simulations

DFT-based *ab initio* molecular dynamics simulations were performed using formate instead of acetate due to the large computational cost to obtain the free energy profile along the distance between the carboxylate carbon atom and the cation, in the region corresponding to the bidentate (short distances) to monodentate (larger distances) transformation, as shown in Figure D.5. Due to the limited sampling allowed by these very expensive simulations, the error bar on the free energy profile is quite large, and difficult to estimate precisely, on the order of 4–5 kJ mol^{-1} . However, they are robust to details of the simulation setup and bring very informative insight. Indeed, the AIMD simulations confirm that Mg^{2+} –acetate ion pairs are only stable in a monodentate geometry (C–Mg distance of 3.1 Å), the bidentate ion pair being more than 25 kJ mol^{-1} higher in free energy. In contrast, both geometries appear possible (within the error bars) with Ca^{2+} . For Zn^{2+} , the AIMD simulations are in line with previous suggestions in the literature that the monodentate and bidentate binding modes are of similar stability.

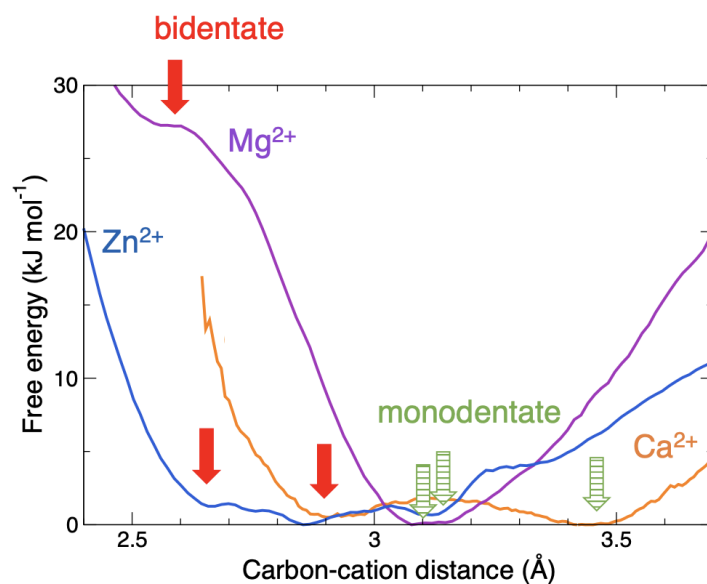


Figure D.5. Free energy profiles along the carboxylate carbon-cation distance for calcium (orange), magnesium (purple) and zinc (blue) as obtained from DFT-based ab initio MD simulations. The location of the bidentate and monodentate ion pairs is indicated with red and dashed green arrows, respectively.

E. ADDITIONAL RESULTS FOR WATER-SHARED ION PAIRING IN HYDROXIDE SOLUTIONS

This appendix describes additional analysis methods and contains supplementary experimental results for Chapter 6 .

E.1 Temperature-dependent thermodynamic analysis

The values of K_0 and b were obtained from the experimentally measured intensities of the normalized SC spectra at the vibrational frequencies specified below. The spectra are those shown in Fig. 6.2(A and C) of Chapter 6 and Fig. E.2 of the next subsection. The intensities were measured in frequency windows of $\sim 5 \text{ cm}^{-1}$ width centered at 3396, 3402, 3407, 3413, and 3418 cm^{-1} for the NaOH SC spectra, and 3460, 3465, 3471, 3496, and 3481 cm^{-1} for the LiOH SC spectra, in the vicinity of the local minima in the high temperature spectra shown in Fig. 6.2(B and D) of Chapter 6. The intensities I (counts) at each of the above frequencies were fit to a quadratic function of the total salt concentration, $I = a_0 + a_1 c_T + a_2 c_T^2$, from which the values of K_0 and b were determined using $K_0 = -a_1/a_0$ and $b = a_2/a_1 - 2a_1/a_0$. These expressions were derived from a Taylor expansion of Eq. 6.2 in Chapter 6, performed by first Taylor expanding the numerator and then factoring out $K_0 c_T$ before re-expanding the entire remaining expression to third order in c_T .

The dotted curves in Fig. E.1 and Fig. 6.3(A and B) in Chapter 6 were obtained using Eqs. 6.2 and 6.3 with the best fit K_0 and b values given in Table E.1. Note that all these predictions agree well with the data points, except for LiOH at 20 °C. This discrepancy may be linked to the fact that the dissociated ion pair fractions of LiOH at 20°C extended down to $x_F \sim 0.06$, while all the other results in Fig. E.1 pertain to dissociated fractions $x_F > 0.2$. The dashed blue curve in Fig. E.1(B) shows how the agreement with the predictions is improved if $K_0 \sim 0.85$ is held fixed and $b \sim 2$ is obtained from a best fit to the blue x_F points.

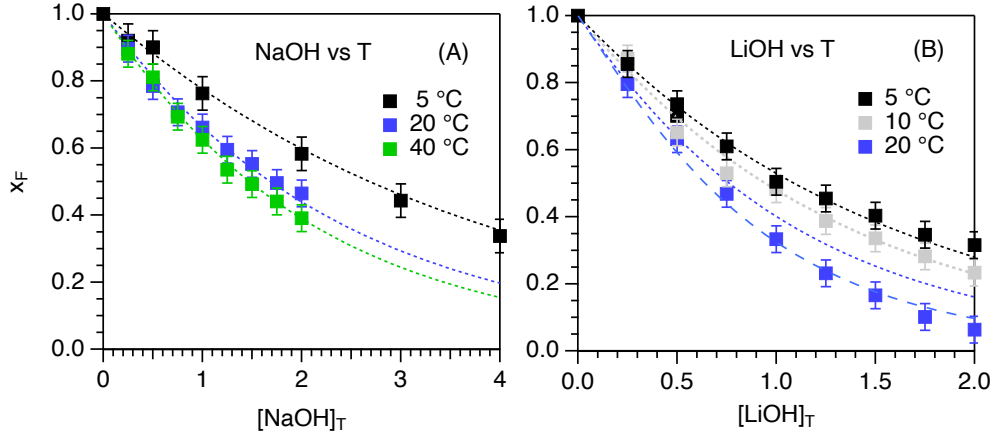


Figure E.1. Dissociated ion pair fractions, $x_F = I/I_0$, were fit to obtain K_0 and b , as described above. The 5 °C points are the same as those in Fig. 6.3(A and B) of Chapter 6, and the points at other temperatures were obtained from the SC spectra shown in Fig. E.2. The dotted curves are obtained using Eq. 6.2 and 6.3 with the K_0 and b values in Table E.1.

Table E.1. K_0 and b values obtained from the dissociation fraction x_F points in Fig. E.1.

	NaOH			LiOH		
T (°C)	5	20	40	5	10	20
K_0	0.25 ± 0.01	0.41 ± 0.03	0.45 ± 0.02	0.61 ± 0.02	0.70 ± 0.04	0.85 ± 0.03
b	0.41 ± 0.01	0.64 ± 0.04	0.74 ± 0.03	1.00 ± 0.04	1.17 ± 0.08	1.47 ± 0.06

E.2 Additional Raman-MCR results

Figure E.2 shows concentration-dependent Raman-MCR SC spectra of aqueous NaOH at 20 °C and 40 °C and aqueous LiOH at 10 °C and 20 °C . The corresponding results at 5 °C are shown in Fig. 6.2(A and C) of Chapter 6.

All SC spectra in Figure E.2 and Figure 6.2 were obtained after performing a background subtraction using a fourth-order polynomial fit to baseline points adjacent to the OH stretch band, as exemplified in Figure E.3. This procedure is necessary to remove any spurious background intensity present in the solution spectrum compared to the pure water spectrum and to generate a SC spectrum with the smallest non-negative area above the background.

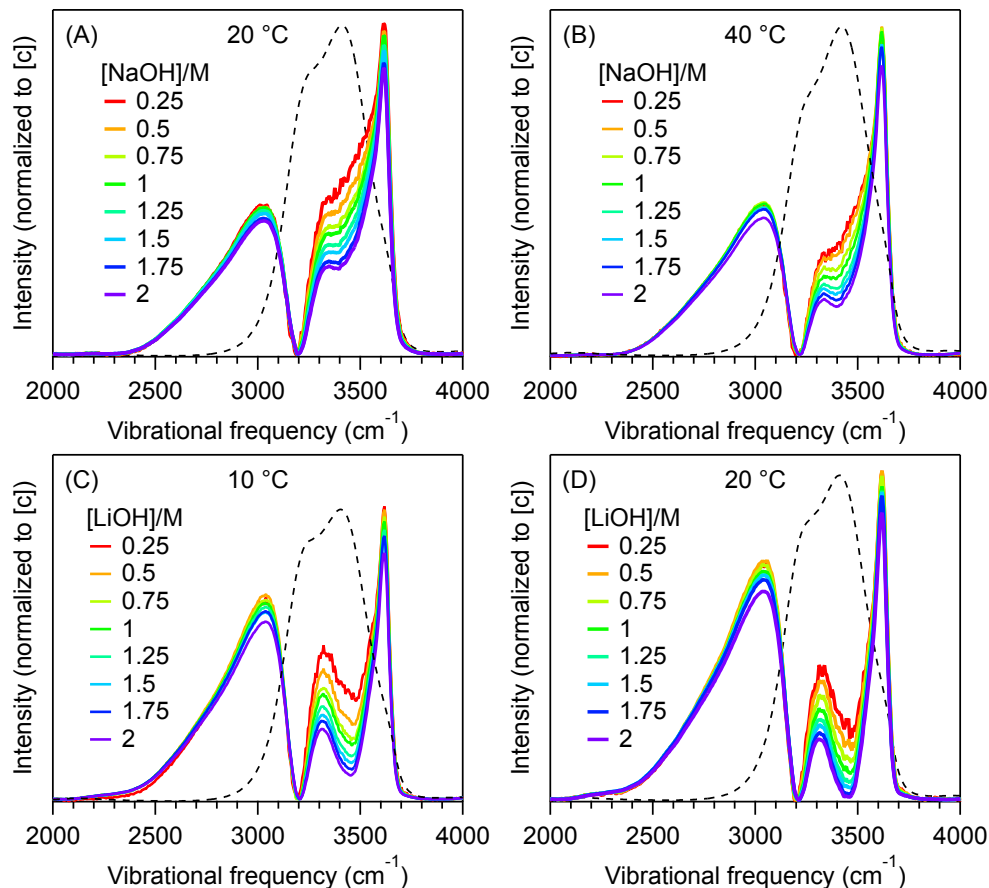


Figure E.2. Concentration-dependent Raman-MCR hydration-shell spectra of aqueous NaOH (A: 10 °C and B: 40 °C) and LiOH (C: 10 °C and D: 20 °C). The dashed curves are pure water spectra at the specified temperatures (scaled to approximately the same peak intensity).

E.3 Supporting AIMD results

Figure E.4 shows AIMD results for the distribution of cations and water molecules with respect to the hydroxide ion. Specifically, the radial distribution functions, $g(r)$, and the respective numbers, $N(r)$, of cations (upper two panels) and water oxygen atoms (lower two panels) are plotted with respect to their distance from the hydroxide oxygen atom.

Figure E.5 shows two dimensional plots of the distribution of water molecules around each hydroxide ion, plotted in the same way as the cation distribution functions shown in Fig. 6.1(C and D) of the parent manuscript. The fact that these distributions are nearly

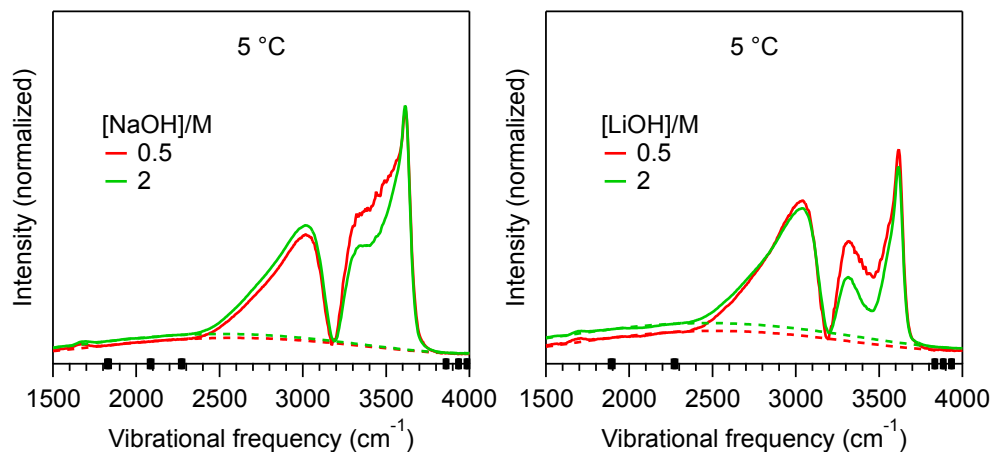


Figure E.3. Raman-MCR SC spectra of aqueous (0.5 M and 2 M) NaOH and LiOH at 5 °C prior to background subtraction. The dashed curves represent the fourth-order polynomial function fit to the background points marked with black squares on the x -axis.

identical confirms that the hydroxide hydration shell remains nearly fully intact even in the more significantly ion paired LiOH solution. Close inspection of the $g(r)$ results in Fig.E.4(C) reveals that there are slightly fewer second hydration shell waters around OH^- in the LiOH solution, as evidenced by the slightly smaller second $g(r)$ peak in LiOH than NaOH.

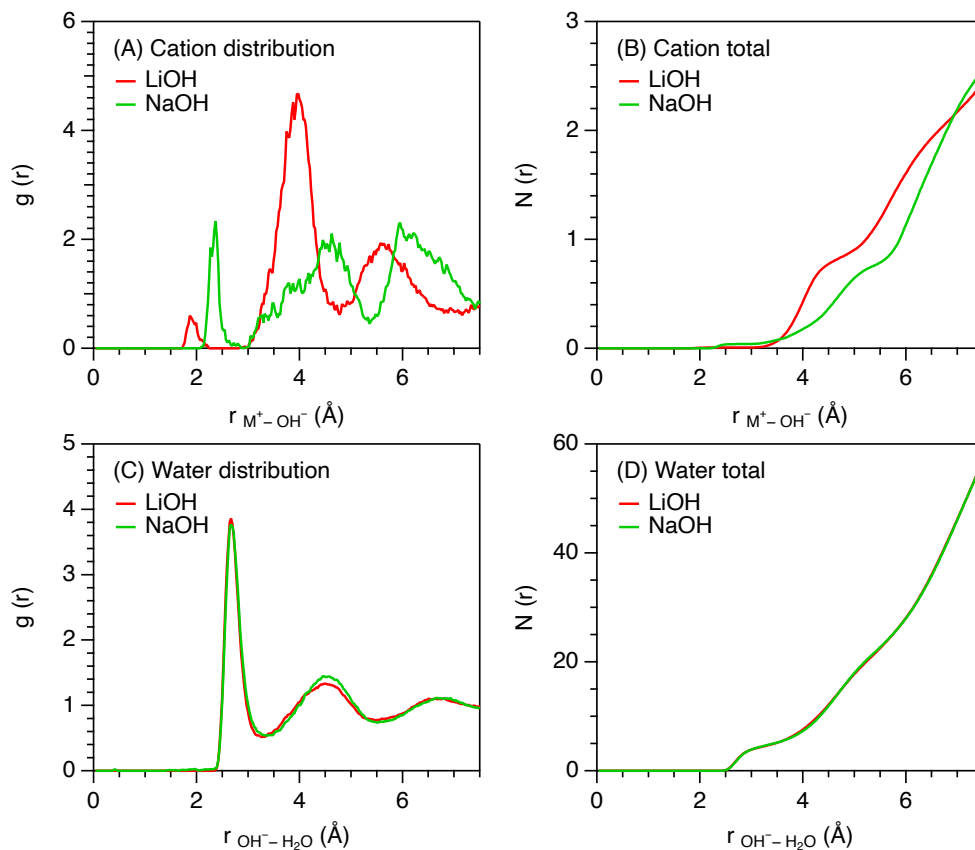


Figure E.4. AIMD predictions of the populations of cations (A and B) or water molecules (C and D) surrounding the hydroxide ion in 1 M LiOH (red) and 1 M NaOH (green) at 25 °C. The radial distribution functions $g(r)$ (A and C) and integrated number of cations or water molecules $N(r)$ (B and D) are plotted as a function of the distance between the OH^- oxygen atom and either the cation, M^+ , or the oxygen atom of H_2O

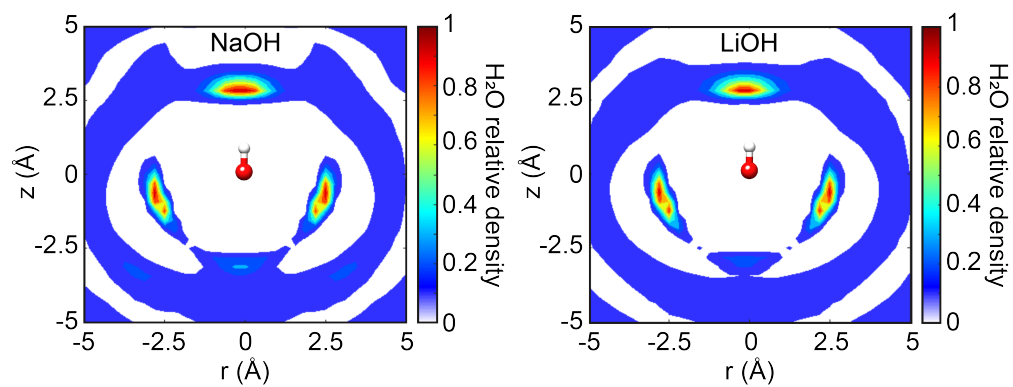


Figure E.5. AIMD predictions of the distributions of H₂O around OH⁻ in 1 M solutions of NaOH (right panel) and LiOH (left panel) at 25 °C. The r and z axes are distances relative to the hydroxide oxygen atom located at $(r, z) = (0, 0)$.

LIST OF PUBLICATIONS

- (1) **Mendes de Oliveira**, D.; Bredt, A. J.; Miller, T. C.; Corcelli, S. A.; Ben-Amotz, D. [Spectroscopic and structural characterization of water-shared ion pairs in aqueous sodium and lithium hydroxide](#). *J. Phys. Chem. B* **2021**, *125*, 1439–1446.
- (2) **Mendes de Oliveira**, D.; Ben-Amotz, D. [Spectroscopically quantifying the influence of salts on nonionic surfactant chemical potentials and micelle formation](#). *J. Phys. Chem. Lett.* **2021**, *12*, 355–360.
- (3) Maruthamuthu, M. K.; Raffiee, A. H.; **Mendes de Oliveira**, D.; Ardekani, A. M.; Verma, M. S. [Raman spectra-based deep learning: A tool to identify microbial contamination](#). *MicrobiologyOpen* **2020**, *9*, e1122.
- (4) Urbina, A. S.; Boulos, V. M.; Zeller, M.; **Mendes de Oliveira**, D.; Ben-Amotz, D. [Binding-induced unfolding of 1-bromopropane in \$\alpha\$ -cyclodextrin](#). *J. Phys. Chem. B* **2020**, *124*, 11015–11021.
- (5) Robalo[†], J. R.; **Mendes de Oliveira**[†], D.; Imhof, P.; Ben-Amotz, D.; Vila Verde, A. [Quantifying how step-wise fluorination tunes local solute hydrophobicity, hydration shell thermodynamics, and the quantum mechanical contributions of solute–water interactions](#). *Phys. Chem. Chem. Phys.* **2020**, *22*, 22997–23008. [†]**These authors contributed equally.**
- (6) **Mendes de Oliveira**, D.; Zukowski, S. R.; Palivec, V.; Hénin, J.; Seara, H. M.; Ben-Amotz, D.; Jungwirth, P.; Duboué-Dijon, E. [Binding of divalent cations to acetate: Molecular simulations guided by Raman spectroscopy](#). *Phys. Chem. Chem. Phys.* **2020**, *22*, 24014–24027.
- (7) Robalo, J. R.; Streacker, L. M.; **Mendes de Oliveira**, D.; Imhof, P.; Ben-Amotz, D.; Verde, A. V. [Hydrophobic but water-friendly: Favorable water–perfluoromethyl interactions promote hydration shell defects](#). *J. Am. Chem. Soc.* **2019**, *141*, 15856–15868.
- (8) Robalo, J. R.; **Mendes de Oliveira**, D.; Zaric, M.; Ben-Amotz, D.; Imhof, P.; Verde, A. V. [Rethinking hydrophobicity: Dangling OH groups as molecular fingerprints](#). *Eur. Biophys. J.* **2019**, *48*, S199–S199.
- (9) **Mendes de Oliveira**, D.; Fontes, L. M.; Pasquini, C. [Comparing laser induced breakdown spectroscopy near infrared spectroscopy and their integration for simultaneous multi-elemental determination of micro- and macronutrients in vegetable samples](#). *Anal. Chim. Acta* **2019**, *1062*, 28–36.

- (10) **Mendes de Oliveira, D.**; Ben-Amotz, D. [Cavity hydration and competitive binding in methylated \$\beta\$ -cyclodextrin](#). *J. Phys. Chem. Lett.* **2019**, *10*, 2802–2805.
- (11) Suarez, W. T.; Alvarenga Jr, B. R.; Franco, M. K.; Gabriel, W. L.; **Mendes de Oliveira, D.**; Santos, V. B. [In situ determination of urea in milk employing a portable and low-cost LED photometer](#). *Food Anal. Methods* **2018**, *11*, 1149–1154.
- (12) **Mendes de Oliveira, D.**; Catão, V. [Teoria das metas de realização em sala de aula e as possíveis influências nos padrões motivacionais para a aprendizagem da química em duas turmas do ensino médio](#). *Góndola, Ens. Apr. Cien.* **2017**, *12*, 50–68.
- (13) **Mendes de Oliveira, D.**; Suarez, W. T.; Alvarenga Jr, B. R.; Gabriel, W. L.; Santos, V. B. [Nitroprusside as a novel reagent for flow injection spectrophotometric determination of captopril](#). *Anal. Lett.* **2016**, *49*, 200–207.
- (14) Alvarenga Jr, B. R.; Gabriel, W. L.; **Mendes de Oliveira, D.**; Reis, C.; Teofilo, R. F.; Santos, V. B.; Suarez, W. T. [Determination of fluoride in mouthwash using flow-injection analysis with spectrophotometric detection](#). *Curr. Pharm. Anal.* **2014**, *10*, 208–214.